Synthesis of Heteroleptic Redox-active and Spin-crossover Complexes

Mark Pelaccia, BSc.

A thesis submitted in partial fulfilment of the requirements for the degree of Master of Science in Chemistry

Faculty of Mathematics and Science
Brock University
St. Catharines, Ontario

Abstract

The following research regarding heteroleptic redox-active complexes with the potential for spin-crossover is synthetic in nature. The intent behind incorporating the Schiff base ligand *N*-(8-quinolyl)salicylaldimine with some redox-active species into a mixed ligand complex featuring a d^4-d^7 metal ion center was to prime the material for spin-crossover based on strong intermolecular interactions that would enhance cooperativity of the system. Single component systems that display spin-crossover behaviour paired with other physical properties like electrical conductivity hold significance in the field of multifunctional materials, of which there are few examples that feature mixed ligand systems. Information describing this type of chemistry and the magnetic interactions that govern these characteristics is introduced in the first chapter of this work.

The synthetic strategies toward mixed ligand complexes in the form of $[(Qsal)Fe(RAL)]^+X^-$ and $[(Qsal)Co(RAL)]^+X^-$ have been realized from the use of mononuclear $[(Qsal)FeCl_2(CH_3OH)]$ and $[(Qsal)Co(OAc)]^+OAc^-$ species, respectively. The redox-active ligand (RAL) component is an arylazo ligand like 10-(8-quinolylazo)-9-phenanthrol (Qapl) or 1-(2-Pyridylazo)-2-phenanthrol (Papl), which possess a low-lying π^* MO that makes them susceptible to multi-step reductions that give rise to radical intermediates. Heteroleptic complexes that were synthesized and isolated like $[(Qsal)Fe(Qapl)]^+BPh_4^-$, $[(Cl\text{-}Qsal)Fe(Qapl)]^+BPh_4^{--}$ and homoleptic $[Fe(Qapl)_2]^+BPh_4^-$ were diffracted and measured several intermolecular π-π contacts of distances typically between 3.5-3.7 Å, often between the phenanthrene rings of adjacent Qapl ligands. Complexes In the form of $[(Qsal)Fe(Qapl)]^+X$ (X= BPh_4^- or SCN^-) showed early onset of spin transition in solution usually beyond 298 K. These complexes were overly reduced in the glovebox which resulted in their deterioration, presumably

from the cleavage of the RAL azo bond. The framework developed for the heteroleptic Fe^{3+} coordination chemistry was applied to cobalt, with some amendments, and afforded several heterleoptic Co^{3+} complexes using Qsal with the arylazo ligands Qapl and Papl. The heteroleptic cobalt complexes presented here were found to be LS Co^{3+} which is diamagnetic. However, there is potential under inert atmosphere to produce Co^{2+} and possibly a phenoxyl radical species with redox-active valence tautomers.

ACKNOWLEDGEMENTS

Throughout the research work and writing of this thesis I have received an abundance of guidance and assistance. I would first like to thank my supervisor, Dr. Martin Lemaire of Brock University whose expertise, guidance, and patience were invaluable in the formulating of this research project.

I would like to thank my committee members, Dr. Georgii Nikonov and Dr. Travis Dudding of Brock University for their instruction and encouragement along the process of conducting the research work.

I would like to thank Ms. Liqun Qiu of Brock University for her expertise and analysis in mass spectrometry, Mr. Razvan Simionescu of Brock University for his assistance with nuclear magnetic resonance and Evans method experiments, and Dr. Art van der Est of Brock University for his assistance with electron paramagnetic resonance experiments. I would also like to thank Dr. Brian Patrick of University of British Columbia, Dr. Alan Lough of University of Toronto, and Dr. Melanie Pilkington of Brock University for their services in X-ray crystallography.

I would like to acknowledge my colleagues Nico Bonanno, PhD candidate, and Zackery Watts, MSc candidate, of Brock University for their assistance in the laboratory, as well as Brock University for their facility and provisions to conduct this research.

Finally, I would like to thank my mother, father, grandmother and sister for all of their support.

Table of Contents

List of Figures

List of Tables

List of Schemes

Abbreviations and Symbols

a.u.	ambiguous units
BM	Bohr Magnetons
CFSE	Crystal field stabilization energy
cm^{-1}	wavenumbers
CV	Cyclic voltammetry
d	doublet
DCM	Dichloromethane
dd	doublet of doublets
dH_2O	distilled water
DMF	Dimethylformamide
ESI	Electron spray ionization
EtOH	Ethanol
FT-IR	Fourier transform infrared spectroscopy
HR-MS	High resolution mass spectrometry
HS	High spin
irr	irreversible
K	Kelvin
LR-MS	Low resolution mass spectrometry
LS	Low spin
m	multiplet
md	medium
MeCN	Acetonitrile
MeOH	Methanol
m/z	mass to charge ratio
nm	nanometers
P	Pairing energy
qr	quasi-reversible
RAL	Redox-active Ligand
RBF	round bottom flask
s	singlet
SCO	Spin-crossover
SQUID	Superconducting Quantum Interference Device
st	strong
t	triplet
TBA	Tetrabutylammonium
TEA	Triethylamine
THF	Tetrahydrofuran
UV-vis	Ultraviolet visible spectroscopy
VT	Variable temperature
w	weak

Chapter 1.0 Introduction to Coordination Chemistry

The interaction between Lewis acids and Lewis bases to form complexes is the basis of coordination chemistry. In metal-coordination complexes, the metal ion acts as a Lewis acid because it accepts a lone pair of electrons from a Lewis base, which is referred to as the ligand. Based on this interaction, the metal ion is acknowledged as the acceptor atom while the atoms that bear the lone pair of electrons on the ligand are designated as the donor atoms.[1] The following chapter will begin by delving into the roots of coordination chemistry and discussing the early issues that were addressed in order to gain greater insight and appreciation for this field of chemistry. The outcome of several initial studies which were conducted to resolve the discrepancies between the shapes, structures, and electron configurations of early coordination complexes laid the foundation for the understanding of concepts in modern coordination chemistry.

1.1.0 History of Coordination Chemistry

The fundamental theories regarding coordination chemistry were first addressed in the late 1800s. At the time there was controversy revolving around the chemical structures and ambiguity between the coordination numbers and oxidation state of the metal ions in coordination complexes. Two important figures, Sophus Mads Jørgensen and Alfred Werner established the basis for modern coordination chemistry. Early work began with the use of metal-ammines.[1,12] Originally, Jørgensen through his work with cobalt-ammines of the form $[CoCl_3(NH_3)_6]$ proposed that the complexes were formed with the ammonia groups binding together in a chain-like manner based on the fact that many organic molecules at the time were described as chain structures.[12] Later in 1893, Alfred Werner correctly determined the structures

of *d*-block metal coordination complexes through his research regarding ligand displacement with $CoCl_3$ and NH_3. Most of Jørgensen's work provided much of the foundation for Werner's theories. Werner was able to generate a series of $CoCl_3$ compounds with NH_3 noted by colour changes and the addition of $AgNO_3$ to precipitate different quantities of AgCl per equivalent of Co^{3+} in solution.[12] The significance behind precipitating free Cl^- ions as AgCl suggested that any Cl^- not precipitated was associated with the coordination compound which led Werner to conclude that the Co^{3+} metal in these compounds must have been concomitant with six ligands; a mixture of Cl^- and NH_3 bound to the metal.[12] As a result from conductivity measurements of the number of ions in solution, Werner was able to formulate the complexes $[Co(NH_3)_6]Cl_3$, $[Co(NH_3)_5Cl]Cl_2$ and $[Co(NH_3)_4Cl_2]Cl$ and referred to the metal ion's oxidation state and coordination number as its primary and secondary valences respectively.[12] Werner was able to isolate two isomers of the complex $[Co(NH_3)_4Cl_2]^+Cl^-$ where he concluded that the 6-coordinate $[Co(NH_3)_4Cl_2]^+$ complex had an octahedral geometry able to exist as a *cis*- or *trans*- isomer.[12] Alfred Werner was awarded the Nobel Prize in chemistry in 1913 for his discoveries and contributions toward coordination chemistry. He passed away shortly after in 1919.[12]

1.2.0 Magnetic Properties of Coordination Complexes

The magnetic properties of a material fundamentally are governed by the magnetic moments of the electrons. Electrons possess two components associated with magnetic moment: spin angular momentum (*S*) and orbital angular momentum (*L*).[2,3] Spin angular momentum is a quantum number that represents the electron movement about its axis. The orbital angular momentum is the quantum number that represents the precession of the electron around the nucleus.[4] The vector coupling of the *S* and *L* parameters gives a total angular momentum value *J*,

$$J = S + L$$

The quantum number *S* can be an integer or half integer value while the quantum number *L* is an integer value. [2,3] The coupling of the electron spin about its own axis to the spin around the nucleus is defined as the spin-orbit coupling and gives rise to a measurement known as the g-factor. This spin-orbit coupling creates a magnetic field. [3,4] However, when *L* has no value then there is no orbital angular momentum and the system can be described as a spin only system. For a single electron the g-factor is typically close to 2.0 representing a spin-only value.[3,38] The magnetism of spin-only ions are defined by a spin microstate (m_s) that can hold a value of either $+\frac{1}{2}$ or $-\frac{1}{2}$.

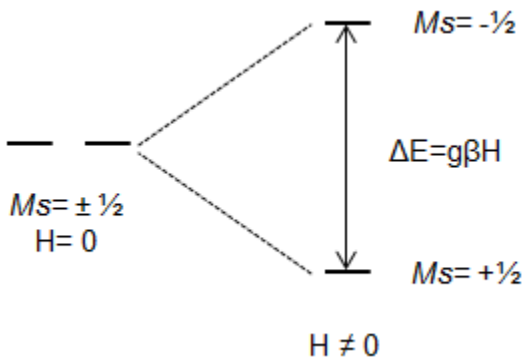

Figure 1.0: Splitting of M_s states in an external magnetic field.

The spins of the unpaired electrons for a single metal ion can communicate and therefore contribute to a net spin, *S*:

$$S = \Sigma m_s$$

The sum of the individual spins in the *d*-orbitals is a function of oxidation state and geometry whereas the total spin quantum number for a transition metal ion is given by $= \frac{n}{2}$, where *n* denotes the number of unpaired electrons.[3,4] The spin multiplicity can be defined as $2S + 1$. Therefore, the magnetic moment (μ) for spin-only behaviour is defined as,

$$\mu_{SO} = 2\sqrt{S(S+1)}$$

If there is a possibility for contribution from orbital angular momentum, then the formula that applies to free ions is amended to,

$\mu = \sqrt{L(L+1) + 4S(S+1)}$ where the $L(L+1)$ expression accommodates for the orbital angular momentum

A material's magnetic susceptibility (χ) is described as a ratio of its magnetization (M) to an external magnetic field of a given intensity (H),

$$\chi = \frac{M}{H}$$

Applying a magnetic field causes a loss of degeneracy for the energies of the M_s states which is known as the Zeeman effect.[2,3] The Zeeman effect causes the splitting of S into a series of M_s states that range from integers of $-S$ to $+S$.[2,4] The response to the applied magnetic field gives rise to an alignment within the material that indicates whether it is diamagnetic, having its electrons paired, or paramagnetic, having unpaired electrons.[2,4] Diamagnetic materials are repelled from the external magnetic field and are associated with negative magnetic susceptibility values ($\chi<0$).[3,4] This translates to the material's intrinsic magnetic field being weakened by the applied magnetic field. Paramagnetic materials are attracted into the external magnetic field as a result of aligning with the field and are associated with positive magnetic susceptibility values ($\chi>0$).[3,4] As a result of aligning with the field, a paramagnetic species' magnetic momenta will be enhanced by the applied magnetization. The population of these M_s states is dependent upon the applied field and the temperature.[4] At low temperatures a larger magnetization is observed.[4,5] This is because the population of the excited states is reduced which causes a larger population of the M_s ground state. If the external field is held constant

while the temperature is lowered then the measure of χ increases and can be described by Curie's Law,

$\chi = \frac{C}{T}$ where C is the Curie constant $\frac{1}{8}g^2S(S+1)$ emu·K·mol^{-1} and T is temperature in Kelvin

A species will generally follow Curie behaviour when they have a well isolated M_s ground state.[2,3] However, not all species follow Curie behaviour. Several other factors including spin-orbit coupling, zero-field splitting, or magnetic exchange coupling can cause a species to deviate from Curie behaviour.[2,3] In these circumstances, a more accurate method to model the magnetic behaviour is through the Curie-Weiss expression,

$$\chi = \frac{C}{(T-\theta)}$$ where θ represents the Weiss constant

The magnetism from the transition metal ion in a coordination complex is regulated by a number of factors including the oxidation state of the metal ion, the coordination geometry, the magnitude of the crystal field splitting (Δ_o) and, the magnitude of the inter-electron repulsion (P).[1,3]

1.2.1 Deviations from Spin-only Behaviour

Deviations from spin-only behaviour originate through second-order spin-orbit coupling effects.[3] These effects cause deviations in the spin-only g-factor value of 2.0.[3,4] Often in conjunction with second-order spin-orbit coupling are the effects of zero-field splitting. Zero-field splitting is the splitting or loss of degeneracy of the M_s states in the absence of an external magnetic field, in essence a zero field.[2,4] The effects of zero-field splitting contribute to changes in relative energies and populations of the M_s states and as a result lead to deviations from Curie behaviour. Causes for zero-field splitting are anisotropic in nature and can come from: magnetic

anisotropy due to second-order spin-orbit coupling, structural anisotropy at the metal center of coordination complexes that undergo *Jahn-Teller* distortion or from other structural anisotropy as a result of differences in the chemical environment not pertaining to the coordination sphere.[3,4] Often observed in octahedral geometries, the *Jahn-Teller* effect highlights the loss of symmetry and energy with respect to orbitals as a result of the coordination complex's geometric distortion which is dependent upon its electronic state.[3,5]

In literature, two common measures of susceptibility that are reported are mass magnetic susceptibility (χ_m) in units of m^3/kg or molar magnetic susceptibility (χ_{mol}) measured as cm^3/mol. Two important properties that define the molar susceptibility are density and the material's molar mass, as related in the formula below:

$$\chi_{\text{mol}} = \frac{M\chi_{volume}}{\text{density}, \rho}$$

The magnitude of the response that the paramagnetic molecule has to an applied field is known as the effective magnetic moment (μ_{eff}).[2] The effective magnetic moment (μ_{eff}) can be determined experimentally from measuring the molar magnetic susceptibility (χ_m) expressed in Bohr magnetons (μ_B) which is related to the molecular mass of the compound.[2,3] A classical technique to measure magnetic susceptibility with respect to volume of a solid sample involves the use of a Gouy balance. The Gouy balance measures the ostensible change in the mass of a sample as it is attracted to or repelled by an applied magnetic gradient.[1] Two different measurements are conducted for the Gouy balance method: a weight reading of the sample in the absence of the magnetic field (m_a) and the weight of the sample in the magnetic field (m_b). This change in mass in the presence of the applied magnet is proportional to the mass magnetic susceptibility of the material.[1,2]

$$\chi_g = \frac{\mathrm{CL}(m_b - \mathrm{m}_a)}{10^9 \mathrm{M}}$$

A positive difference in mass (m_b-m_a>0) is a result of the sample being drawn into the magnetic field and indicates that the material is paramagnetic. This means that that magnetic susceptibility of a paramagnetic material is positive because the overall magnetic induction is greater than the applied magnetic field.[1,2] In contrast, diamagnetic materials exhibit insignificant or negative changes in weight and therefore, negative values of magnetic susceptibility since they are repelled by the applied magnetic field and have a weaker magnetic induction effect. [1,2] In solution the magnetic susceptibility of a sample can be measured through the use of Nuclear magnetic resonance (NMR) frequency by a technique known as Evans method. Evan's method can also be used to measure the temperature dependent switching of a spin-crossover complex in solution.[3,21] The technique determines the $\chi_M T$ of a paramagnetic species from the frequency shift ($\Delta\delta$) of diamagnetic solvent molecules which interact with the paramagnetic species in relation to the reference solvent.[21]

$$\chi_M = \frac{477\ \Delta\delta}{2x10^6\ M}$$

Where χ_M is molar susceptibility in cm^3/mol, $\Delta\delta$ is the frequency shift in ppm, and M is the concentration in mol/cm^3

Measurements recorded by Evan's method have significance toward developing materials capable of switching for potential solution-based chemosensing applications like MRI contrasting agents.[21]

Another method for analyzing paramagnetic species is by Electron Paramagnetic Resonance (EPR). EPR uses a varied magnetic field for probing the species with unpaired electrons while holding an external microwave frequency constant.[2,38] In contrast, NMR

involves holding the magnetic field constant while probing for the difference in energy between the $m_s = -\frac{1}{2}$ and $m_s = +\frac{1}{2}$ states using radio waves, which leads to signal broadening and inconsistent chemical shift values for paramagnetic species.[1,2] In EPR, the coupling of the electron spin about its own axis to the spin around the nucleus is the spin-orbit coupling process that gives rise to the aforementioned g-value.[2] This spin-orbit coupling creates a magnetic field which is analogous to the chemical shift values observed in NMR.[1,4,43] The spectra below in Figure 1.1 depict Fe^{3+} in the low spin and high spin configuration in the complex $[Fe(Qsal)_2]^+X^-$.

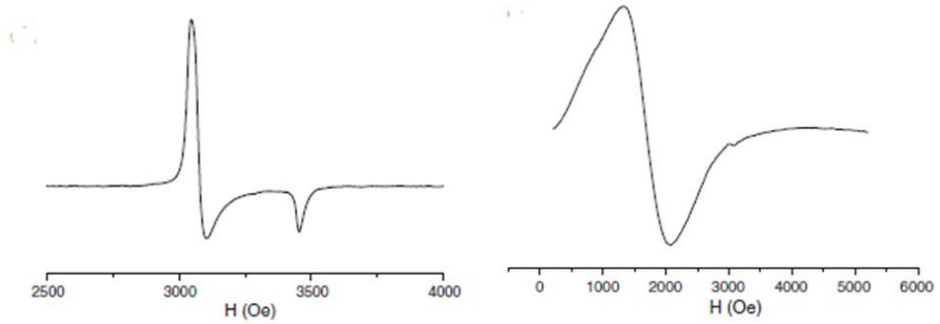

Figure 1.1: EPR spectrum of LS Fe^{3+} in $[Fe(Qsal)_2]^+CF_3SO_3^-$ at 130 K (left); EPR spectrum of HS Fe^{3+} in $[Fe(Qsal)_2]^+Cl^-$ at 250 K (right). Taken from *Appl. Magn. Reson.*, **2011**, 40, 1-10.

Complexes $[Fe(Qsal)_2]^+Cl^-$ and $[Fe(Qsal)_2]^+CF_3SO_3^-$ were investigated by EPR to study the dependence of the Fe^{3+} spin state on the type of counter ion and temperature. The Fe^{3+} center in the $[Fe(Qsal)_2]^+CF_3SO_3^-$ complex is observed at 130 K with g_x= 2.182, g_y= 2.175, and g_z= 1.929 values commonly seen for a LS state Fe^{3+} (S=1/2) species.[38] The $[Fe(Qsal)_2]^+Cl^-$ complex is a HS state Fe^{3+} (S=5/2) between 5-300 K, characterized by the strong rhombic distortion and the correspondence to Curie-Weiss behaviour based on the temperature dependence of the integrated intensity of the EPR signal.[38]

Hyperfine coupling patterns can also be observed by EPR which originate from the magnetic coupling of an electron spin to any magnetic nuclei present.[3,43] This coupling is

observed in the first derivative of the absorption spectra that splits the paramagnetic signal into *2nI+1* lines of equal intensity, where *n* represents the number of nuclei that the electron couples to and *I* indicates the spin state of the nuclei.[1,43] A LS Fe^{3+} ion has only one unpaired electron (S=1/2) in its low energy subset of bonding orbitals and therefore displays a characteristic signal in the first derivative of its absorbance reading. [1,38] However, deviations from spin-only behaviour that cause deviations from approximate g-value of 2.0 originate from second-order spin-orbit coupling effects and zero-field splitting as previously introduced in subsection 1.2.1.

1.2.2 Magnetic Interactions and Ligand Effects

Magnetic interactions between metal centers that communicate directly or through some ligand typically give rise to ferromagnetic or antiferromagnetic coupling.

Figure 1.2: Neighbouring electron alignments in (a) ferromagnetic species and (b) antiferromagnetic species.

Ferromagnetically coupled materials have their magnetic dipoles aligned in the same direction whereas antiferromagnetically coupled materials have magnetic dipoles that align in opposite directions as designated by the electron spin quantum number (m_s).[1,4] These types of interactions can be influenced by the electronic interactions between the metal ion and the ligands. The coordination of a ligand to a metal center is greatly influenced by the ligand's denticity and the types of donor atoms the ligand features.[1,5] Denticity refers to the number of donor atoms a ligand has available for coordination.[1,5] Most coordination systems incorporate ligands that are multidentate and possess several donor atoms, either anionic or neutral with a lone pair that can coordinate simultaneously. Multidentate ligands are able to engage in a process called chelation

which describes the ligand's ability to chelate or wrap itself around the metal using several donor atoms.[1] The formation and stability of coordinate bonds between the ligand's donor atoms and the metal ion can be characterized using Hard-Soft-Acid-Base (HSAB) theory.[1] HSAB theory takes into consideration factors such as size, polarizability and oxidation states. Donor atoms that are considered to be soft bases are generally larger in size and relatively polarizable.[1] These include donors like phosphorus, sulfur and chloride. Donor atoms that are classified as hard bases are typically smaller and are non-polarizing. These commonly include nitrogen, oxygen and fluoride.[1] Smaller sized metal ions with high oxidation states are considered as hard acids while larger sized metals with lower oxidation states are softer.[1] Generally, hard bases have a greater binding affinity toward hard acids while soft bases associate better with soft acids. The ligand interactions along or in between the *xyz* plane causes the metal's *d*-orbitals to segregate into different energy levels which results in a loss of degeneracy.[1,4,44]

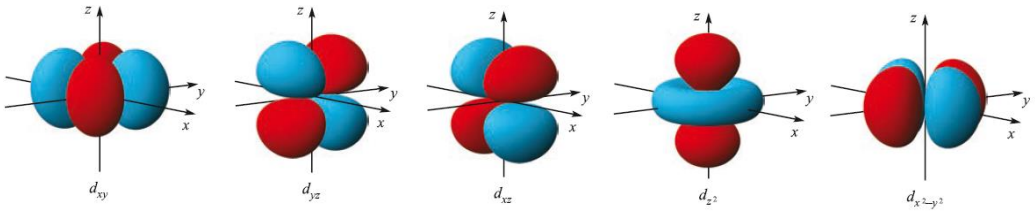

Figure 1.3: Degenerate *d*-atomic orbital diagrams generated in *Orbital Viewer* by David Manthey. Taken from *Inorganic Chemistry* 4th Ed., 2012, Harlow, England: Pearson Education Ltd.

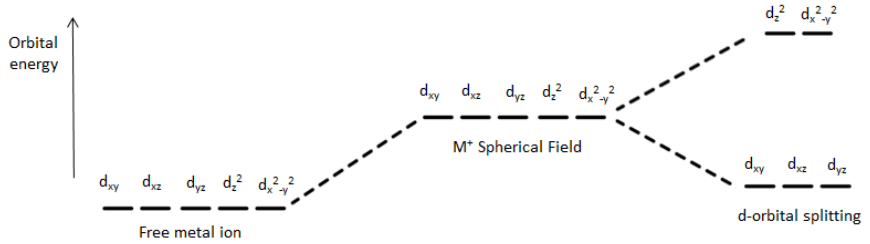

Figure 1.4: Changes in *d*-orbital energies of a first row M^{n+} ion as a result of an octahedral crystal field.

The d_{xy}, d_{xz}, and d_{yz} orbitals rest in between the spaces of the xyz axes while $d_{x^2-y^2}$ and d_{z^2} rest along the axes. Crystal field theory is used to explain the loss of degeneracy of the metal's *d*-orbitals as a result of electron repulsion by the ligand.[1,5] A spherical electrostatic or crystal field results in destabilization of the energies of the five *d*-orbitals uniformly as depicted by the rise in energy of the free metal ion in Figure 1.4. The low-lying energy orbitals are d_{xy}, d_{xz}, d_{yz} and the higher energy level orbitals are $d_{x^2-y^2}$ and d_{z^2}. The electron configuration among these orbitals determines the spin-state of the metal.[1] Low-spin states are a result of the electrons fully occupying the low level d_{xy}, d_{xz}, d_{yz} orbitals. High-spin states occur when one or more electrons are able to occupy the high level $d_{x^2-y^2}$ and d_{z^2} orbitals.[1] However, the shortcoming presented with the crystal field model is that it emphasizes more ionic bond character rather than covalent between the metal and ligand, in essence oversimplifying the ligand to metal interactions.[1] A more comprehensive understanding of the orbital rearrangements and bonding interactions in coordination complexes comes from an extension of crystal field theory known as ligand field theory. Ligand field theory accounts for the overlap of the ligand and metal atomic orbitals and, does not treat each ligand as a point charge. The model is essentially an application of molecular orbital theory with respect to the *d*-orbitals of the metal ions.[1] Under different symmetries there are different splitting patterns of energy levels. Complexes with a coordination number of four are typically found in a square planar or tetrahedral geometry. Higher coordination numbers like a six-coordinate complex is most commonly found in an octahedral geometry. In an octahedral symmetry there are three triply degenerate low energy orbitals labeled as t_{2g} and two doubly degenerate high energy orbitals labeled as e_g as shown below in Figure 1.5.[1,5]

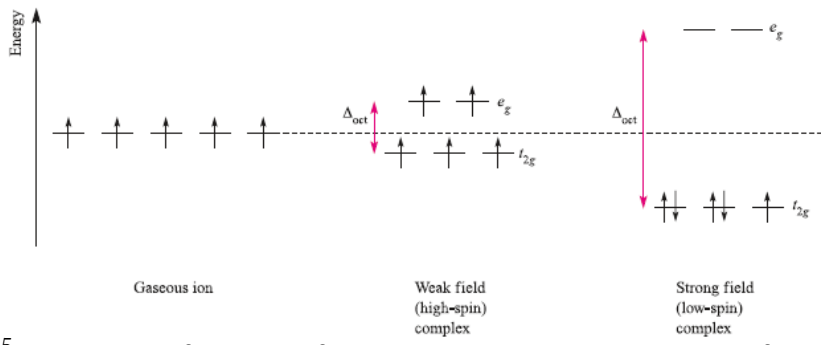

Figure 1.5: d^5-electron configuration for HS state (center) and LS state (far right) under O_h symmetry.

The t_2g and e_g sets of orbitals correspond to the low energy d_{xy}, d_{xz}, d_{yz} and high energy $d_x^2{}_{-y}^2$ and d_z^2 orbitals respectively. The strength of the metal-ligand interactions are governed by symmetry, energy match of molecular orbital formation, and orbital overlap.[1,5] In the case of a 3*d* transition metal like iron, these interactions are dominated by the ligand's interaction with the valence 4*s* and 4*p* orbitals. Both sigma (σ) and pi (π) bonding interactions are taken into consideration between the ligands and the metal with respect to the loss of degeneracy between the *d*-orbitals. These interactions are crucial toward understanding two factors that help direct the distribution of *d*-electrons: pairing energy and octahedral energy.[4,5] Pairing energy of the *d*-electrons refers to the energy related to two electrons occupying one orbital. The octahedral energy (Δ_o) is defined as the energy difference that arises between the t_2g (bonding) and e_g (antibonding) orbitals upon the coordination of a ligand to the metal ion.[4,5] Ligand field theory adequately delineates ligands into three categories based on their field splitting strength: weak, medium, and strong field.[1] An important aspect of this model is the spectrochemical series. The spectrochemical series is a categorization of ligands based on their ability to split the metal ion's *d*-orbitals.[1] The conventional series is outlined below in Scheme 1.0.

$$I^- < Br^- < S^{2-} < SCN^- < Cl^- < NO_3^- < N_3^- < F^- < OH^- < C_2O_4^{2-} < H_2O < NCS^- < CH_3CN < py$$
$$< NH_3 < en < bipy < phen < NO_2^- < PPh_3 < CN^- < CO$$

Scheme 1.0: Spectrochemical series ranging from small Δ_o to large Δ_o splitting; py is pyridine, en is ethylenediamine, bipy is 2,2'-bipyridine, phen is 1,10-phenanthroline, and PPh_3 is triphenylphosphine.

Weak field ligands are π-donors that typically possess lone pairs of electrons which form sigma-coordinate bonds to metal cations. This type of coordinate bond results in a small Δ_o energy barrier which translates to small splitting between the energy levels of the t_2g and e_g *d*-orbitals. The pairing energy of electrons is less favourable than the promotion of electrons to the e_g orbitals since the Δ_o barrier is easily overcome.[1,5] This effect explains why complexes with weak field ligands are often associated with high-spin state. Mid-field ligands have no π-character and are observed as either low or high spin complexes, depending on external perturbations like temperature, pressure or light. Strong field ligands act as π-acceptors being able to accept electron density from the metal through empty π*-orbitals in a process referred to as back bonding. Because strong field ligands render large Δ_o values due to better overlap with the metal ion's *d*-orbitals, the pairing energy of *d*-orbital electrons is more favoured which typically generate low-spin complexes.[1,5] Therefore, for octahedral complexes (O_h) with a d^4-d^7 metal ion there are two outcomes: low spin ($P<\Delta_o$) and high spin ($\Delta_o<P$). High to low spin transitions in d^4-d^7 transition metal coordination complexes lead to deviations in spin-only behaviour in molecular magnetism and can give rise to characteristic behaviour known as spin-crossover, most often seen among Fe^{2+} and Fe^{3+} species.[5,7]

1.3.0 Spin-crossover

Spin-crossover (SCO) is a molecular switching process between the HS and LS states observed for d^4-d^7 metal ions under an octahedral symmetry (O_h).[3,5] Spin-crossover is heavily

tailored to the magnitude of Δ_o and P. When Δ_o and P are comparable in energy then the LS and HS states also become equally energetic. The spectrochemical series provides a qualitative assessment for outlining the Δ_o and P parameters. However, a quantitative analysis is provided with the Jørgenson's equation using values determined by Ultraviolet-visible spectroscopy (UV-vis),

$\Delta_o = a_{TM} \times b_L \times 1000\ cm^{-1}$ where Δ_o is the difference in energy levels of the split *d*-orbitals; a_{TM} and b_L represent the crystal field splitting values determined experimentally by UV-visible spectroscopy, of the transition metal and ligand respectively.

Coordination complexes are able to undergo electronic transitions within the visible range of the electromagnetic spectrum. For this reason, UV-vis spectroscopy is a spectroscopic technique that uses light to probe for the electronic transitions between the frontier HOMO and LUMO orbitals.[7,39] The transitions from the ground to excited state are related to the absorption measurements. With regards to SCO, electronic absorption experiments can probe for the transfer of electrons between the molecular orbitals of the ligands and the *d*-orbitals of the metal ion. These transitions are prominent in UV-vis spectra and are referred to as charge transfer bands.[1] The transfer of electrons from the full molecular orbitals of the ligands to the empty or partially empty *d*-orbitals of the metal ion are referred to as ligand-to-metal charge transfer (LMCT) and often are observed with metal ions in higher oxidation states. Metal-to-ligand charge transfers (MLCT) arise in complexes containing π-acceptor ligands possessing low level orbitals that are empty, coordinated to metals in a low oxidation state.[1,5]

Structure elucidation by X-ray crystallography is a practical method for observing SCO behaviour. X-ray diffraction allows for the reconstruction of complete molecular structures from the diffraction pattern produced by the scattering of X-rays from a crystal. The waves of the X-rays that are scattered by the electrons of the atoms in the crystal must satisfy the angle at which

constructive interference occurs to produce the diffraction patterns. The angle at which constructive interference between the wavelengths occurs is given by Bragg's Law,

$$2d \sin\theta = \lambda$$

Bragg's Law defines the path length (*2d sin θ*) that the wavelength (λ) must follow for a crystal to diffract.[1,53] The diffraction patterns produce images or reflections by positioning the single crystal at varying orientations while being exposed to X-rays. These reflections generate a series of spatial arrangements between dark and light points which are translated through Fourier transformations into the 3-dimensional maps of electron density within the crystal. This method of structure elucidation is relevant for studying SCO behaviour because information regarding the coordinate bond lengths, spin states, intermolecular interactions, and packing structures can be measured. In SCO complexes the metal to ligand bond distances fluctuate since SCO behaviour is essentially an intra-ionic electron transfer between the t_2g orbitals and the e_g subset that possesses antibonding character.[53,54]

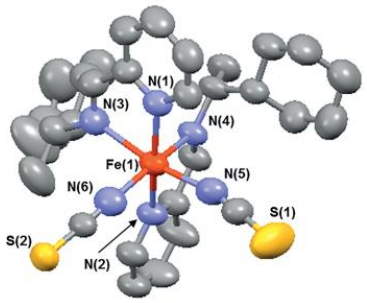

Figure 1.6: [Fe{(R)-α-methyl-*N*-(2-pyridinylmethylene)cyclohexanemethanamine}$_2$(NCS)$_2$] complex. Taken from *Eur. J. Inorg. Chem.* **2017**, 1049-1053.

The crystal structure obtained from single crystal X-ray diffraction of an Fe^{2+} complex, shown in Figure 1.6, reveals the Fe^{2+} center in an octahedral field to four nitrogen atoms from two chiral bidentate ligands and two thiocyananto ions arranged in a *cis* configuration.[49] Information about the spin state of the iron can be obtained from the relative bond lengths calculated from the

crystal structure. Here, the Fe-N(1) and Fe-N(2) coordinate bonds from the pyridine are 2.188(5) Å and 2.195(4) Å, respectively.[49] The bond distances of 2.292(5) Å for Fe-N(3) and 2.240(6) Å for Fe-N(4) from the imine were found to be even longer than those of the pyridine.[49] These Fe-N bond lengths at 278 K are commonly associated with high-spin Fe^{2+} species.[7,49]

1.3.1 Thermodynamics of Spin-crossover

The energetics of SCO are thermodynamically modeled by the Gibbs free energy equation,

$$\Delta G = \Delta H - T\Delta S$$

The parameters ΔH and ΔS define enthalpy and entropy, respectively. In a more comprehensive view, ΔS is the significant driving force behind the transition to HS from LS and is defined as,

$$\Delta S = S_{HS} - S_{LS}$$

$$S = RlnW$$

where R represents the gas constant in $J{\cdot}K{\cdot}mol^{-1}$ and W represents the number of permutations for the LS and HS configuration

Temperature is a factor of the entropic value and therefore plays a significant role behind the driving force. At low temperatures the Crystal Field Stabilization Energy (CFSE) is maximized which describes an enthalpic effect.[4,7] Conversely, at high temperatures an entropic effect is observed since the number of unpaired electrons increases and maximizes the entropy of the system. Therefore for a SCO system, ΔH will be the dominating parameter at low temperatures and dictate a LS state while ΔS will dominate at high temperatures and dictate a HS state to exist.[3,4,5] In a coordination complex the metal ion's electrons are no longer in an atomic orbital

but rather a molecular orbital due to the covalency of the system. This essentially translates to the metal ion's electrons being more delocalized which reduces electron repulsion.

1.3.2 Types of Spin-crossover and Thermal Hysteresis

Generally, the abruptness in spin-crossover is defined by the cooperativity of the system which originates from the propagation of each coordination complex through intermolecular interactions.[5,7] These intermolecular interactions are a result of π-π stacking, hydrogen bonding, or halogen interactions and they can also be effected by the size of counter ions in charged complexes or saturation with solvent molecules. [5,7] Because spin-crossover complexes can exhibit characteristic responses to an applied magnetic field a suitable means of measuring the magnetic susceptibility of a SCO complex is to move the complex in and out of a magnetic field and examine its response.[4,5,7] In modern research this is accomplished by a Super Conducting Quantum Interference Device (SQUID). A SQUID is a highly sensitive magnetometer that detects the magnetization induced in a sample from exposing it to a magnetic field through a series of superconducting coils.[2,3] The magnetic susceptibility of the sample is related to the differences in potential read from the SQUID magnetometer. Because magnetization and temperature are the two variables in a SQUID analysis, the measurements are collected as a function of magnetization at a constant temperature or magnetization in a fixed field. [2,3] The magnetic measurements obtained can indicate the degree of switching in the complex.[8]

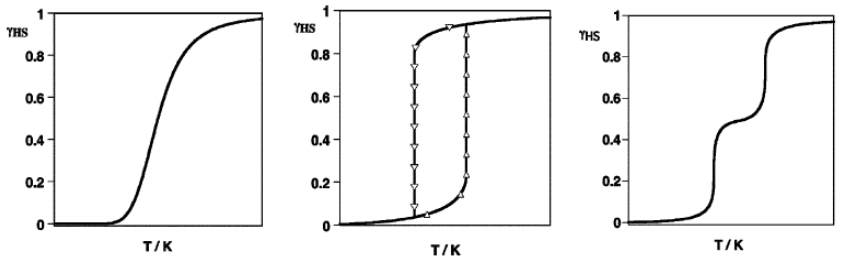

Figure 1.7: High spin molar fraction γ_{HS} against temperature (T in Kelvin) transition curves: gradual (left), abrupt with hysteresis (middle), and stepped (right). Taken from *Dalton Trans*., **2005**, 2062-2079.

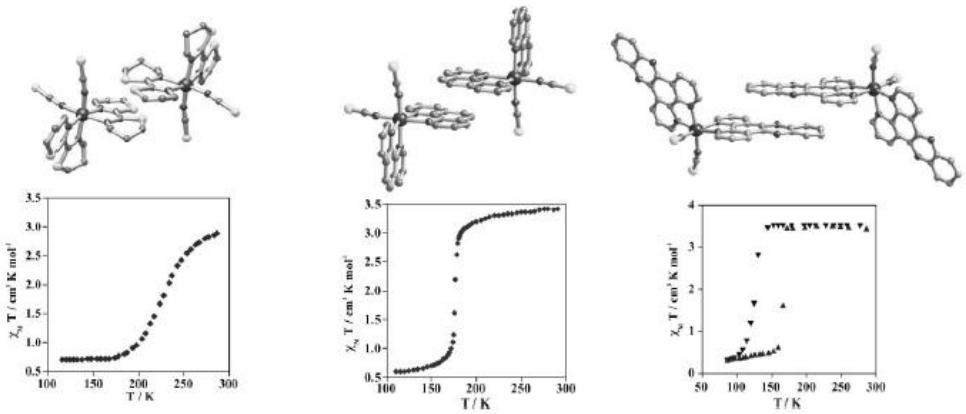

Figure 1.8: Degree of intermolecular interactions as they are related to SCO types presented in the form of $\chi_M T$ against temperature for the complexes: $[Fe(btz)_2(NCS)_2]$ (left), $[Fe(phen)_2(NCS)_2]$ (middle), $[Fe(dppz)_2(NCS)_2]$·pyridine (right). Taken from *Dalton Trans*., **2005**, 2062-2079.

The cooperative interaction of the molecules that makeup SCO materials originates from the change in volume of each molecule as seen through X-ray diffraction.[5,7,8] The structural changes or growth in the crystal lattice often propagate systematically as neighbouring molecules affect one another. This process of propagation of the metal ions throughout a material by means of coordinate bonds and intermolecular interactions can be induced by temperature and is known as thermal hysteresis.[3,5] From a thermodynamic standpoint if ΔH and ΔS represent the enthalpic and entropic variations per mole of spin transitioning centers then the ratio of $\Delta H/\Delta S$ relates to the temperature at which an equal number of LS and HS complexes exist, known as $T_{1/2}$.[3,5] The cooperativity effect depends on the intermolecular interactions as demonstrated by the monomeric iron complexes presented in Figure 1.8. The btz ligand is aliphatic and based from

crystal structures the packing of the complex lacks any appreciable intermolecular interactions. The phen ligand is aromatic and shows more significant C···C contacts in comparison to btz. The dppz has an extended aromatic system and show more enhanced C···C contacts. As these intermolecular interactions become tighter the consequent SCO effect becomes more cooperative.[5,13] In principle the synthetic approach taken toward enhancing cooperativity is to design systems with cohesive intermolecular interactions like hydrogen bonds and π-π interactions. Because first-order transitions usually accompanied by hysteresis allow for a degree of elasticity or memory they render the material more suited for coding applications while more abrupt behaviour is desired for use as switches.[3,5,7] A well-known example of a wide thermal hysteresis loop at room temperature is observed from the complex [Fe(*N*-(8-quinolyl)salicylaldimine)$_2$]NCSe MeOH.

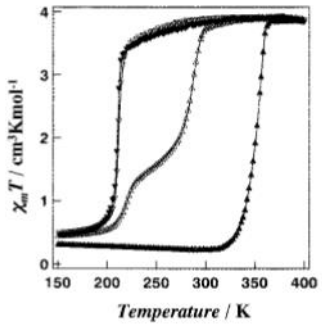

Figure 1.9: $\chi_m T$ *vs T* plot for [Fe(*N*-(8-quinolyl)salicylaldimine)$_2$]NCSe MeOH. Taken from *J. Am. Chem. Soc.*, **2001**, 123, 11644-11650.

The wide hysteresis loop is mainly attributed to the intermolecular π-interactions between the quinoline and phenyl rings of the *N*-(8-quinolyl)salicylaldimine ligands.[52] *N*-(8-quinolyl)salicylaldimine (Qsal) is a thoroughly studied multidentate ligand in coordination chemistry that is known to associate with SCO behaviour in coordination complexes.[5,7,52] The Qsal ligand has been recognized as an exemplary Schiff base type ligand that features a multidentate N_2O coordination site illustrated quinolylsalicylaldimine type Lewis bases have

been shown as exceptional ligands that associate with SCO in both Fe^{2+} and Fe^{3+} complexes, due to their involvement in hydrogen bonding and intermolecular π-π interactions as illustrated below in Figure 1.10.[54]

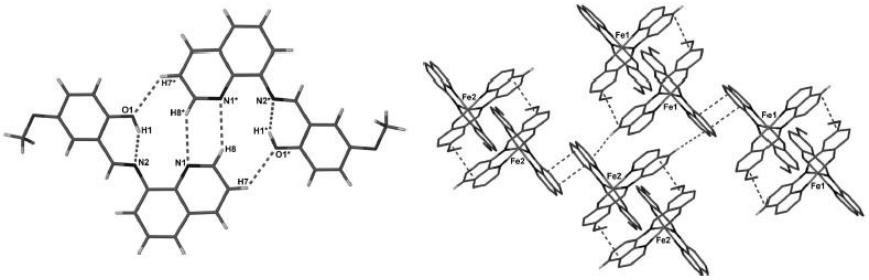

Figure 1.10: C-H···N, C-H···O and O-H···N interactions of HQsal-5-OMe (left). π-π interactions of $[Fe(Qsal\text{-}5\text{-}OMe)_2]Cl{\cdot}2MeOH{\cdot}0.5H_2O$ forming HS and LS chains (right). Taken from *Chem. Eur. J.*, **2013**, 19, 1082-1090.

The changes in the chemical environment of a nucleus that reflect its coordination sphere, oxidation state and magnetic properties can be probed using Mössbauer spectroscopy. Mössbauer spectroscopy is a spectroscopic technique that works on the resonant emission and absorption of gamma (ɣ) radiation without recoil by atomic nuclei in a lattice.[4] The emission and absorption of ɣ-radiation without recoil is known as the Mössbauer effect and it is highly sensitive toward specific nuclear energies as they are related to their electronic environment. There are distinct nuclei that are more suitable over others for Mössbauer measurements based on their decay time and nuclear excitation.[4] For this reason, ^{57}Co nuclei that decay to an excited state of ^{57}Fe by electron capture are used in Mössbauer spectroscopy. Because this technique distinguishes subtle changes in the energy levels of atomic nuclei, information about oxidation state and spin state can be reasoned from two parameters: the isomer shift (δ) and the quadrupole splitting (ΔE_Q).[54] The isomer shift, analogous to a chemical shift, is given by the difference between the absorption of radiation at the energy required to excite the nucleus from its ground state to the excited state. Isomer shift values, expressed in velocity units of mm/s, can infer the

oxidation state of a metal ion based on the difference in energies that are dependent upon the electron density at the nucleus.[54] More specifically, the *s* electron as it relates to shielding effects from the *p* and *d* electrons. The quadrupole splitting is another nuclear interaction that provides additional information about the spin state of the metal ion. The changes in these nuclear interactions for SCO complexes generate unique spectra as shown below in Figure 1.11.

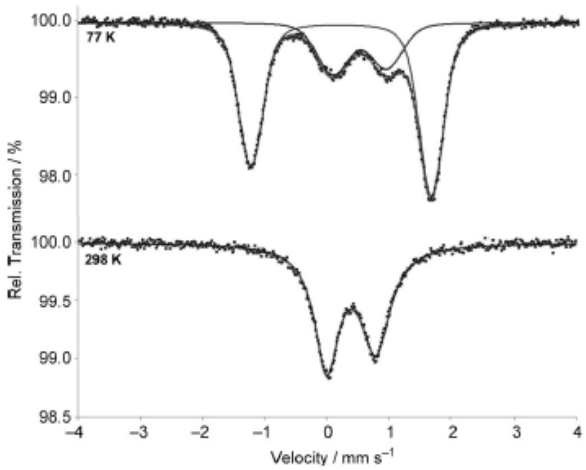

Figure 1.11: Mössbauer data of $[Fe(Qsal\text{-}5\text{-}OMe)_2]Cl{\cdot}MeCN{\cdot}H_2O$ complex at 298 K (bottom) and 77 K (top). Taken from *Chem. Eur. J.*, **2013**, 19, 1082-1090.

Figure 1.11 shows the Mössbauer spectra of an $[Fe(Qsal\text{-}5\text{-}OMe)_2]Cl{\cdot}MeCN{\cdot}H_2O$ spin-crossover complex at room temperature and 77 K. Upon cooling, the complex gives rise to an asymmetric doublet that begins to form with an δ value of 0.20 mm/s and a ΔE_Q value of 2.89 mm/s. These values for both parameters are indicative of LS Fe^{3+}.[15] The HS Fe^{3+} centers, having an δ value of 0.52 mm/s and a ΔE_Q value of 0.86 mm/s are noted to exist in a fraction of 28% compared to LS at 77 K.[54] Because the number of *d*-electrons in Fe^{2+} is greater than Fe^{3+}, Fe^{2+} centers experience a greater shielding effect from the *s*-electrons which results in more positive δ values.[5,54] The presence of two distinct LS and HS Fe^{3+} centers is understood by the presence of the C-H···π and π-π interactions of fluctuating strengths.[54] Magnetic susceptibility measurements exhibited by this complex abruptly decrease as the sample is cooled below 150 K, suggestive of half SCO

occurring which is consistent with the Mössbauer data in which one Fe center is LS and another Fe center in HS.[54]

1.3.3 Multifunctional Materials – Spin-crossover and Electrical Conductivity

Multifunctional materials are single molecule-based materials that can feature unique combinations of physical properties that are otherwise not naturally observed together.[2,3] Synthetic strategies toward these types of materials offer the opportunity to combine SCO with electrical conductivity to produce semi-conducting SCO hybrid materials. Electrical conductivity is the measure of a material's ability to carry an electric current.[1] Therefore, a material with low resistance to the flow of an electric current would act as an exceptional electrical conductor.[1] Band theory aptly models how well a material can conduct an electric current. In Band theory the energy levels in a material arise from the overlap of a large number of atomic orbitals to produce a number of molecular orbitals.[2,3,42] These molecular orbitals are closely spaced in energy and as a result form an almost continuous band of energy levels which are separated by gaps. The electrons in the material populate the band structure in a manner that minimizes the total energy starting from the lowest energy state. However, only a single electron can occupy each state as described by the Pauli Exclusion Principle which states that identically charged particles with half-integer spins cannot occupy the same quantum state.[2,3,42] This means that as the band structure is populated by the electrons, the electrons will eventually reach a highest occupied energy level. This level is characteristic to each material and is referred to as the Fermi level.[2,3,42] The Fermi level and its position within the band structure is crucial toward the ability to conduct an electric current as electrons near the Fermi level have the ability to move and occupy other states within that region. The most crucial bands closely associated with the Fermi level are the valence band and conduction band. The valence band is the highest state

at which the electrons occupy at absolute zero temperature.[2,3,42] The conduction band holds the lowest array of unoccupied and available energy states. Now with regards to metal coordination complexes, the electrical conductivity arises from a partially filled band structure where the valence and conduction bands overlap, allowing for the electrons to delocalize more readily near the Fermi level. The delocalization of electrons into the conduction band is what gives rise to electrical conductivity in a metal complex.[2,3,42] Species that are considered semi-conductors possess narrow gaps between these bands which require an input of energy for the electron to cross.[2,3,42] As the gaps between these bands expands and become too energetically unfavourable to cross then the species is described as an insulator demonstrating poor electrical conductivity.[4] As with the entropic effect in SCO, temperature also plays a role in electrical conductivity. An increase in conductivity is often observed with decreasing temperatures. This is due to the fact that at low temperatures the resistivity or irregularities within the crystal lattice of the metal complex are reduced.[2,3,42] The interest behind pairing SCO with electrical conductivity is largely due to the synergistic effects among the different physical properties which can lead to behaviours desirable for switches and sensors or data storage and display units that function on the bi-stability between the LS and HS states within a certain temperature range.[4,5,42]

The relatively large structural changes between the HS and LS states of SCO can function as a switch for the electrical conductivity in hybrid materials.[3,11,50] Two approaches are typically considered for the preparation of materials that exhibit SCO with electrical conductivity. The first approach involves combining conducting anions and SCO cations within the same crystal lattice.[50] The second approach involves the use of redox-active ligands that possess conducting moieties to form metal coordination complexes.[50] To visualize this synergistic effect, consider

an Fe^{2+} SCO complex that shows semiconducting behaviour as a function of temperature outlined in Figure 1.12.

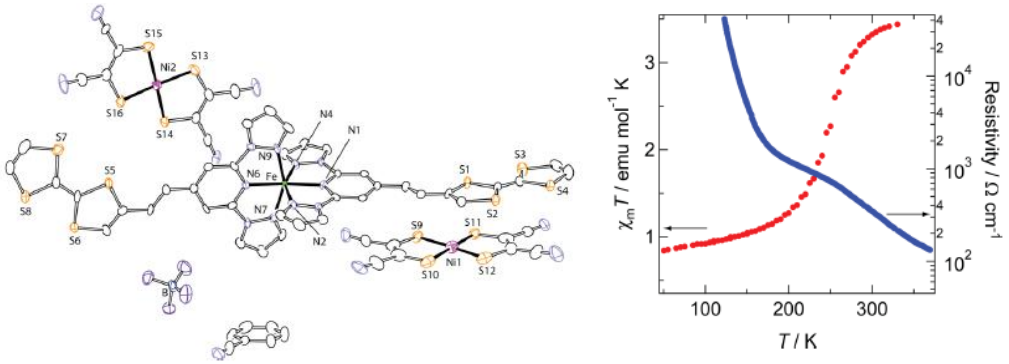

Figure 1.12: Crystal structure of $[Fe(dppTTF)_2][Ni(mnt)_2]_2(BF_4)\cdot PhCN$ (left); (dppTTF = 1-{2-(1,3-dithiol-2ylinene)-1,3-dithiolyl}-2-{2,6-bis(1-pyrazolyl)pyridyl}-ethylene, mnt = maleonitriledithiolate). Plots of $\chi_M T$ measurements and resistivity as a function of temperature (right). Taken from *Dalton Trans.*, **2011**, 40, 2154-2156.

Typically in semiconducting materials the resistivity decreases with increasing temperature.[4] The inflection observed in the resistivity plot coinciding with the spin transition indicates a level of cooperation between the two functions.[5,50] Upon lowering the temperature to the range of 160-280 K, which typically corresponds to spin transition in iron centers, a variance was observed in the complex's properties.[50] The correlation between the gradual SCO behaviour with the subsequent large structural changes as a function of temperature and the variation of the electrical conductivity has been rationalized by the chemical pressure induced by SCO in the Fe^{2+} ion.[50]

Recently, a pair of Fe^{2+} complexes with chiral (*R*)/(*S*)-4,5-pinenepyridyl-2-pyrazine ligands that can undergo SCO and dielectric switching processes have been synthesized. Structurally, the *R*-enantiomer form of the complex connects to neighbouring complexes through a C···N contact forming a weak pseudodimer.[27] These pseudodimers can engage in π-π contacts through the pyridyl and pyrazine components. The magnetic moments of both complexes were found to be weakly temperature dependent between 250 K to 300 K.[27] Spin-crossover from Fe^{2+}

HS (S=2) to Fe^{2+} LS (S=0) was recognized from the decreasing $\chi_M T$ value with decreasing temperatures and both complexes displayed a weakly hysteric one-step complete SCO at 187 K. The C-H···N and π-π contacts were noticed to become weaker upon transitioning from LS to HS states.[27] This SCO was accompanied by a significant change in the dielectric constant as a result of their chirality. These types of materials are highly desired to expand information storage, sensor technology, and switching applications due to their coupled properties that can be regulated by temperature, light, pressure and electric or magnetic fields.[3,27,50]

1.3.4 Heteroleptic and Homoleptic Spin-crossover Complexes

A recent example of a heteroleptic complex $[Fe(bpte)(bim)]^{2+}2X^-$ exhibits temperature induced gradual SCO. The complex was synthesized by reacting the corresponding Fe^{2+} salt (X= ClO_4^-,BF_4^-, OTf^-) with an equivalent mixture of the bpte and bim ligands.[15] The significance behind this complex is its expansion of coordination environments with N_4S_2 donor atoms.

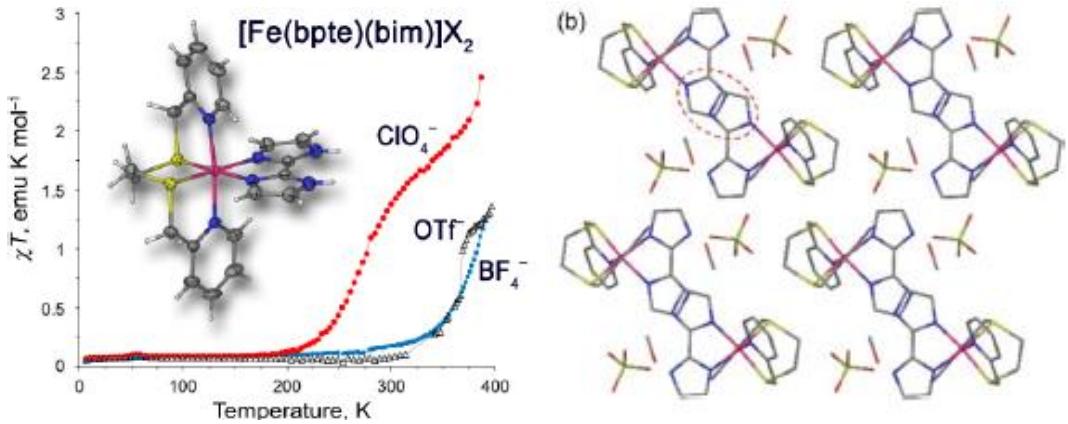

Figure 1.13: Anionic tuning of $[Fe(bpte)(bim)]X_2$ (bpte= *S,S'*-bis(2-pyridylmethyl)-1,2-thioethane; bim= 2,2'-biimidazole and X= ClO_4^-,BF_4^-, OTf^-). Taken from *Inorg. Chem.*, **2017**, 56, 11096-11103.

Distances measured at 230 K between the Fe-N coordinate bonds fall within the range of 2.003(2)-2.004(2) Å for each complex.[15] The Fe-S coordinate bonds fall between 2.231(2)-2.244

Å. These bond distances are recorded to be characteristic of LS Fe^{2+} ions.[5,15] The packing structure of $[Fe(bpte)(bim)]^{2+}2ClO_4^-$ appear as dimers in columns that are weakly coupled by π-π interactions between the imidazole rings of the bim ligands with an interplanar distance of 3.45 Å. The gaps within the columns are occupied by the ClO_4^- anions and MeOH solvent molecules.[15] The gradual SCO is attributed to the low cooperativity of interactions between the cationic links.[15] The VT-magnetic susceptibility measurements reveal that each complex is indeed LS Fe^{2+} as indicated by the near zero values of χT. The SCO onset observed strongest for $[Fe(bpte)bim)]^{2+}2ClO_4^-$ complex at 230 K. The conversion between the LS to HS state is gradual and occurred in two steps as indicated by the inflection point in the χT vs T curve at around 300 K with χT measured at 1.60 emu·K·mol^{-1}. [15]

Octahedral Co^{2+} (d^7) complexes can exhibit thermal spin-crossover between the high-spin state (S = 3/2) and low-spin state (S = 1/2).[5,7] In contrast to Fe^{2+} spin-crossover complexes, Co^{2+} requires a greater field strength to transition to the low-spin state where the *Jahn-Teller* distortion is active.[5,48] The structural changes attributed from changes in donor to metal coordinate bond distances in spin-crossover are smaller for Co^{2+} compared to Fe^{2+} or Fe^{3+}, which also reflects the smaller change in spin state. For this reason, spin-crossover of Co^{2+} systems is typically more gradual and incomplete. An example of a Co^{2+} spin-crossover complex is presented below in Figure 1.14.

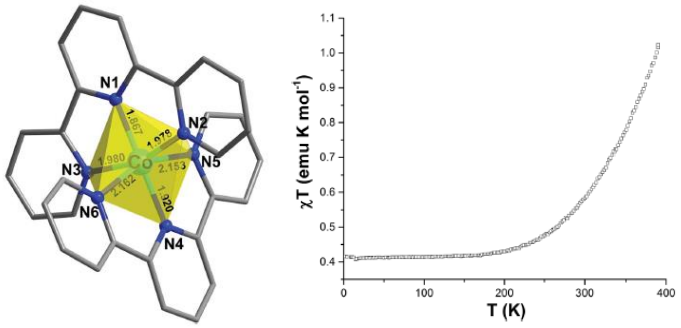

Figure 1.14: Coordination sphere of Co^{2+} with labeled Co-N bond distances (Å) at 100 K (left). Molar susceptibility measurements (χT) as a function of temperature (right). Taken from *Chem. Sci*., **2006**, 7, 1569-1574.

The $\chi_M T$ data between 180-190 K indicate that virtually all of the Co^{2+} atoms are in the LS state.[48] The gradual decrease in $\chi_M T$ values at 390 K indicates that the HS state is not fully populated in comparison to the $\chi_M T$ value of 1.88 emu K mol^{-1}, which is typically expected for spin-only HS Co^{2+} ions.[48] The unique characteristics of this Co^{2+} complex stem from its conducting behaviour as it relates to the gradual SCO observed. As previously stated, Co^{2+} requires a greater field strength to transition to the low-spin state where the *Jahn-Teller* distortion is active.[5,48] The structural variation given by the transition from HS to LS and the resulting *Jahn-Teller* distortion in the LS state contribute to the conducting behaviour of this complex.[48]

There are few examples of SCO complexes with chromium ($3d^5$) and manganese ($3d^5$) metal centers. A particular example comes from some computational studies of spin state flexibility as a function of metal valency in redox-active transition metal complexes.[17] Spin-crossover coupled with electron transfer by complexes in the form of $[M(tacn)_2]^{3+/2+}$ (M= Cr, Mn, Fe, Co, Ni) were modeled using density functional theory (DFT) calculations and compared with experimental redox properties of complexes in the form of $[M(NH_3)_6]^{n+}$.

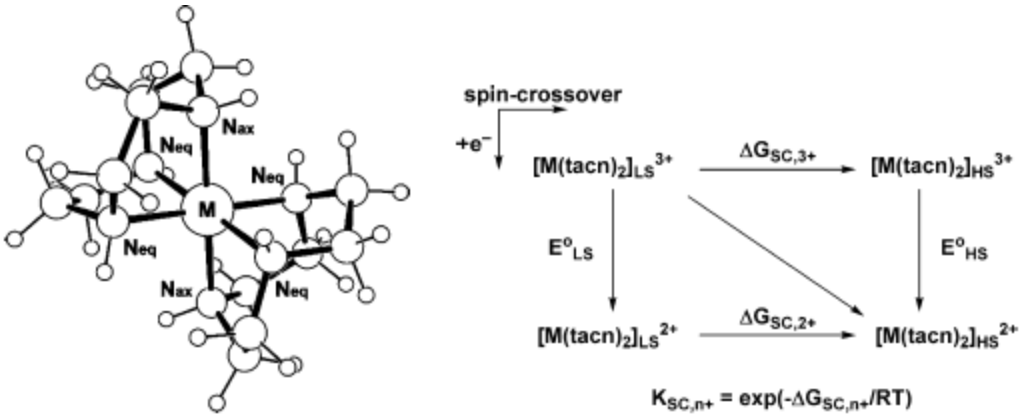

Figure 1.15: Structure of $[M(tacn)_2]^{n+}$ complex (tacn= 1,4,7-triazacyclononane; M= Cr, Mn, Fe, Co, Ni) and schematic of decoupling of SCO (horizontal) from electron transfer (vertical). Taken from *J. Am. Chem. Soc*., **2009**, 131, 6189-6197.

The relationship between spin decoupled electron transfer and spin-crossover thermodynamics modeled by,

$$-nF\left(E^{\circ}_{HS} - E^{\circ}_{LS}\right) = \Delta G_{SC2+} + \Delta G_{SC3+}$$

describes the spin state energy dependence on oxidation state change. In this study the tacn ligand offers shorter M-N bond distances and N-M-N bond angles that deviate from 90° which provided a means for manipulating spin state energetics for metal ions where multiple spin states are accessible.[17] Previously measured redox potentials for $M^{3+/2+}$ of -1.14 and +0.62 V versus a Normal Hydrogen Electrode (NHE) for Cr and Mn (with 0.1 M LiClO4 and 0.1 M KCl supporting electrolyte in water) are comparable to the DFT predicted reduction potentials of -0.991 and +0.462 for Cr and Mn respectively, within an error of 160 mV. Reduced species tend to favour HS configurations while oxidized species favour LS states.[17] The HS configuration in Mn^{2+} is more stable than LS due to the half-filled $t_{2g}^3e_g^2$ electron configuration. However, spin state accessibility for Cr^{2+} is not well documented, with mostly LS examples involving strong field ligands like CN^- or dinuclear bridging complexes.[16,17] Greater positive values for E_{HS} versus E_{LS} for both Cr and Mn tacn complexes were noted with SCO and coupled electron

transfer proceeding from the LS M^{3+} state to the HS M^{2+} state. However, the accurate prediction of spin state energy differences for pseudo-octahedral transition metal complexes like these and the functionals applied to estimate their exchange energies remains challenging since open shell systems are multiconfigurational.[17]

1.4.0 Redox-active Arylazo Ligands

Redox chemistry is the transferring of electrons between two species. Unlike charge transfers that are observed from UV-vis spectroscopy as a result of electronic transitions in excited states rather than ground states, redox processes involve the oxidation or loss of electrons of one species and a reduction or acquiring of electrons by another species.[1,2] Often in literature the terms innocent and non-innocent are used as descriptors for ligands that are associated with redox-activity in coordination complexes. Innocent ligands unambiguously determine the metal centers' oxidation state upon their binding and formation of a coordination complex.[1,32] A non-innocent ligand is one in which the oxidation state is not obvious or easily predicted and often differs from its experimentally determined oxidation state.[1,32] Generally, redox-active non-innocent ligands possess more accessible energy levels and are therefore more susceptible to changes in their oxidation number.[32]

A particular class of redox-active compounds being explored for use as ligands in coordination chemistry are arylazo compounds. Arylazo compounds feature a diimide bond with aromatic or aryl substituents that most often include some *N*-heterocycle such a 2-pyridylidine. These are multi-dentate ligands that coordinate to metal ions with their nitrogen atoms from the azo bonds and pyridylidine rings, as well as an anionic oxygen donor. The low-lying π^* molecular orbital of the azo group and its accessibility for electronic transitions is appealing toward generating molecular electronic features.[32] It is also responsible for the intense longer

wavelength absorptions observed among the visible region from these compounds.[33,34] More specifically, this low-lying π* orbital centered on the azo group fits well into the frontier orbital structure of a coordination complex and can be populated by one or more electrons giving rise to a multi-step reduction pathway.[32]

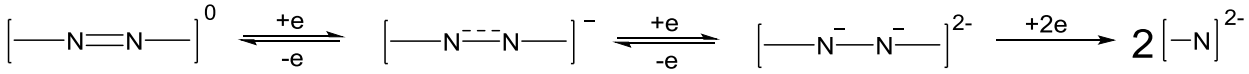

Scheme 1.1: Multistep reduction pathway of azo bonds. Taken from *Dalton Trans.*, **2012**, 41, 2213-2226.

The first and second intermediate species from the multi-step reduction process are reversible. The first reduction gives rise to a stable radical anionic form which introduces some paramagnetic character to the system. This paramagnetic character can in turn influence the π stacking or electrical conductivity of the system which can favour more cooperative spin transitions and conduction properties.[4,5,32] Subsequent reduction of the radical anionic intermediate results in a fully reduced hydrazido$^{(2-)}$ species. Further reduction of the hydrazido$^{(2-)}$ species leads to the cleavage of the N=N bond as a result of forming the closed shell dianion.[32] Therefore, the reductive population of the azo-centered molecular orbital with one or two electrons in an open or closed shell electronic configuration can give rise to ligands that have the capacity to generate interesting electronic and structural properties.

1.4.1 Examples of Redox-active Arylazo Ligands and Their Electrochemical Profile

The arylazo ligand 1-(2-pyridylazo)-2-phenanthrol (Papl) is a tridentate ligand that features a N_2O binding structure. It is formed from reacting 2-hydrazinopyridine with 9,10-phenanthrenequinone under acidic conditions.[34]

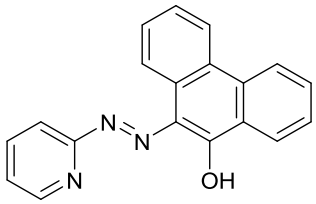

Figure 1.16: Molecular structure of 1-(2-pyridylazo)-2-phenanthrol (Papl).

Typically in coordination reactions Papl has been used to generate complexes of the form $[M(Papl)_2]$ with some divalent or trivalent transition metal ions (M= Mn^{2+}, $Co^{3+/2+}$, Zn^{2+}). Some of these complexes with this ligand have been shown to undergo reversible redox chemistry and SCO behaviour.[34] The ligand also undergoes tautomerization between the keto and enol form in solution. Possessing the ability to tautomerize offers possibilities toward reversible intramolecular electron transfer processes by either a redox-induced electron transfer or through valence tautomerism.[34]

Another studied phenanthrol-based arylazo compound known as 10-(8-quinolylazo)-9-phenanthrol (Qapl) also features a N_2O binding structure but bears a quinoline substituent.

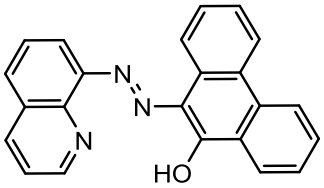

Figure 1.17: Molecular structure of 10-(8-quinolylazo)-9-phenanthrol (Qapl).

The compound is made from reacting 8-hydrazinoquinoline with 9,10-phenanthrenequinone and, unlike Papl, Qapl does not undergo a keto-enol tautomerization in solution.[33]

Electron transfer processes are fundamental toward the reactivity of coordination complexes, especially with regards to redox-active ligands, and molecular electrochemistry relates the flow of electrons to chemical changes.[17] The fundamental value behind electrochemistry is the capability of changing the identity of the species used as the reductant to

allow for easier measurements of the thermodynamic and kinetic parameters that govern the driving force of a reaction. Cyclic Voltammetry (CV) is a convenient electrochemical technique commonly used for studying the oxidation and reduction processes of coordination complexes.[63] The data is presented as a voltammogram and represents the profile of the electrical current that develops in response to an applied potential. The voltammogram of Qapl (green trace) is shown below overlaid with the complex $[Co(Qapl)_2]^+Cl^-$ (red trace) in Figure 1.18.

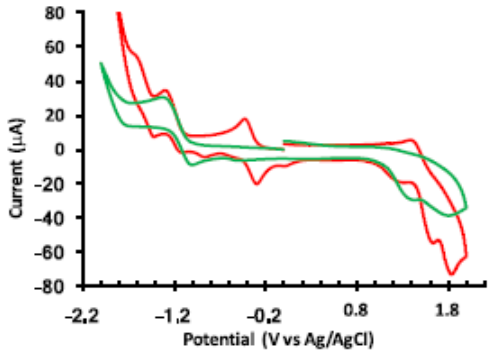

Figure 1.18: Electrochemical profiles of Qapl (green) and $[Co(Qapl)_2]^+Cl^-$ (red). Taken from *Polyhedron*, **2017**, 131, 34-39.

The cathodic trace is the forward scan of the voltammogram that shows the potential swept negatively from the starting potential 0 V to the switching potential of approximately -2.0 V at a scan rate of 100 mV/s.[33] The reverse scan where the potential is swept positively back to the starting potential is the anodic trace.[63] The peaks read in a voltammogram are described by the Nernst equation,

$$E = E^0 + \frac{RT}{nF} ln \frac{[Ox]}{[Red]} = E^0 + 2.3026 \frac{RT}{nF} log_{10} \frac{[Ox]}{[Red]}$$

The Nernst equation relates the potential of an electrochemical cell (E) to the standard potential of a species (E^0) and the relative activities of the oxidized [Ox] and reduced [Red] analyte in the system at equilibrium.[63] The formal potential is distinct to each experiment based on the conditions applied and is often estimated experimentally from the average potential value ($E_{1/2}$)

between the maximum and minimum peak values. The average potential value can help with estimating the E^0 value for a reversible electron transfer process which can be applied to the Nernst equation to determine how a system will respond to a change in the electrode potential or a change in concentration of the species.[63] The green trace representing Qapl exhibits a semi-reversible cathodic wave at -1.1 V (vs Ag/AgCl) as a result of the reduction of the N=N azo π-antibonding character which lies in the LUMO of the ligand. At high potential there is an irreversible anodic process.[33] The combination of the semi-reversible cathodic and irreversible anodic process lends stability to the radical anionic intermediate formed from the reduction of the azo group. The electrochemical profile of the $[Co(Qapl)_2]^+Cl^-$ complex shows two cathodic processes at potentials higher than -1.0 V (vs Ag/AgCl) that correspond to the ligand-centered reductions which are distinctive for arylazo ligands.[19]

1.5.0 Project Outline

This thesis takes on a synthetic approach toward generating heteroleptic redox-active complexes with the potential for spin-crossover. The rationale behind using a redox-active ligand stems from the low-lying nature of the π* orbital of the azo which makes it susceptible to multi-step reductions that give rise to radical intermediates. These intermediate forms would provide paramagnetic character to the system that can influence the π-stacking. There is also the possibility of some reversible intramolecular electron transfer process by either a redox-induced electron transfer or by valence tautomerism.[30,44] Here, the focus would be on the magnetic exchange interactions of a transition metal complex as a result of the singly reduced form of the arylazo ligand. Uniting a redox-active arylazo ligand with *N*-8-quinolylalicylaldimine to form a mixed ligand complex that holds a d^4-d^7 metal ion may promote greater intermolecular π-interactions that lead to enhanced cooperativity between the metal centers. Such complexes that

combine multiple physical properties like spin-crossover paired with electrical conductivity within a single component hold significance to multifunctional materials.[3,5] The initial course of action involves coordinating the monoanionic versions of these ligands to a Fe^{3+} center in order to lead to the mixed ligand charged complexes.

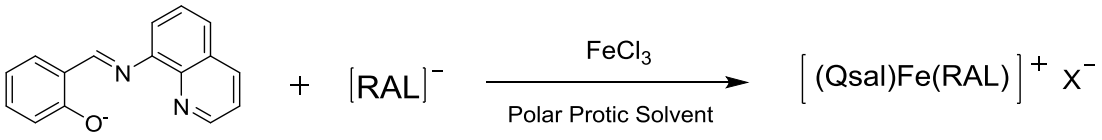

Qsal

Scheme 1.2: Theorized reaction path toward heteroleptic Fe^{3+} complexes.

The synthetic routes and targets will expand to incorporate different d^4-d^7 metal ions that possess the electronic configuration for potential spin-crossover, as well as other ligands like halogen substituted Qsal and various arylazo ligands.

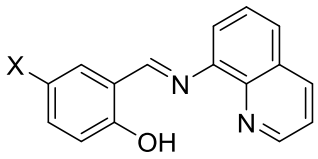

X-Qsal
(X=Br, Cl)

Figure 1.19: Molecular structure of halogenated-Qsal ligand.

Halogenated Qsal could offer halogen bonding effects and introduce additional intermolecular interactions to the systems.[57,79] Some other redox-active arylazo ligands that can be explored are shown in Figure 1.20.

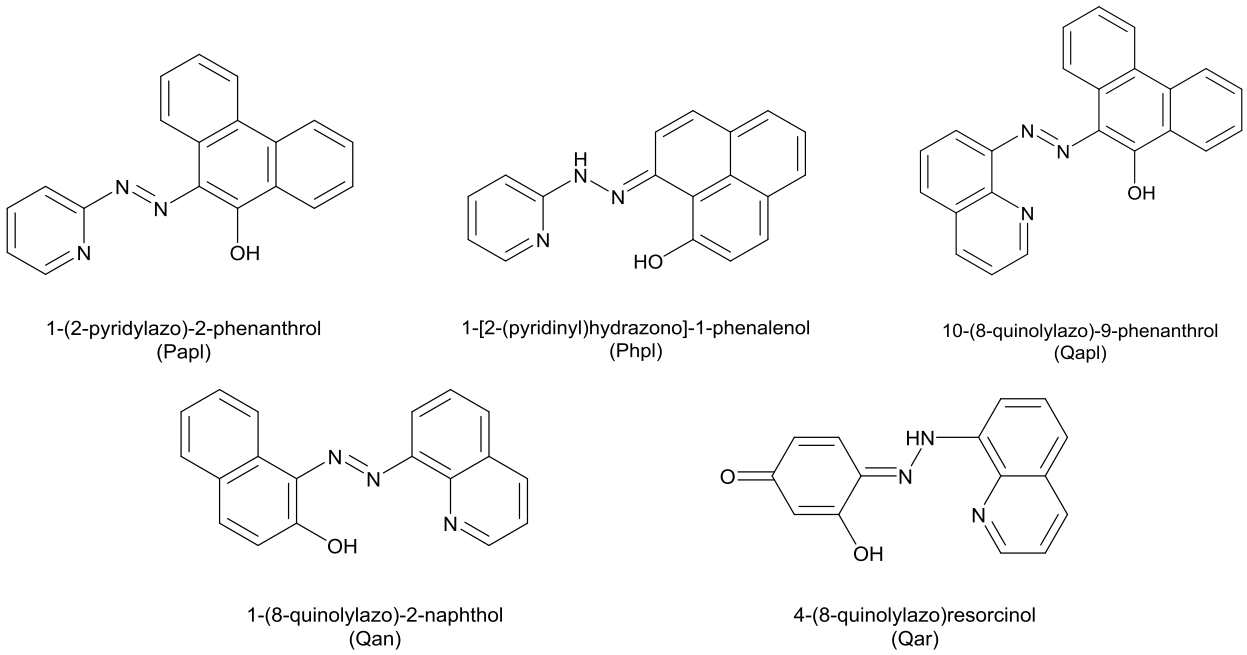

Figure 1.20: Molecular structures of proposed arylazo ligands.

Generating the cationic complex will allow for the anionic tuning of the counter ions. The ability to tune the counter ion is a crucial aspect toward studying the properties of these complexes. Counter ions can be influential toward the packing of the complexes and any potential spin-crossover behaviour. The counter ion can also affect the conductivity, solubility, and crystallization of the complex. Crystals that are suitable for X-ray diffraction are highly desired for structure elucidation, observing asymmetric units, and packing structures. In cases where crystallization is unattainable, characterization of the complexes by combustion analysis (CHN), Mass Spectrometry (MS), and Fourier-Transform Infrared Spectroscopy (FT-IR) will be of great value. The magnetic properties and magnetic susceptibilities can be investigated using Mössbauer, EPR, and SQUID if permitted in a solid-state analysis while susceptibility measurements can be obtained in solution by Evan's method.

Chapter 2.0 Experimental Details

All commercially available reagents and solvents were purchased from Sigma Aldrich, Fisher Scientific, or Tokyo Chemical Industry Co., Ltd. (TCI) and were used as received unless otherwise stated. Deaerated and anhydrous solvents were obtained from a distillation or from a Puresolve PA MD-4 solvent purification system, and all air or moisture sensitive reactions were carried out using standard Schlenk techniques. Elemental analyses were carried out by Atlantic Microlab Ltd., Norcross, GA, USA.

2.1.0 Instrumentation

All instrumentation is located at Brock University unless otherwise specified.

2.1.1 Nuclear Magnetic Resonance Spectroscopy

Nuclear Magnetic Resonance spectrometry on a Bruker Avance III HD 400 Digital NMR Spectrometer with a 9.4 Tesla Ascend Magnet was used for ^{1}H and ^{13}C NMR to analyze ligand and organic structures. Bruker Avance AV 600 Digital NMR Spectrometer with a 14.1 Tesla Ultrashield Plus magnet was used for Evans method.

2.1.2 Mass Spectrometry

MS Electrospray Ionization (ESI) spectra of both ligands and metal coordination complexes were produced from a Bruker HCT Plus Proteineer LCMS Mass Spectrometer.

2.1.3 Fourier Transform Infrared Spectroscopy

FT-IR spectra for the identification of functional groups and presence of counter ions were recorded on a Shimadzu IR Affinity-1 Spectrometer in the form of a solid KBr disk.

2.1.4 Ultraviolet-visible Spectroscopy

UV-visible spectra were recorded on a Shimadzu 3600 UV-vis-NIR spectrophotometer using suitable solvents in a 1 cm quartz cuvette. Variable temperature UV-vis experiments were controlled using a Specac variable temperature cell and temperature controller.

2.1.5 Electron Paramagnetic Resonance

Electron Paramagnetic Resonance experiments were recorded using a Bruker Elexays E580 pulse spectrometer.

2.1.6 Superconducting Quantum Interference Device

Variable temperature magnetic susceptibility measurements were recorded using a Quantum Design SQUID magnetometer with a 5T magnet and a Quantum Design PPMS and Oxford Instruments Maglab system (McMaster University) as well as a Quantum Design magnetic Property Measurement System (Brock University). Crystal samples of the transition metal complexes were dried, weighed, pelleted and tightly packed into plastic capsules.

2.1.7 Mössbauer Spectroscopy

Mössbauer spectroscopy were recorded with a constant-acceleration spectrometer (Wissel GMBH, Germany) in a horizontal transmission mode using a 50 mCi ^{57}Co source.

2.1.8 Electrochemistry

Cyclic voltammetry experiments were performed with an Epsilon Electrochemical Workstation. The samples were dissolved with the supporting electrolyte tetra(n-butyl)ammonium hexafluorophosphate in anhydrous solvent (DCM or DMF) and deaerated by

sparging with nitrogen gas for 15 minutes. Sample concentrations were approximately with 0.5 M in supporting electrolyte. A three-electrode set-up was used which includes a glassy carbon working electrode, an Ag wire reference electrode, and a platinum auxiliary electrode.

2.2.0 Single Crystal X-ray Structure Determination

2.2.1 Structure Elucidation of $[(Qsal)Fe(Qapl)]^{+}BPh_4^{-}$ (**12**)

A single crystal of complex **12** (0.27×0.17×0.07) mm^3 was diffracted using a Bruker APEX-II CCD diffractometer. The crystal was kept at T = 90(2) K during data collection. The structure was solved by Dr. Brian O. Patrick from the University of British Columbia, using Olex 2 with the XT structure solution program. The model was refined with version 2018/1 of XL using Least Squares minimisation. [85,86,87]

2.2.2 Structure Elucidation of $[(Cl\text{-}Qsal)Fe(Qapl)]^{+}BPh_4^{-}$ (**14**)

A single crystal of complex **14** was diffracted using a Bruker Nonius Kappa-CCD system with an Oxford Crysotream variable temperature apparatus, and the structure was solved by Dr. Alan J. Lough from the University of Toronto.

2.2.3 Structure Elucidation of $[Fe(Qan)_2]$ (**16**)

A single crystal of complex **16** (0.22×0.03×0.02) mm^3 was diffracted using a Bruker APEX-II CCD diffractometer. The crystal was kept at T = 100(2) K during data collection. The structure was solved by Dr. Brian O. Patrick from the University of British Columbia using Olex2 with the XT structure solution program. The model was refined with version 2018/1 of XL using Least Squares minimization. [85,86,87]

2.2.4 Structure Elucidation of $[(Qsal)Co(Qapl)]^{+}BPh_4^{-}$ (**18**)

A single crystal of complex **18** was diffracted using a Bruker Apex II Kappa, CCD X-ray diffractometer equipped with an Oxford Cryostream plus device, and the structure was solved by the Pilkington group of Brock University.

2.2.5 Structure Elucidation of $[(Qsal)Co(Papl)]^{+}BPh_4^{-}$ (**19**)

A single crystal of complex **19** was diffracted using a Bruker Apex II Kappa, CCD X-ray diffractometer equipped with an Oxford Cryostream plus device, and the structure was solved by the Pilkington group of Brock University.

2.2.6 Structure Elucidation of $[Fe(Qapl)_2]^{+}BPh_4^{-}$ (**20**)

A single crystal of complex **20** was diffracted using a Bruker Nonius Kappa-CCD system with an Oxford Crysotream variable temperature apparatus, and the structure was solved by Dr. Alan J. Lough from the University of Toronto.

2.3.0 Synthesis of Ligands

2.3.1 Synthesis of *N*-(8-quinolyl)salicylaldimine (Qsal) (**1**)

Prepared following the original condensation reaction from Dahl *et al*.[11]

To a 50 mL Erlenmeyer flask, 8-aminoquinoline (146.1 mg, 1.013 mmol) was added in 10 mL of methanol. To this solution, salicylaldehyde (107 μL, 1.03 mmol) was added and the solution turns dark yellow. The resulting mixture was stirred for 10 minutes at room temperature to produce *N*-(8-quinolyl)salicylaldimine. The ligand was left in solution and was not isolated or quantified. UV-vis (MeOH, nm): 336.

2.3.2 Synthesis of 5-chloro-*N*-(8-quinolyl)salicylaldimine (Cl-Qsal) (**2**)

Methodology follows closely to that of Sirirak *et al*.[57]

To a 50 mL Erlenmeyer flask, 5-chlorosalicylaldehyde (783.0 mg, 5.001 mmol) was added in isopropyl alcohol (20 mL). One equivalent of 8-aminoquinoline (721.0 mg, 5.001 mmol) was pre-dissolved in isopropyl alcohol (5 mL) and added to the solution of 5-chlorosalicylaldehyde. The mixture was left to stir at room temperature for 4 hours. The mixture was then covered in aluminum foil and left to stand overnight to allow for slow evaporation of most of the isopropyl alcohol. The resulting yellow precipitate was vacuum filtered, washed with isopropyl alcohol, and left in air to dry. Yield = 900.1 mg (64 %). ^{1}H-NMR (400 MHz, $CDCl_3$): δ 14.01 (s, 1H), 9.00 (s, 1H), 8.91 (s, 1H), 8.21 (dd, 1H), 7.76 (dd, 1H), 7.59 (t, 1H), 7.53-7.47 (m, 2H), 7.43 (d, 1H), 7.34 (dd, 1H), 7.04 (d, 1H). ^{13}C-NMR (400 MHz, $CDCl_3$): δ 163.46, 160.70, 150.63, 144.75, 142.23, 136.10, 133.09, 131.31, 129.24, 126.72, 126.56, 123.31, 121.85, 120.30, 119.25. LR-MS [$C_{16}H_{11}N_2OCl$] (ESI+): *m/z* 282.7. UV-vis (DCM, nm): 360. FT-IR (KBr, cm^{-1}): 3436 (w), 3042 (w), 2994 (md), 1624 (st).

2.3.3 Synthesis of 5-bromo-*N*-(8-quinolyl)salicylaldimine (Br-Qsal) (**3**)

Methodology follows closely to that of Sirirak et al.[57]

To a 50 mL Erlenmeyer flask, 5-bromosalicylaldehyde (506.0 mg, 2.517 mmol) was added in diethyl ether (20 mL). One equivalent of 8-aminoquinoline (363.0 mg, 2.518 mmol) was pre-dissolved in diethyl ether (5 mL) and added to the solution of 5-bromosalicylaldehyde. The mixture was left to stir at room temperature for 4 hours. The mixture was then covered in aluminum foil and left to stand overnight to allow for slow evaporation of some of the diethyl ether. The resulting orange precipitate was vacuum filtered, washed with diethyl ether, and left in air to dry. Yield = 660.1 mg (80%). ^{1}H-NMR (400 MHz, $CDCl_3$): δ 14.05 (s, 1H), 8.99 (dd,

1H), 8.91 (s, 1H), 8.21 (d, 1H), 7.76 (d, 1H), 7.59 (t, 2H), 7.53-7.46 (m, 3H), 6.99 (d, 1H). ^{13}C-NMR (400 MHz, $CDCl_3$): δ 163.34, 161.20, 150.65, 144.66, 142.28, 136.05, 135.82, 134.30, 129.21, 126.74, 126.55, 121.89, 120.94, 119.75, 119.23, 110.19. LR-MS [$C_{16}H_{11}N_2OBr$] (ESI+): *m/z* 327.2. UV-vis (DCM, nm): 350. FT-IR (KBr, cm^{-1}): 3369 (w), 3049 (w), 2968 (md), 1617 (st).

2.3.4 Synthesis of 10-(8-quinolylazo)-9-phenanthrol (Qapl) (**4**)

Methodology follows that of Taylor et al.[33]

In a 250 mL RBF, 8-hydroxyquinoline (10.01 g, 68.95 mmol) was mixed with hydrazine hydrate (80 mL) and stirred at reflux for 5 days. The reaction mixture was allowed to cool to room temperature to allow for crystallization of 8-hydrazinoquinoline. The yellow-brown crystalline product was vacuum filtered, washed with warm (50-70°C) dH_2O, and left in air to dry. Yield = 9.01 g (90 %). ^{1}H-NMR (400, MHz, $CDCl_3$): δ 8.74 (dd, 1H), 8.09 (dd, 1H), 7.47 (t, 1H), 7.41-7.38 (m, 1H), 7.28 (m, 1H), 7.17 (dd, 1H), 7.09 (d, 1H), 3.70 (s, 2H).

In a 500 mL RBF, 8-hydrazinoquinoline (9.00 g, 56.55 mmol) and 9,10-phenanthrenequinone (11.21 g, 53.84 mmol) were mixed in glacial acetic acid (35 mL) at 70°C overnight (12 hours). After stirring the solution was left to cool to room temperature and ice-dH_2O (200 mL) was poured into the solution with stirring until the ice completely melted. Small portions of Na_2CO_3 were added to neutralize the solution to pH 8 and resulted in a red precipitate. The red precipitate was vacuum filtered and left in air to dry. Yield = 17.10 g (91%). The crude red powder was pre-dissolved in a minimal amount of dichloromethane and 5 drops of glacial acetic acid before chromatographed over silica using dichloromethane as the eluent. The product was collected as a bright red band from the column and concentrated under reduced pressure as a bright red powder. Yield = 2.02 g (12%). ^{1}H-NMR (400 MHz, $CDCl_3$): δ 16.64 (s, 1H), 9.09

(dd, 1H), 8.62 (m, 2H), 8.31-8.19 (m, 4H), 7.63 (dd, 1H), 7.66-7.47 (m, 6H). ^{13}C-NMR (400 MHz, $CDCl_3$): δ 179.30, 149.66, 139.00, 135.90, 133.34, 131.20, 128.40, 127.47, 127.24, 127.05, 123.14, 123.04, 122.89, 121.99, 112.69. LR-MS [$C_{23}H_{15}N_3O$] (ESI+): *m/z* 349.1. UV-vis (DCM, nm): 507. FT-IR (KBr, cm^{-1}): 3065 (w), 2957 (w), 2955 (w), 2853 (w), 1620 (w), 1595 (md), 1573 (w), 1506 (st), 1479 (st), 1447 (md), 1414 (w), 1377 (w), 1364 (w), 1323 (w), 1281 (st), 1213 (st), 1128 (w), 1101 (w), 1080 (w), 1061 (w), 1047 (w), 1018 (w), 961 (w), 820 (w), 789 (md), 754 (md), 725 (md), 687 (w), 650 (w), 602 (w), 571 (w).

2.3.5 Synthesis of 1-(2-Pyridylazo)-2-phenanthrol (Papl) (**5**)

Methodology follows that of Taylor *et al*.[34]

In a 100 mL RBF, 2-hydrazinopyridine (301.0 mg, 2.76 mmol) and 9,10-phenanthrenequinone (589.0 mg, 2.83 mmol) were added in glacial acetic acid (30 mL). The reaction was heated to 120°C and allowed to reflux overnight. The solution was cooled to room temperature and poured over ice; the slurry was stirred until the ice was melted. Small portions of Na_2CO_3 (50 mg) were added and the product was precipitated. The product was isolated by vacuum filtration to yield an orange to brown solid. Yield = 521.1 mg (62 %). ^{1}H-NMR (400 MHz, $CDCl_3$): δ 8.41(m, 1H), 8.19 (d, 2H), 8.00 (d, 2H), 7.84 (m, 1H), 7.72 (m, 3H), 7.48 (t, 4H). UV-vis (DCM, nm): 466.

2.3.6 Synthesis of 1-(8-quinolylazo)-2-naphthol (Qan) (**6**)

Methodology follows that of Vershinina *et al*.[67]

In a 100 mL RBF, sodium nitrite $NaNO_2$ (1.09 g, 15.81 mmol) was added in dH_2O (10 mL). The $NaNO_2$ solution was slowly added to a cooled (0°C) solution of 8-aminoquinoline (2.00 g, 13.88 mmol) in HCl (10 mL, 18%). The mixture was left to stir in the ice bath for 30

minutes and the resulting diazonium salt solution was added to a solution of 2-naphthol (2.01 g, 13.91 mmol) in KOH (5.01 g, 89.31 mmol) and dH_20 (20 mL). The mixture was left to stir for 30 minutes and the neutralized with acetic acid to pH 8. The red precipitate was vacuum filtered and washed with dH_20. The red solid was left to dry in air at room temperature overnight and then subsequently dried in a flask at 90°C for 3 hours. Yield = 3.10 g (75 %). MS [$C_{19}H_{13}N_3O$] (ESI+): *m/z* 299.3. UV-vis (DCM, nm): 479.

2.3.7 Synthesis of 1-[2-(pyridinyl)hydrazono]-1-phenalenol (Phpl) (**7**)

Preparation of Phpl follows that of Dale *et al*.[35]

In a 250 mL RBF, cinnamoyl chloride (98%) (7.37 g, 44.24 mmol) and 2-methoxynaphthalene (7.01 g, 44.33 mmol) were mixed in equal equivalents in dry 1,2-dichloroethane (77 mL) under Schlenk conditions. The reaction was cooled in an ice bath to approximately 5^0C and an equivalent of $AlCl_3$ (5.90 g, 44.26 mmol) was added slowly with stirring. The reaction was allowed to warm to RT for 1 hour and a second portion (6.20 g, 46.50 mmol) of $AlCl_3$ was added. The reaction was refluxed for 3 hours and later quenched with iced HCl (35%) and filtered. The filtrate was extracted with DCM and refiltered until the solution became colourless. All the organic extracts were combined and dried with $NaSO_4$. The solution was filtered and concentrated under reduced pressure. The yellow solid was identified as 9-hydroxyphenalenone. Yield = 5.19 g (60 %). In a 100 mL RBF, 9- hydroxyphenalenone (861.1 mg, 4.39 mmol) was added in degassed $CHCl_3$ (25 mL) under nitrogen. An equivalent of Ag_2O (1.00 g, 4.32 mmol) was added with stirring at RT. An excess of iodomethane (60 µL) was added periodically every 3 hours over the course of one day. The reaction was left to stir at reflux overnight. The mixture was filtered and the filtrate was concentrated under reduced pressure to give 9-methoxy-1-phenalenone. The ligand powder is sensitive to air and moisture

and therefore, is typically used immediately in coordination reactions or stored under inert atmosphere. Yield = 0.80 g (86 %). ^{1}H-NMR (400 MHz, $CDCl_3$): δ 8.19 (d, 1H), 7.96 (d, 1H), 7.79 (d, 1H) 7.70 (d, 1H), 7.49 (t, 2H), 6.77 (d, 1H), 4.19 (s, 3H). ^{13}C-NMR (400 MHz, $CDCl_3$): δ 184.79, 163. 59, 139.15, 137.61, 131.79, 131.59, 130.85, 129.06, 127.16, 126.68, 124.05, 115.63, 113.95, 56.75.

In a 50 mL RBF, 9-methoxy-1-phenalenone (0.20 g, 0.957 mmol) and 2-hydrazinopyridine (0.1022 g, 0.9365 mmol) were mixed together in degassed $CHCl_3$ (20 mL) under nitrogen. The reaction was refluxed for 24 hours and the product was concentrated under reduced pressure. Yield = 0.20 g (78 %). ^{1}H-NMR (400 MHz, $CDCl_3$): δ 13.01 (s, 1H), 8.22 (d, 1H), 7.98 (d, 1H), 7.97-7.88 (m, 3H), 7.68 (d, 1H), 7.55-7.48 (m, 2H), 7.04 (d, 1H), 6.82 (dd, 1H), 6.78 (d, 1H). ^{13}C-NMR (400 MHz, $CDCl_3$): δ 183.3, 159.1, 156.7, 148.1, 138.7, 138.6, 138.5, 131.9, 131.5, 128.0, 125.7, 125.6, 122.7, 116.4, 114.2, 108.2, 106.5 ppm. HR-MS [$C_{18}H_{13}N_3$] (ESI+): *m/z* 288.1. FT-IR (KBr, cm^{-1}): 3188 (w), 3155 (w), 3030 (w), 1633 (st), 1593 (md), 1438 (md), 1269 (st).

2.3.8 Synthesis of 2,4-di-tert-butyl-6-(pyridin-2-ylazo)phenol (HL) (**8**)

Prepared according to Chatterjee *et al*.[65]

To a 100 mL RBF, 2-hydrazinopyridine (49.8 mg, 0.46 mmol) and 3,5-di-tert-butyl-o-benzoquinone (107 mg, 0.49 mmol) were added with glacial acetic acid (30 mL). The solution allowed to reflux for 5 days and cooled to room temperature. When cool, the mixture was poured over ice and mixed until the ice was melted. Na_2CO_3 (50 mg) was added in small portions to neutralize the solution and precipitate the product. The product must be immediately filtered to maintain a solid product. Prolonged contact in solution or in the Buchner funnel will cause the ligand to turn into a black tar-like semi-solid. Yield = 0.78 g (56%). ^{1}H-NMR (400 MHz,

$CDCl_3$): δ 8.73 (dd, 1H), 7.92 (m, 1H), 7.90 (m, 2H,), 7.51 (d, 1H), 7.40 (m, 1H), 1.49 (s, 9H), 1.39 (s, 9H). UV-vis (THF, nm): 422.

2.4.0 Synthesis of Coordination Complexes

2.4.1 Synthesis of [(Qsal)$FeCl_2(CH_3OH)$] (**9**)

To a 50 mL Erlenmeyer flask, 8-aminoquinoline (146.1 mg, 1.01 mmol) was added in 10 mL of methanol. To this solution, salicylaldehyde (107 μL, 1.02 mmol) was added. The resulting mixture was stirred for 10 minutes at room temperature to produce *N*-(8-quinolyl)salicylaldimine. To another 50 mL Erlenmeyer flask, $FeCl_3$ (165.1 mg, 1.02 mmol) was added in methanol (7 mL). Once stirring was complete, the flask containing *N*-(8-quinolyl)salicylaldimine was added drop-wise using a pipette to the flask containing $FeCl_3$. The resulting mixture was swirled, covered in aluminum foil, and left to stand for 4 hours to produce dark blue crystals. The blue crystals were filtered under vacuum and dried in air. Yield = 312.0 mg (74 %). Anal. Calc'd for $FeC_{17}H_{15}N_2O_2Cl_2$ (found, %): C, 51.38 (51.33); H, 2.96 (3.00); N, 7.49 (7.56). UV-vis (THF, nm): 429.

2.4.2 Synthesis of [(Cl-Qsal)$FeCl_2(CH_3OH)$] (**10**)

In a 50 mL Erlenmeyer flask, Cl-Qsal (101.1 mg, 0.358 mmol) was added in methanol (10 mL) at RT. In another 50 mL Erlenmeyer flask, $FeCl_3$ (56.9 mg, 0.351 mmol) was dissolved in methanol (7 mL). The dissolved Cl-Qsal ligand was slowly added drop-wise from a pipette to the flask containing $FeCl_3$ and swirled. The mixture was left to stand for 4 hours at RT upon which dark brown microcrystalline precipitated and were collected by vacuum filtration. Yield = 95.1 mg (66 %). Anal. Calc. for $FeC_{17}H_{14}N_2O_2Cl_3$ (found, %): C, 47.05 (47.25); H, 2.47 (2.41);

N, 6.86 (7.02). UV-vis (THF, nm): 333, 422, 456. FT-IR (KBr, cm^{-1}): 1602 (st), 1508 (st), 1450 (md), 1379 (md), 1313 (md), 1205 (md).

2.4.3 Synthesis of [(Br-Qsal)$FeCl_2(CH_3OH)$] (**11**)

In a 50 mL Erlenmeyer flask, Br-Qsal (97.2 mg, 0.30 mmol) was added in methanol (10 mL) at RT. In another 50 mL Erlenmeyer flask, $FeCl_3$ (48.0 mg, 0.30 mmol) was dissolved in methanol (7 mL). The dissolved Br-Qsal ligand was slowly added drop-wise from a pipette to the flask containing $FeCl_3$ and swirled. The mixture was left to stand for 4 hours at RT upon which dark brown microcrystalline precipitated and were collected by vacuum filtration. Yield = 87.1 mg (64 %). *Anal*. Calc. for $FeC_{17}H_{14}N_2O_2Cl_2Br$ (found, %): C, 42.42 (42.71); H, 2.23 (2.29); N, 6.18 (6.33). UV-vis (THF, nm): 336, 420. FT-IR (KBr, cm^{-1}): 1601 (st), 1521 (st), 1448 (st), 1377 (st), 1313 (md), 1205 (md).

2.4.4 Synthesis of [(Qsal)Fe(Qapl)]$^+BPh_4^-$ ·0.7THF (**12**)

In a 50 mL Erlenmeyer flask, Qapl (40.1 mg, 0.12 mmol) was stirred at room temperature with triethylamine (79 μL) in methanol (15 mL) for 10 minutes. One equivalent of [(Qsal)$FeCl_2(CH_3OH)$] (46.2 mg, 0.11 mmol) was added to the flask and the mixture was stirred for 5 days at RT. The solution turned maroon in colour and a dark orange precipitate formed. The reaction was vacuum filtered and the filtrate was collected. An excess of sodium tetraphenylborate (110.5 mg, 0.34 mmol) was dissolved in a minimal amount of methanol (>7 mL) with mild heating and allowed to cool to room temperature before added to the filtrate. The charged complex forms as a dark brown precipitate and was collected by vacuum filtration. Yield = 27.7 mg (38 %). LR-MS [$FeC_{39}H_{25}N_5O_2$] (ESI+): *m/z* 651.1; (ESI-): *m/z* 319.1. Anal. Calc'd for $FeC_{63}H_{45}N_5O_2$ ·0.7 THF (found, %): C, 77.39 (76.91); H, 4.99 (4.75); N, 6.86 (7.35).

UV-vis (THF, nm): 398, 558. FT-IR (KBr, cm^{-1}): 3440 (w), 3053 (w), 1604 (st), 1533 (st), 1504 (st), 1460 (md), 1427 (md), 1300 (md), 1232 (md), 1147 (md). Single rod-shaped crystals were grow by diffusion of tetrahydrofuran:pentane of approximately 6-7 mg in 4 mL of THF.

2.4.5 Synthesis of $[(Qsal)Fe(Qapl)]^{+}SCN^{-}$ (**13**)

The preparation of the cationic $[(Qsal)Fe(Qapl)]^{+}$ complex is analogous to 2.2.4.

Once the filtrate containing the cationic complex was collected an excess of potassium thiocyanate (100.2 mg, 1.03 mmol) was added to a minimal amount of methanol (>10 mL) with mild heating and allowed to cool to room temperature before it was added to the filtrate. The heteroleptic complex forms as a dark brown precipitate and was collected by vacuum filtration. Yield = 26.8 mg (61 %). LR-MS $[FeC_{39}H_{25}N_5O_2]$ (ESI+): *m/z* 651.1; (ESI-): *m/z* 58.1. Anal. Calc. for $FeC_{40}H_{25}N_6O_2 \cdot 0.95\ MeOH \cdot 1.55\ H_2O$ (found, %): C, 64.13 (64.14); H, 4.06 (4.02); N, 10.96 (10.92). UV-vis (THF, nm): 371. FT-IR (KBr, cm^{-1}): 2357 (md), 2048 (md), 1604 (st), 1502 (st), 1301 (st), 1226 (st).

2.4.6 Synthesis of $[(Cl\text{-}Qsal)Fe(Qapl)]^{+}BPh_4^{-}$ THF (**14**)

In a 50 mL Erlenmeyer flask, Qapl (24.1 mg, 0.069 mmol) was stirred at room temperature with triethylamine (48 μL) in methanol (15 mL) for 10 minutes. One equivalent of $[(Cl\text{-}Qsal)FeCl_2(CH_3OH)]$ (28.3 mg, 0.070 mmol) was added to the flask and the mixture was stirred for 4 days at room temperature. After 4 days the solution turned maroon in colour and a dark orange/brown precipitate formed. The reaction was vacuum filtered and the filtrate was collected. An excess of sodium tetraphenylborate (111.2 mg, 0.348 mmol) was added in a minimal amount of methanol (>10 mL) with mild heating and allowed to cool to room temperature before added to the filtrate. The charged complex forms as a dark brown precipitate

and was collected by vacuum filtration and left to dry in air. Yield = 32.2 mg (62 %). Anal. Calc. for $FeC_{63}H_{44}N_5O_2Cl \cdot 1.1\ MeOH \cdot 0.05\ THF$ (found, %): C, 74.04 (74.15); H, 4.62 (4.73); N, 6.71 (6.83). LR-MS [$FeC_{39}H_{24}N_5O_2Cl$] (ESI+): *m/z* 685.9 found 685.1. UV-vis (THF, nm): 332, 430, 573. Single crystals were grow by diffusion of tetrahydrofuran:pentane of approximately 6-7 mg in 4 mL of THF.

2.4.7 Synthesis of $[(Qsal)Fe(Phpl)]^+Cl^- \cdot 1$ MeOH (**15**)

In a 50 mL Erlenmeyer flask, Phpl (45.2 mg, 0.158 mmol) was added in methanol (15 mL) with excess triethylamine (108 μL) and stirred at RT. After 1-2 minutes of stirring, the $[(Qsal)FeCl_2(CH_3OH)]$ complex (63.1 mg, 0.155 mmol) was added to the solution. The reaction was left to stir at RT for 45 minutes. The resulting red-brown powder was vacuum filtered. Yield = 47.6 mg (52 %). LR-MS (ESI+): *m/z* 588.1. Anal. Calc'd for $FeC_{34}H_{22}N_5O_2Cl \cdot MeOH$ (found, %): C, 64.09 (63.75); H, 4.00 (3.77); N, 10.68 (10.35).

2.4.8 Synthesis of $[Fe(Qan)_2]$ (**16**)

In a 50 mL Erlenmeyer flask, Qan (37.2 mg, 0.122 mmol) was added in methanol (15 mL) with mild heating (40^0C) and stirring. Half of an equivalent of $FeCl_3$ (11.9 mg, 0.073 mmol) was added to the solution and the solution was allowed to cool to RT with stirring for 2 days. The resulting brown precipitate was collected by vacuum filtration. Yield = 33.9 mg (82 %). LR-MS [$FeC_{38}H_{24}N_6O_2$] (ESI+): *m/z* 652.2. UV-vis (THF, nm): 468. FT-IR (KBr, cm^{-1}): 3334 (w), 3039 (w), 1600 (st), 1504 (st), 1342 (st), 1288 (md), 1207 (md), 1147 (md). $\mu_{eff} = 0$ BM (298 K). Black rod-like crystals of the complex were obtained after 2 weeks through a dichloromethane:ether diffusion with 8 mg of the complex powder dissolved in DCM.

2.4.9 Synthesis of [(Qsal)Co(OAc)] ·1.15 CH_3CH_2OH ·2 H_2O (**17**)

Methodology follows that of Watts.[90]

In a 100 mL Schlenk flask, ethanol (35 mL) was added and purged with N_2 for 10 min. After purging, $Co(OAc)_2$•$4H_2O$ (501.1 mg, 2.83 mmol) was added and left to dissolve in purged EtOH. Qsal was formed as mentioned above under Schlenk conditions. Qsal was drawn from a 50 mL Erlenmeyer flask with a syringe and was slowly added to the $Co(OAc)_2$•$4H_2O$ solution. A red- orange precipitate was formed overnight which was collected by vacuum filtration. The product is an orange solid. An additional purification step was performed if the product was red. The product was filtered and washed with boiling ethanol to remove homoleptic Co-Qsal impurities. Yield = 190.1 mg (62%). Anal. Calc. for $CoC_{18}H_{14}N_2O_3$ ·1.15 CH_3CH_2OH ·2 H_2O (found, %): C, 53.67 (52.01); H, 5.52 (3.86); N, 6.17 (5.85). LR-MS [$CoC_{16}H_{11}N_2O$] (ESI+): *m/z* 306.1 found 306.0. UV-vis (MeOH, nm): 333, 437. FT-IR (KBr, cm^{-1}): 1608 (st), 1577 (st), 1558(st), 1435 (st), 1159 (md), 758 (md), 671 (md). μ_{eff}. = 3.98 BM (298 K).

2.4.10 Synthesis of [(Qsal)Co(Qapl)]$^+BPh_4^-$ (**18**)

Methodology follows that of Watts.[90]

In a 50 mL Erlenmeyer flask, the [(Qsal)Co(OAc)] complex (12.9 mg, 0.042 mmol) was added to methanol (10 mL). The Qapl ligand (11.2 mg, 0.032 mmol) was added in CH_2Cl_2 (2 mL) and slowly added to the [(Qsal)Co(OAc)] solution. The solution was mixed for 30 min. The complex was precipitated with the addition of $Na^+BPh_4^-$ (35.2 mg, 0.11 mmol). The complex was collected by vacuum filtration, to yield a dark purple to black solid. Yield = 15.1 mg (53%). Anal. Calc. for $CoC_{63}H_{45}N_5O_2$ ·0.75 $Na^+CH_3COO^-$ ·1 CH_3OH (found, %): C, 74.46 (74.53); H, 4.89 (4.75); N, 6.63 (6.73). LR-MS [$CoC_{39}H_{25}N_5O_2$] (ESI+): *m/z* 654.5 found 654.1. UV-vis

(THF, nm): 338, 353, 373, 446, 557, 597. FT-IR (KBr, cm^{-1}): 1606 (st), 1350 (st), 1313 (st), 1244 (st), 756 (md), 731 (md), 704 (st).

2.4.11 Synthesis of $[(Qsal)Co(Papl)]^{+}BPh_4^{-}$ $CHCl_3$ (**19**)

Methodology follows that of Watts.[90]

In a 50 mL Erlenmeyer flask, the [(Qsal)Co(OAc)] complex (49.0 mg, 0.16 mmol) was added in methanol (20 mL). The Papl ligand (31.3 mg, 0.11 mmol) was added to the [(Qsal)Co(OAc)] solution and mixed for 30 min. The solution turned black upon addition of Papl. The complex was precipitated with the addition of $Na^{+}BPh_4^{-}$ (11.7 mg, 0.37 mmol) to yield a dark purple to black solid. Yield = 27.3 mg (28 %). Anal. Calc. for $CoC_{59}H_{43}N_5O_2 \cdot 1.65$ $Na^{+}CH_3COO^{-} \cdot 1$ MeOH (found, %): C 70.37 (69.96); H, 4.85 (4.41); N, 6.48 (7.02). LR-MS $[CoC_{35}H_{23}N_5O_2]$ (ESI+): *m/z* 605.5 found 604.1. UV-vis ($CHCl_3$, nm): 338, 474, 574, 617. FT-IR (KBr, cm^{-1}): 1604 (st), 1506 (st), 1427 (md), 1365 (st), 1226 (st), 1149 (md), 931 (md), 756 (md), 704 (md).

Chapter 3.0 Heteroleptic Transition Metal Complexes

To this date there have been few reported heteroleptic $Fe^{3+/2+}$ complexes, with a few from this category that act as SCO or multifunctional materials.[25,47,50] Research endeavours from Harding and Murray with co-workers highlight the SCO behaviour of quinolylsalicylaldiminate complexes in the form of $[Mn(Cl\text{-}Qsal)_2]^{0/+}$, $[Mn(Br\text{-}Qsal)_2]^{0/+}$and $[Fe(Qsal\text{-}5\text{-}OMe)_2]^{+}X^{-}$ where the anionic tuning of X^{-} to either PF_6^{-} or NCS^{-} resulted in a gradual and abrupt SCO, respectively. Like Harding, Murray and co-workers, Takahashi and colleagues have reported charged anionic Fe^{3+} SCO complexes with weak field N_2O_4 coordination spheres. Examples like these among others are compared with the results obtained from meeting the synthetic objectives of designing d^4-d^7 transition metal heteroleptic complexes. Working out the synthetic strategies toward coordination complexes with Qsal and some arylazo redox-active ligand like Qapl, Papl, or Phpl has led to several charged complexes with either a Fe^{3+} or $Co^{3+/2+}$ center. Most of the arylazo redox-active ligands behaved differently during each coordination reaction, with the more notable dissimilarity being between Qapl and Papl with $[(Qsal)FeCl_2(CH_3OH)]$. This is mainly thought to be due to Papl tautomerizing in solution producing various by-products despite its use for synthesizing a heteroleptic mononuclear cobalt complex. Generally, each coordination reaction and its respective synthetic target presented many challenges including dissociation from homoleptic complexes, solubility differences, and propensity toward different counter ions.

3.1.0 Series of $[(Qsal)FeCl_2(CH_3OH)]$ Complexes

Naturally, the synthetic approach began with reacting protonated versions of Qsal and some corresponding RAL with an equivalent ratio of $FeCl_3$ as the source of Fe^{3+} in a polar protic solvent such as methanol or ethanol, common in literature.[5,7,25] Initially these reactions were

carried out at room temperature and exposed to air. The outcome of the early coordination reactions resulted in either complete formation of homoleptic $[Fe(Qsal)_2]^+Cl^-$ and $[Fe(RAL)_2]^+Cl^-$ complexes or a mixture of homoleptic complexes and starting ligands.

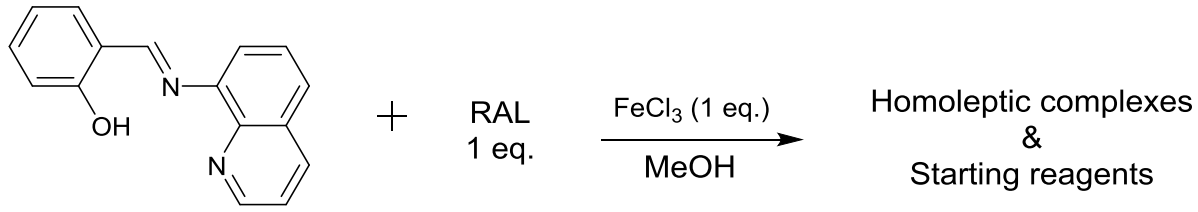

1

Scheme 3.0: Initial reaction path toward heteroleptic Fe^{3+} complexes.

These results lead to investigating each variable of the coordination reaction which involved regulating temperature, concentration, solvent, inert atmosphere conditions, and time. Increasing the temperature above room temperature or to reflux led to the complete formation of the homoleptic complexes. Decreasing the temperature to 0°C, and in some instances below zero, delayed the formation of homoleptic complexes which left an abundance of unreacted starting materials. Manipulating other variables such as increasing or decreasing the concentration of ligands to metal ratio, using different polar solvents, or conducting the reactions under Schlenk conditions produced the similar results. Shortening or lengthening the reaction time while monitoring each individual variable did not seem to affect these outcomes. It had become evident that any formation of heteroleptic species was not obvious and seemed unfavourable, based on the reactants. This led to exploring some other methods of introducing the metal ion while simultaneously inhibiting the formation of the homoleptic species. From the Lemaire lab group, a previously synthesized $[(Qsal)FeCl_2(CH_3OH)]$ complex featuring two ancillary Cl^- ligands was proposed to be better suited toward forming the heteroleptic Qsal-RAL complexes

since Fe^{3+} was already coordinated to the desired Qsal ligand with Qsal's N_2O chelating effect providing greater stability versus the Cl^- donors on $FeCl_3$.

The $[(Qsal)FeCl_2(CH_3OH)]$ complex is synthesized in two subsequent steps. The first step is a condensation reaction between one equivalent of 8-aminoquinoline and salicylaldehyde in methanol to synthesize the Qsal ligand in a similar manner to that of Dickinson and Baker and Dahl *et al.*[10,11] The second step is adding drop-wise the solution of Qsal to a pre-dissolved solution of $FeCl_3$ of equivalent ratio in methanol. The Qsal and $FeCl_3$ mixture is left to sit at room temperature exposed to air for approximately 4 hours where after the complex crystallized out of solution as large dark blue crystals.

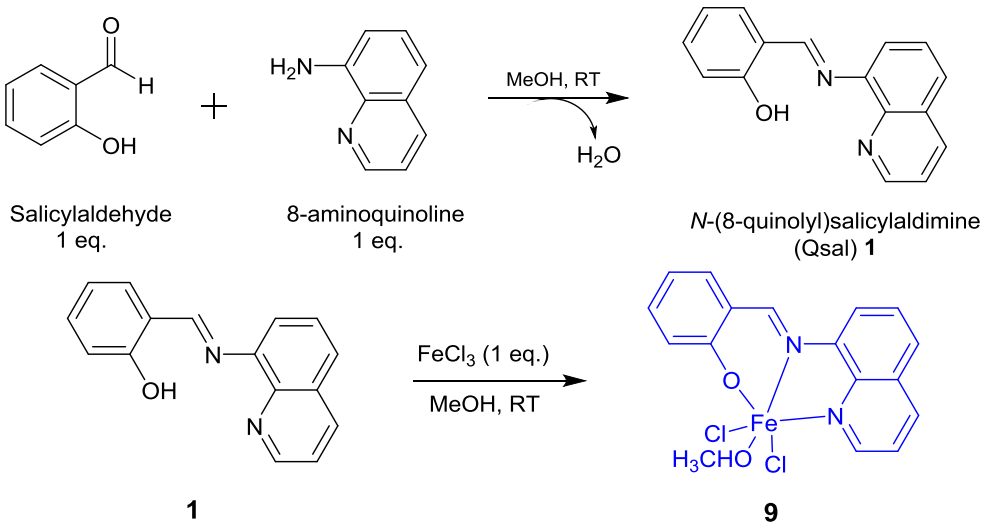

Scheme 3.1: Synthesis of $[(Qsal)FeCl_2(CH_3OH)]$.

A crystal structure of complex **9** reveals a single coordinated MeOH molecule with two Cl^- and one Qsal ligand. Some analytical techniques such as MS were found unsuitable for identifying the formation of complex **9** due to a rearrangement as a result of the ionization process, consequently only identifying the 550 *m/z* signal which corresponds to the homoleptic $[Fe(Qsal)_2]^+$ complex. The UV-visible spectra presented in Figure 3.0 below contrasts the differences between complex **9** and homoleptic $[Fe(Qsal)_2]^+Cl^-$.

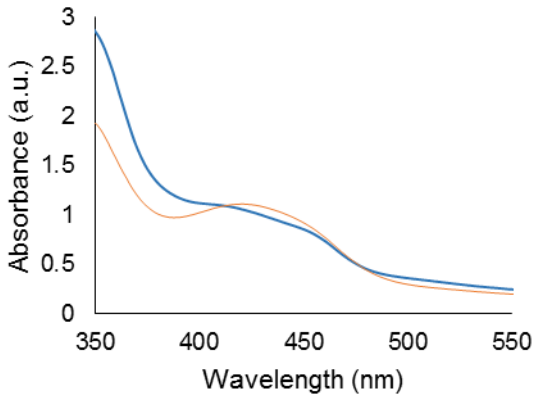

Figure 3.0: UV-visible spectra comparing complex **9** (blue) to homoleptic $[Fe(Qsal)_2]^+Cl^-$ (orange) in DCM at RT.

The absorbance pattern for both complex **9** and homoleptic $[Fe(Qsal)_2]^+Cl^-$ are quite similar as anticipated with a slight shift in absorbance at 380 nm and varying intensity at 430 nm.

Halogenated versions of $[(X\text{-}Qsal)FeCl_2(CH_3OH)]$ were also prepared in an analogous manner to complex **9** using Cl-Qsal and Br-Qsal. Cl-Qsal and Br-Qsal were synthesized by a condensation reaction between 8-aminoquinoline and 5-chlorosalicylaldehyde and 5-bromosalicylaldehyde, respectively.

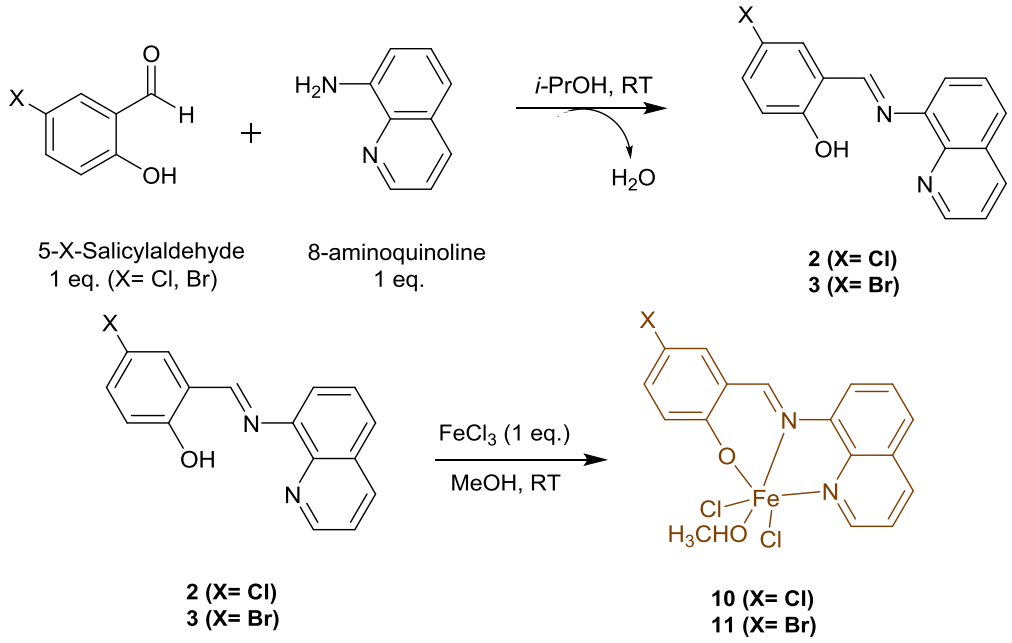

Scheme 3.2: Halogenated versions of complex **9**.

Explicit formation of complex **10** and **11** have not yet been ascertained by X-ray diffraction as conditions for growing diffractable crystals have not yet been determined. As with complex **9**, both complex **10** and **11** have the same rearranging effect during the ionization process of MS ESI. However, the elemental analysis for both complexes **10** and **11** are in agreement with theoretical values each within 99-97% identical. The formation of complexes **9**, **10**, and **11** have also been inferred from their use in synthesizing heteroleptic $[(Qsal)Fe(Qapl)]^{+}X^{-}$ and $[(X\text{-}Qsal)Fe(Qapl)]^{+}X^{-}$ complexes. These halogenated versions of Qsal were expected to contribute additional halogen bonding patterns to the repertoire of intermolecular O-H···O, C-H···N/O, C-H···π, and π-π interactions.[57] These additional interactions were understood to induce tighter packing and enhanced cooperativity as illustrated in Figure 3.1 below.

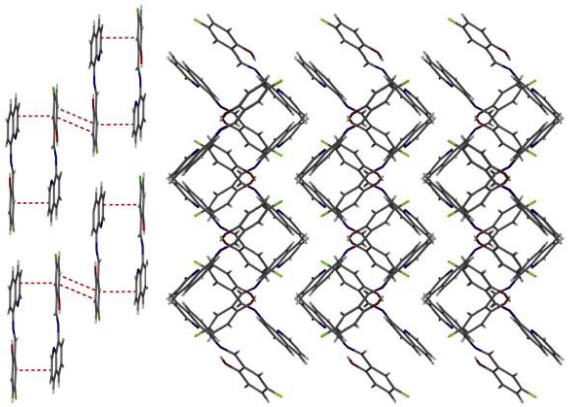

Figure 3.1: Intermolecular π-π interactions of Qsal dimers (left); Packing of Qsal dimer structure (right). Taken from *J. of Mol. Struct.*, **2013**, 1036, 439-446.

Efforts to synthesize other Fe^{3+} complexes with some redox-active arylazo ligands that feature the same N_2O donor pattern as Qsal in the form of $[(RAL)FeCl_2(CH_3OH)]$ were unsuccessful. Arylazo ligands like 10-(8-quinolylazo)-9-phenanthrol (Qapl), 1-(8-quinolylazo)-2-naphthol (Qan), and 2,4-di-tert-butyl-6-(pyridin-2-ylazo)phenol (HL) were used in attempts to generate $[(Qapl)FeCl_2(CH_3OH)]$, $[(Qan)FeCl_2(CH_3OH)]$, and $[(HL)FeCl_2(CH_3OH)]$ respectively, but only

resulted in homoleptic formations or unreacted materials. During these trials other sources of iron were explored such as $Fe(AcAc)_3$ but did not seem to benefit or provide control over the formation of any mixed ligand complexes.

3.2.0 Heteroleptic $[(Qsal)Fe(Qapl)]^+BPh_4^-$ Complex

The phenanthrol-based arylazo quinoline substituted ligand 10-(8-quinolylazo)-9-phenanthrol (Qapl) is prepared in two steps.[33] The first step involves the reflux of 8-hydroxyquinoline in an excess solution of hydrazine hydrate to yield 8-hydrazinoquinoline. The second step involves heating the 8-hydrazinoquinoline in glacial acetic acid with 9,10-phenanthrenequinone.[33] Column chromatography is required to purify Qapl, so it is obtained in a relatively low yield (12 %). Unlike the related Papl ligand which exists a keto-enol tautomer, NMR data (Appendix A.7) shows that Qapl exists as a single species in solution. The significantly deshielded O-H resonance appearing far above 15 ppm is suggestive of H-bonding with a nitrogen atom from the azo group.

The charged heteroleptic $[(Qsal)Fe(Qapl)]^+Cl^-$ complex was synthesized using monoanionic Qapl with complex **9**. Anionic tuning as seen with Harding and Murray's quinolylsalicylaldiminate complexes was used to expand the $[(Qsal)Fe(Qapl)]^+Cl^-$ complex into a series that feature different counter ions including BPh_4^-, SCN^-, PF_6^-, I^- and NO_3^-.[78] This provided a means of purifying the charged heteroleptic complexes in order to investigate their structural and magnetic properties.

3.2.1 Synthesis and Structural Characterization

The synthesis of $[(Qsal)Fe(Qapl)]^+BPh_4^-$ involved pre-dissolving the 10-(8-quinolylazo)-9-phenanthrol ligand in methanol with an excess of triethylamine followed by the addition of one

equivalent of the [(Qsal)$FeCl_2(CH_3OH)$] complex. The addition of excess triethylamine to deprotonate and generate the monoanionic form of the arylazo ligand was found to reduce the time needed for coordination as well as slightly increase the yield.

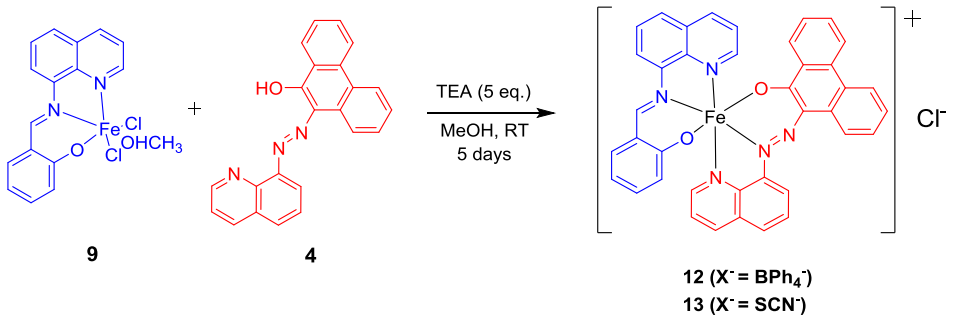

9 **4** **12 (X^- = BPh_4^-)** **13 (X^- = SCN^-)**

Scheme 3.3: Synthesis of [(Qsal)Fe(Qapl)]$^+Cl^-$

As with earlier attempts of generating heteroleptic complexes, heating the reaction resulted in the formation of the undesired homoleptic $[Fe(Qapl)_2]^+$ complex while cooling the reaction only led to longer reaction times which often resulted in both heteroleptic and homoleptic complexes with lower yields (>20%). The prime conditions for generating the [(Qsal)Fe(Qapl)]$^+Cl^-$ complex seemed to be allowing the mixture to stir for 5 days at room temperature in an open atmosphere. At the end of this time period the solution was filtered and isolated from any homoleptic formations and unreacted starting materials as the heteroleptic cationic $[(Qsal)Fe(Qapl)]^+$ complex with a Cl^- counter ion was the only species that remained soluble in MeOH (along with excess triethylamine). An exchange of the Cl^- ion for the bulkier BPh_4^- ion was used to precipitate the heteroleptic complex from solution. This resulted in a dark brown powder precipitating out of the filtrate solution which was then filtered and recrystallized from a THF and pentane diffusion. Single black tablet-shaped crystals of the [(Qsal)Fe(Qapl)]$^+BPh_4^-$ complex grew and a single crystal was diffracted at 90 K. Its structure is reported below in Figure 3.2.

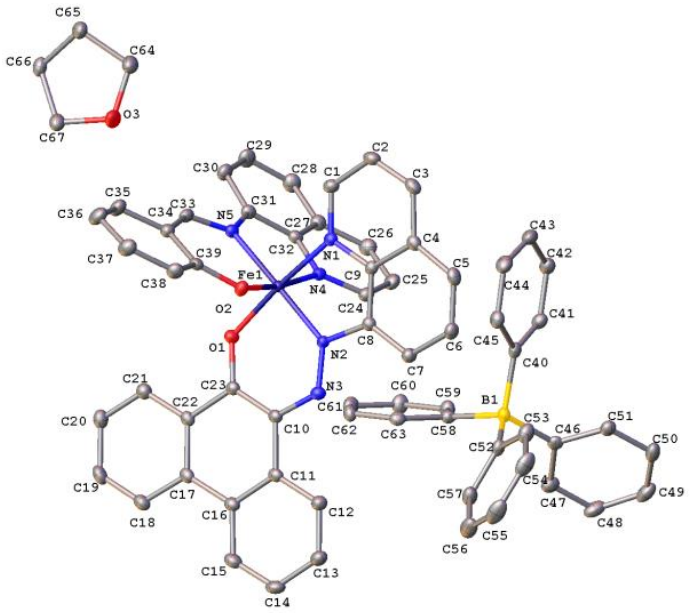

Figure 3.2: Molecular structure of $[(Qsal)Fe(Qapl)]^{+}BPh_4^{-}$ diffracted at 90 K. Hydrogens excluded for clarity. Structure solved by Dr. Brian O. Patrick from the University of British Columbia.

Table 3.0: Coordinate bond lengths and angles of $[(Qsal)Fe(Qapl)]^{+}BPh_4^{-}$

Bond	Length/ Å	Atoms	Angle/°
Fe1-O1	1.8875(11)	O1-Fe1-N1	175.10(5)
Fe1-O2	1.8811(11)	O1-Fe1-N2	91.21(5)
Fe1-N1	1.9695(13)	O1-Fe1-N4	93.47(5)
Fe1-N2	1.8879(13)	O1-Fe1-N5	86.73(5)
Fe1-N4	1.9908(13)	O2-Fe1-O1	93.32(5)
Fe1-N5	1.9536(14)	O2-Fe1-N1	87.19(5)
N2=N3	1.2910(18)	O2-Fe1-N2	88.60(5)
		O2-Fe1-N4	172.12(5)
		O2-Fe-N5	94.16(5)
		N1-Fe1-N4	86.39(5)
		N2-Fe1-N1	83.93(6)
		N2-Fe1-N4	95.25(6)
		N2-Fe1-N5	176.64(6)
		N5-Fe1-N1	98.10(6)
		N5-Fe1-N4	82.24(6)

The reported bond distances are typical of a Qsal anion, similar to lengths that have been reported in other Fe-Qsal complexes.[49] The azo bond of the Qapl ligand was measured to be 1.29 Å between N2=N3, typical of an azo double bond.[34,64,66] Comparable to literature at 100K, the short coordinate bond lengths (<2.0 Å) between the iron center and the N_2O donor atoms of

both the Qsal and Qapl ligands are evident of a LS iron.[5] Coordinate bond lengths for LS iron species are typically short under 2.0 Å as a result of the *d*-electrons solely occupying the t_2g orbitals forming strong coordinate bonds due to the overlap with ligand orbitals.[4,5] HS Fe^{3+} species are typically observed to have coordinate bond elongations of over 2.0-2.1 Å.[54] The overlap between neighbouring complexes occurs through C10, C11, C16-C23 of the phenanthrol rings of Qapl. This interaction closes as distance of 3.563 Å shown in Figure 3.3.

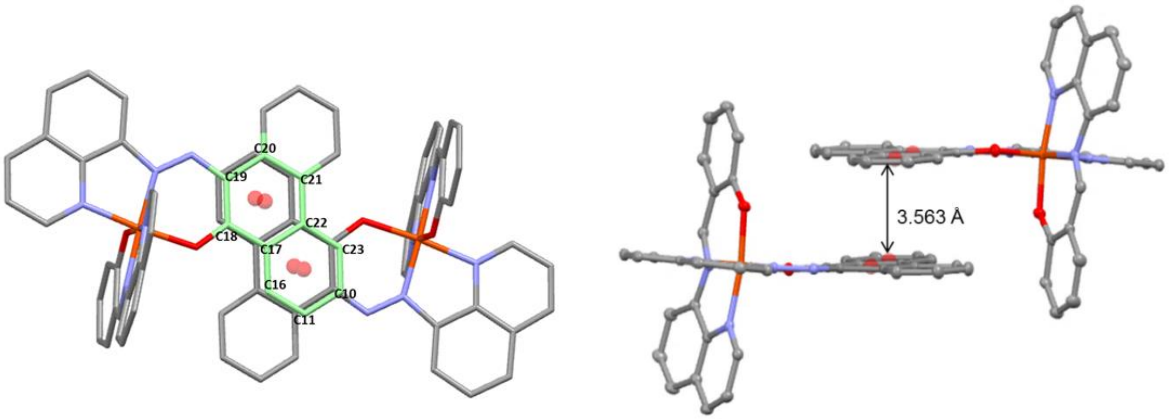

Figure 3.3: Intermolecular π-π overlap of $[(Qsal)Fe(Qapl)]^{+}BPh_4^{-}$. Hydrogen atoms, solvent molecules and counter ions omitted for clarity.

The directional π-stacking interactions observed in the heteroleptic azobisphenolate Fe^{3+} $[(Qsal)Fe(azp)]\cdot 0.5CH_3OH$ complex, with a N_3O_3 coordination sphere, contribute to cooperative SCO.[47] The interlocking chain structure of complex **12** shown in Figure 3.4 highlights the overlap between the phenanthrol rings of Qapl 3.56 Å apart at low temperature.

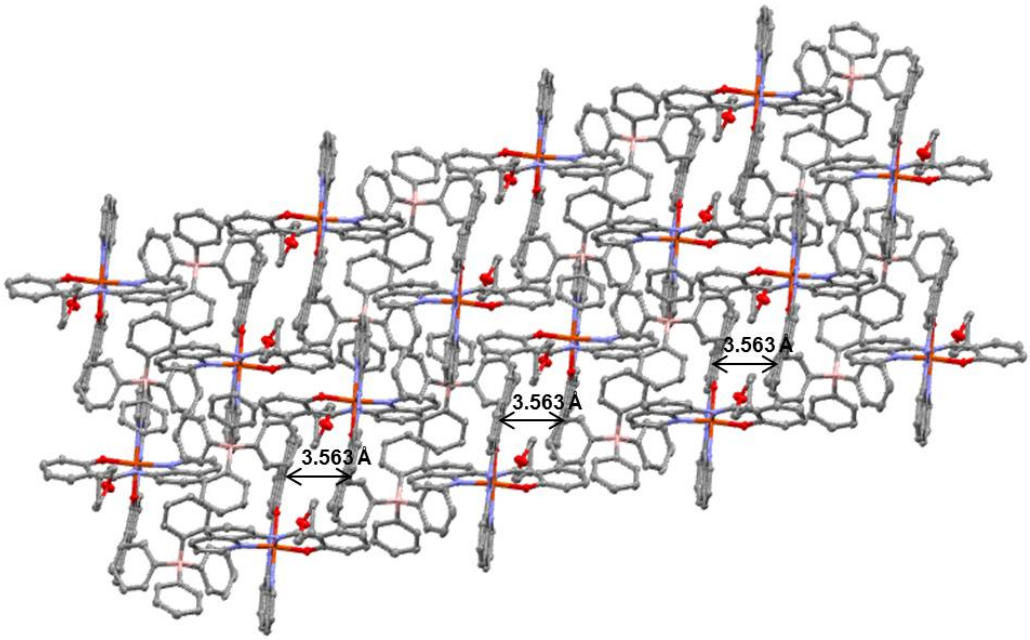

Figure 3.4: Packing structure of $[(Qsal)Fe(Qapl)]^{+}BPh_4^{-}$. Hydrogen atoms and solvent molecules omitted for clarity.

This overlap between the phenanthrol rings is the shortest and only π-π intermolecular interaction between the complexes. It is slightly longer than the thermal variations of the π-plane distances reported for the crystal structure of [(Qsal)Fe(azp)]·0.5 MeOH at 90 K and 273 K which barely fluctuate between 3.4 Å (+/- 0.1).[47,55] Other potential interactions among complex **12** appear to be inhibited by the presence of the BPh_4^{-} ion and its spatial arrangement relative to the Qsal ligands. Spectrometric data is provided below in Figure 3.5 and follows with the recurring pattern of rearrangement that is seen among most of the synthetic targets throughout this work.

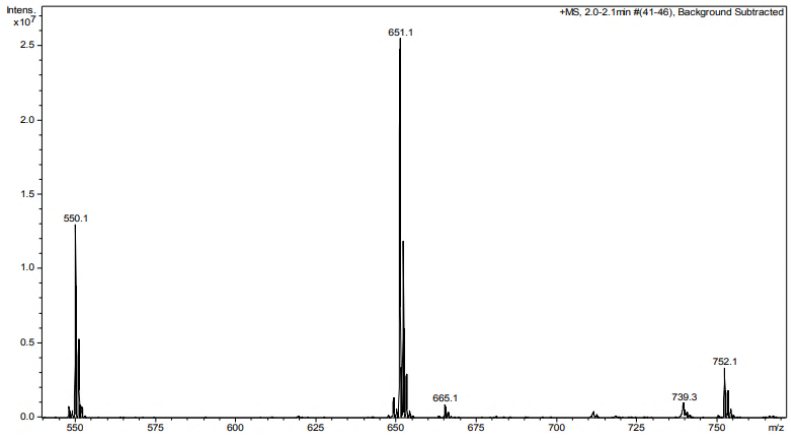

Figure 3.5: MS ESI+ of $[(Qsal)Fe(Qapl)]^{+}BPh_4^{-}$ complex. MS ESI- mode identified the 319.0 *m/z* corresponding to tetraphenylborate counter ion.

The 651.1 *m/z* corresponding to the heteroleptic $[(Qsal)Fe(Qapl)]^{+}$ complex is accompanied by two other signals: 550.1 *m/z* and 752.1 *m/z*. The 550.1 *m/z* and 752.1 *m/z* signals correspond to the formation of the homoleptic $[Fe(Qsal)_2]^{+}$ and $[Fe(Qapl)_2]^{+}$ species, respectively. These results were not surprising as they follow for ESI noted from complexes **9**, **10** and **11**.

3.2.2 Magnetic Properties

The magnetic switching behaviour of $[(Qsal)Fe(Qapl)]^{+}BPh_4^{-}$ was probed in the solid state and its molar susceptibility plot is shown below in Figure 3.6. Variable temperature magnetic susceptibility measurements were recorded using a Quantum Design SQUID magnetometer with a 5T magnet and a Quantum Design MPMS system.

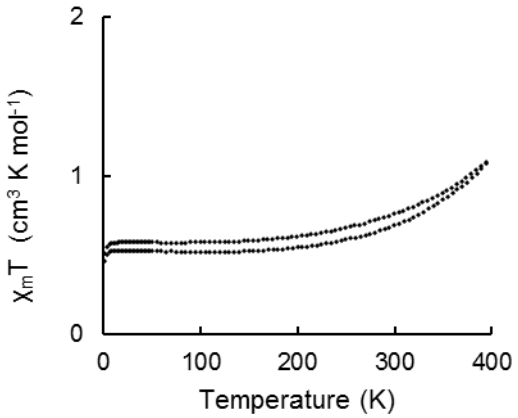

Figure 3.6: Molar susceptibility profile for $[(Qsal)Fe(Qapl)]^{+}BPh_4^{-}$ over a temperature range of 2 K to 395 K.

The profile for heteroleptic $[(Qsal)Fe(Qapl)]^{+}BPh_4^{-}$ is LS Fe^{3+} showing nearly no change up to 300 K. However, between the temperature range of 300-395 K there is a subtle increase in $\chi_M T$ which may be suggestive of some early onset of spin-crossover. The $\chi_M T$ value of 0.458 cm^3 K mol^{-1} at 2 K reaches 1.08 cm^3 K mol^{-1} as the temperature approach 395 K. The weak communication in the solid state is attributed to the lack of intermolecular contacts as a result of the BPh_4^{-} counter ion.[7,39,83] The intermolecular contacts between the phenathrol rings of the Qapl ligand are relatively long at 3.56 Å.[5,25] A similar trend of a gradual spin transition has been noted in literature between the temperature range of 250 K to 400 K with a heteroleptic bis-tridentate Fe^{3+} [Fe(3-OMe-Sal(En)(thsal)] complex, but exhibits complete SCO more abruptly beyond RT at 344 K.[51] The SCO process observed in this example has been attributed to the π-π interactions that seem to correlate with $T_{1/2}$, that is as the strength of π-π interactions increases then the higher $T_{1/2}$ becomes in complexes with abrupt SCO.[51] The effects of π-π interactions in relation to SCO were supported based on the comparison to the complex $[Fe(3\text{-}OMe\text{-}salEen)_2][Ni(dmit)_2]\cdot CH_3OH$ where π-π interactions are absent and the complex shows a gradual SCO over a temperature range of 200 K.[51] Therefore, these intermolecular π interactions allow the structure to pack in a higher degree of order which gives rise to a more abrupt transition.[51]

Based on these results, the $[(Qsal)Fe(Qapl)]^{+}BPh_4^{-}$ hold weaker π-π interactions and may require much higher temperatures to induce SCO.

The magnetic susceptibility was also measured in solution by the Evans method. The differences in the solvent's chemical shift caused by the paramagnetic character of $[(Qsal)Fe(Qapl)]^{+}BPh_4^{-}$ in $CDCl_3$ as a function of temperature showed some incomplete spin-crossover. Electronic spectroscopy was used to support that there is possible spin-crossover behaviour in solution. VT UV-vis is often used to probe for the switching states in solution as a function of temperature.[1,5,83] Both the VT UV-vis and VT Evans method data are presented below in Figure 3.7.

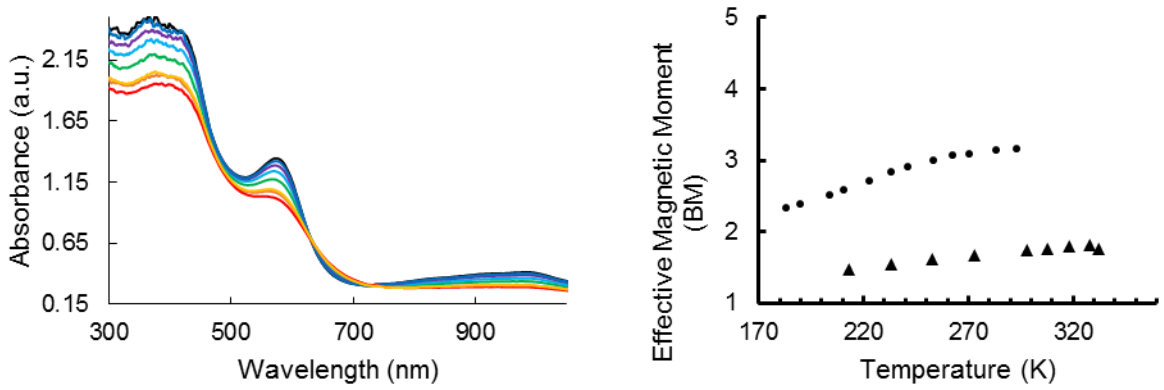

Figure 3.7: VT UV-vis spectra of $[(Qsal)Fe(Qapl)]^{+}BPh_4^{-}$ in THF. Temperature range from 183 K (blue) to 303 K (red). VT Evans method of $[(Qsal)Fe(Qapl)]^{+}BPh_4^{-}$ in $CDCl_3$; d_8-THF (triangles) between temperature range 213 K to 332 K.

An isosbestic point at 630 nm and 733 nm is noted indicating that there are two individual components in solution that share a constant absorption at that particular wavelength.[1,20] Some charge transfer bands are seen at shorter wavelengths and higher energies and can be most likely be inferred as LMCT bands as the metal present in the complex is a high oxidation Fe^{3+} ion.[7,20] From the magnetic susceptibility measurements by Evans method, a species with S= 1/2 is stable at low temperature. Despite not reaching an effective magnetic moment of >5.9 BM at RT,

which would correspond to a HS Fe^{3+} species with all 5 *d*-electrons unpaired, the data still shows some climbing trend with higher temperatures. Some transitioning as the temperature approaches 300 K with some species resembling *S*= 3/2 state is stable at near RT. Some explanations offered to rationalize this data could point toward a HS Fe^{2+} ion with *S*= 2 being antiferromagnetically coupled to a ligand radical with *S*= 1/2 to give rise to the *S* = 3/2 state observed at 300 K. Alternatively, this could simply be an example of some incomplete spin-crossover phenomena where both states are not completely populated. There are several examples of Fe^{3+} with an intermediate spin (*S*=3/2) seen in iron porphyrins and Fe^{3+} complexes with macrocyclic tetraamido-*N* ligands.[77] The $[Et_4N]_2[FeCl(\eta^4\text{-MAC*})]^{n-}$ complex in its ferric state has an electronic ground state with intermediate spin *S*=3/2. The coordinate bond distances measured from the crystal structure obtained at 293 K between the Fe center and N1, N2, N3, N4 donor atoms all lay within the 1.916-1.932 Å range. Admixed spin states of *S*=3/2 and *S*=5/2 multiplicities are not uncommon in iron heme- or porphyrin systems.[76,77] The solubility of the complex also poses an issue with Evans method as the complex may precipitate out of solution over time with fluctuating temperatures which will alter the concentration value. The behaviour of the complex in solution prompted further investigation of the unpaired electrons using EPR. The results of the EPR experiments are presented below in Figures 3.8 and 3.10.

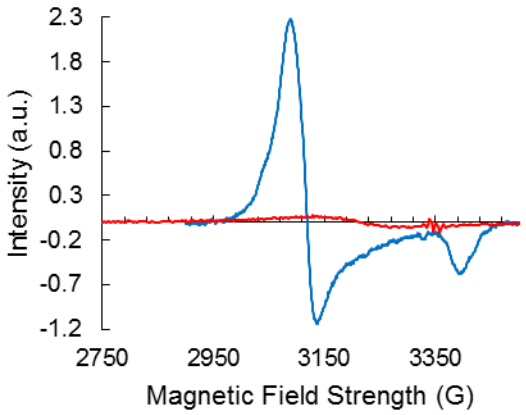

Figure 3.8: EPR spectrum of $[(Qsal)Fe(Qapl)]^{+}BPh_4^{-}$ in THF at 100 K (blue trace) overlapped with spectrum at RT (red trace).

The low temperature EPR spectrum here essentially presents the $[(Qsal)Fe(Qapl)]^{+}BPh_4^{-}$ complex in a frozen state. A RT spectrum produced from the same sample has a significant decrease in intensity and is shown overlapped with the low temperature spectrum in Figure 3.8. Typically the smaller the g-anisotropy, the higher the spectral intensity will be.[40] Here, the low temperature behaviour of complex **12** is observed as rhombic LS Fe^{3+} (S=1/2).[40,55] The rhombic spectrum with g_x, g_y, and g_z indicate inequivalent axes. An enlarged version of the 293 K spectrum of complex **12** is presented below in Figure 3.9.

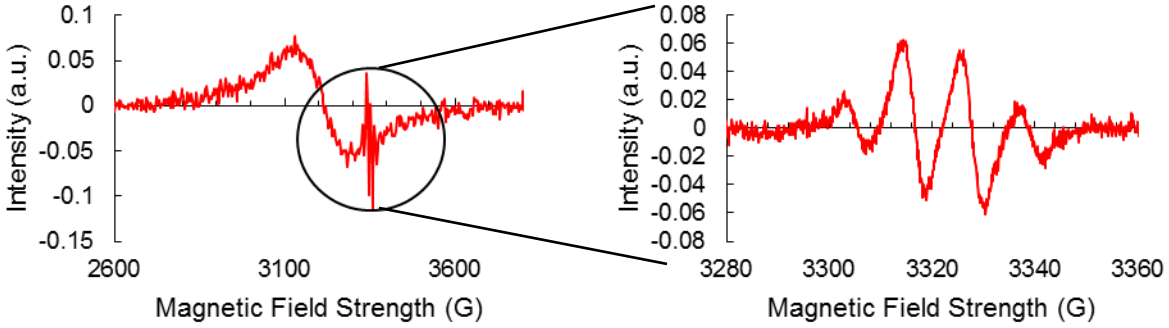

Figure 3.9: EPR spectra of $[(Qsal)Fe(Qapl)]^{+}BPh_4^{-}$ in THF at 293 K.

Close to RT the rhombic Fe^{3+} (S=1/2) spectrum disappears. This is noted by the scale of intensity in Figure 3.9, as well as the contrast in relative intensity seen from the overlap of

spectra presented in Figure 3.8. A signal that corresponds to HS Fe^{3+} (*S*= 5/2) typically appears with a broad resonance centered at g = 2.0 with the x and y tensor g-values close between 4.0-6.0.[77,80] However, with the disappearance of the Fe^{3+} *S*=1/2 spectrum and the lack of evidence for the presence of Fe^{3+} *S*=5/2, the disappearance of the signal may be masked by some impurity of the spin states or other connected to the unusual splitting seen in Figure 3.9.

3.2.3 Electrochemical Properties

The electrochemical properties of complex **12** are reported below in Figure 3.10. Cyclic voltammetry experiments were conducted at with a scan rate of 100 mVs.

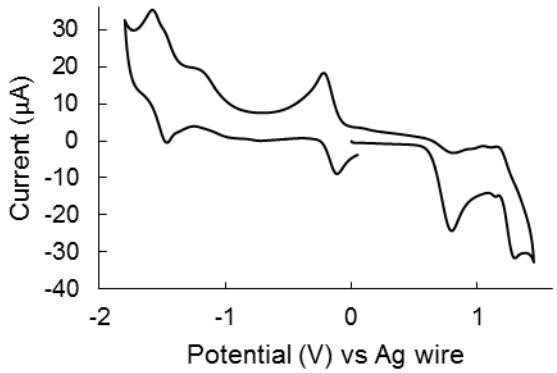

$E_{1/2}$ Anodic vs Ag wire	$E_{1/2}$ Cathodic vs Ag wire
0.8 V (irr), 1.3 V (irr)	-0.17 V (qr), -1.5 V (qr)

Figure 3.10: Voltammogram of $[(Qsal)Fe(Qapl)]^{+}BPh_4^{-}$ in DCM containing 0.5M $^{n}NBu_4PF_6$ supporting electrolyte.

The quasi-reversible $E_{1/2}$ value at -0.17 V corresponds to the reduction of Fe^{3+}.[75] Uncoordinated Qapl can be reduced quasi-reversibly from the reduction of the azo to form the radical anion of the ligand.[32,33,57] Previously shown, the Qapl ligand has a quasi-reversible cathodic wave centered at -1.1 V (vs Ag/AgCl) and only irreversible anodic processes at high positive potential.[33] Transition metal complexes with azo-aromatic ligands often feature some reversible

cathodic trace which is suggestive of stable ligand-centered reductions.[32] Therefore, the cathodic wave here can be assigned to the reduction of the azo N=N π-antibonding character. In comparison, a homoleptic $[Co(Qapl)_2]^+Cl^-$ exhibits two cathodic processes at potentials greater than -1.0 V (vs Ag/AgCl) that are assigned as ligand-centered reductions.[33] Reduction of the $[(Qsal)Fe(Qapl)]^+BPh_4^-$ complex, conducted in the glovebox using sodium, led to the decomposition of the complex possibly due to the strength of the reducing agent.

3.3.0 Heteroleptic $[(Qsal)Fe(Qapl)]^+SCN^-$ Complex

The formation and solubility of the $[(Qsal)Fe(Qapl)]^+Cl^-$ complex in methanol already necessitated that a counter ion exchange would precipitate the heteroleptic complex from solution. Therefore, SCN^-, PF_6^-, NO_3^-, and I^- were used and theorized to be spatially less cumbersome over any intermolecular interactions of the heteroleptic complex.

3.3.1 Synthesis and Structural Characterization

The synthesis to generate the $[(Qsal)Fe(Qapl)]^+Cl^-$ complex remained unchanged. Once the charged heteroleptic complex was formed and known to remain in solution, excess K^+SCN^- predissolved in methanol was added to the filtrate and a brown powder was precipitated. The powder was washed with warm dH_2O to remove any potassium salts (KCl) and solvent which were taken into consideration over the elemental analysis of the complex. The spectrometric data is reported below in Figure 3.11.

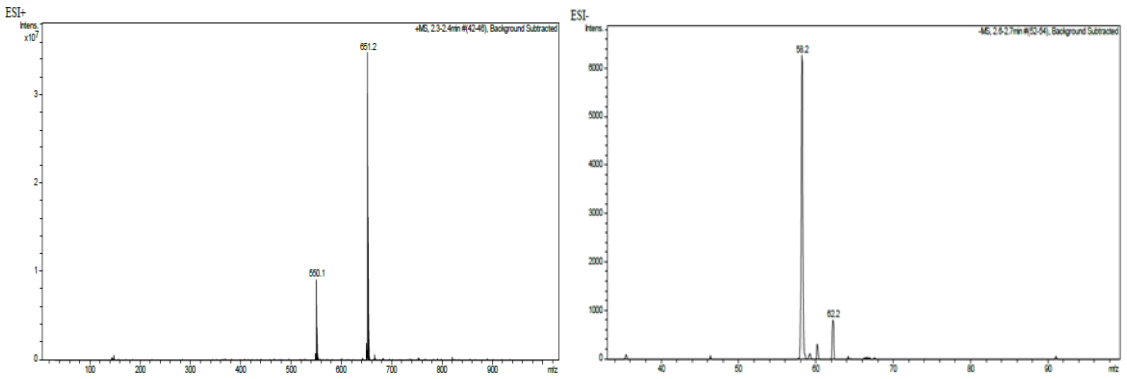

Figure 3.11: MS ESI+ (top) 651.2 *m/z* corresponds to $[(Qsal)Fe(Qapl)]^+$ mass; ESI- (bottom) 58.2 *m/z* corresponds to SCN^- mass.

As expected, the positive mode ESI data indicates the formation of the cationic $[(Qsal)Fe(Qapl)]^+$ parent complex with the appearance of the 550 *m/z* corresponding to $[Fe(Qsal)_2]^+X^-$. The 58.2 *m/z* ratio in ESI- corresponds to the thiocyanate counter ion. Although MS may not be a concrete indicator of sample purity, its elemental analysis definitely supports that the powder worked with was purely the heteroleptic complex. The elemental analysis matched the theoretical values reasonably well with the adjusted formula $[(Qsal)Fe(Qapl)]^+SCN^-$ $0.95MeOH \cdot 1.55H_2O$ (99%). In addition to MS ESI- another method to identify the presence of counter ions is FT-IR. The IR spectrum of $[(Qsal)Fe(Qapl)]^+SCN^-$ is shown below in Figure 3.12.

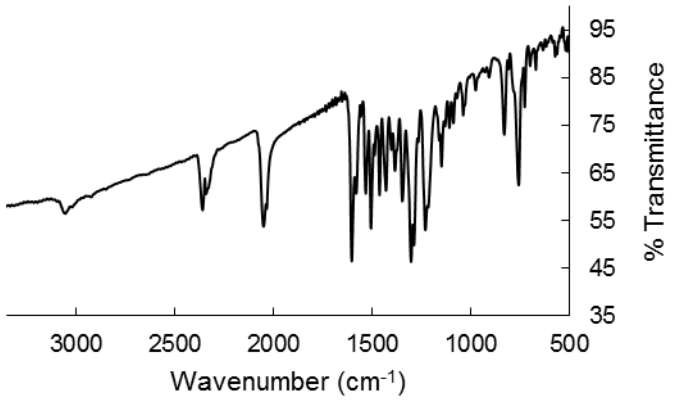

Figure 3.12: FT-IR with KBr on $[(Qsal)Fe(Qapl)]^+SCN^-$ complex.

The S=C=N stretch visible at 2050 cm^{-1} resembles that of O=C=O which is typically observed at 2350 cm^{-1}.[1,20] Despite having similar solubility in THF as complex **12**, suitable crystals for diffraction of complex **13** have not yet been attained.

3.3.2 Magnetic Properties

Once the integration of the SCN^- ion was established, the switching capabilities of $[(Qsal)Fe(Qapl)]^+SCN^-$ complex were examined. The characterized powder of complex **13** was used for SQUID magnetometry to examine the magnetic susceptibility of the complex since single crystals could not be obtained. The variable temperature molar susceptibility profile is presented below in Figure 3.13.

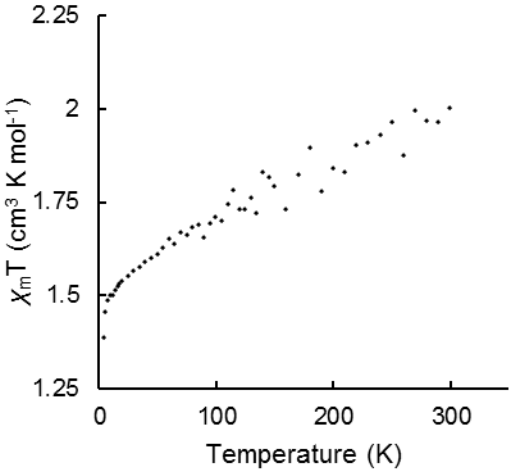

Figure 3.13: *M* vs *T* plot from a clean powder sample of $[(Qsal)Fe(Qapl)]^+SCN^-$.

The profile shows a LS Fe^{3+} center but with an unusual climbing trend between 2 K (1.24 cm^3 K mol^{-1}) to 300 K (2.00 cm^3 K mol^{-1}). In comparison to the molar susceptibility of complex **12**, the $\chi_M T$ value at 300 K here is higher. The fluctuations between 65 K (1.64 cm^3 K mol^{-1}) and 270 K (1.98 cm^3 K mol^{-1}) make evaluating the slope of the *M* vs *T* plot difficult. As with complex **12**, any possible transitioning behaviour as a function of temperature was monitored in solution. The

electronic transitions profiles between 180 K and 300 K for complex **13** are presented below in Figure 3.14.

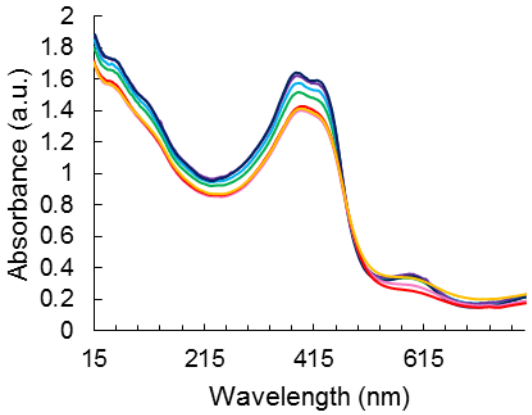

Figure 3.14: VT UV-vis spectra of $[(Qsal)Fe(Qapl)]^{+}SCN^{-}$ in DCM. Temperature range from 183 K (blue) to 303 K (red).

An isosbestic point is observed at 475 nm, occurring at a shorter wavelength than the isosbestic point seen for $[(Qsal)Fe(Qapl)]^{+}BPh_4^{-}$ at 630 nm. It is not unusual that complex **12** and **13** follow a similar trend in solution with regards to electronic absorptions since both complexes in solution exist as the cationic $[(Qsal)Fe(Qapl)]^{+}$ species. Isolating the $[(Qsal)Fe(Qapl)]^{+}$ complex with SCN^{-} did pose new challenges. The solubility of complex **13** was poorer in solvents like DCM and THF versus the BPh_4^{-} species. This made recrystallization of the $[(Qsal)Fe(Qapl)]^{+}SCN^{-}$ complex quite challenging and finding suitable conditions for crystal growing still have yet to be determined. The size difference in the counter ion does likely affect the solubility, packing, and crystallization of the $[(Qsal)Fe(Qapl)]^{+}$ complex. The directional π-stacking interactions significantly contribute to the cooperativity of SCO, more so than the intermolecular isotropic Coulomb and dispersion interactions.[5,7,25,83] Other counter ions including PF_6^{-} and I^{-} were investigated but have not yet been cleanly isolated making them inaccurate for analyses (Appendices C).

3.4.0 Heteroleptic $[(X\text{-}Qsal)Fe(Qapl)]^{+}X^{-}$ Complexes

In addition to utilizing smaller counter ions to enhance the intermolecular contacts within the $[(Qsal)Fe(Qapl)]^{+}$ system, another approach taken involved introducing different types of bonding interactions. A key aspect to generating abrupt switching behaviour in spin-crossover complexes relies heavily on strengthening the intermolecular interactions within the complex.[5,57] Recent literature was suggestive of using different derivatives of the Qsal ligand that would introduce additional bonding patterns. This led to the realization of heteroleptic complexes using halogenated X-Qsal ligands. The C-H···π, C-H···X, and C-X···π types of interactions have been shown to generate highly cooperative supramolecular 3D networks.[57] Examples of halogen interactions are reported by Harding, Murray and colleagues in homoleptic Mn^{3+} $[Mn(Br\text{-}Qsal)_2]$ and $[Mn(Cl\text{-}Qsal)_2]$ complexes.[79]

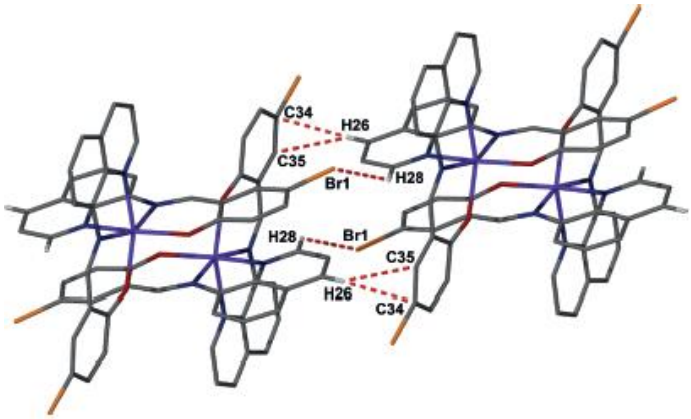

Figure 3.15: Interactions along the *ab* plane in $[Mn(Br\text{-}Qsal)_2]$. Taken from *Eur. J. Inorg. Chem.*, **2015**, 2534-2542.

The intermolecular halogen-based interactions of the $[Mn(Br\text{-}Qsal)_2]$ complexes highlighted in Figure 3.15 occur between C28-H28···Br1 and C33-H33···Br2 which measure 2.892 and 3.031 Å, respectively. Likewise, the $[Mn(Cl\text{-}Qsal)_2]$ linkages occur between C28-H28···Cl1 which are measured at 2.808 Å and C33-H33···Cl2 which measure 2.945 Å.[79] Part of the synthetic strategy

of using X-Qsal ligands is to introduce these types of halogen-based intermolecular interactions between the heteroleptic complexes involving Qapl and other RAL.

3.4.1 Synthesis and Structural Characterization

Following the methodology used to generate the $[(Qsal)FeCl_2(CH_3OH)]$ complex, both Cl-Qsal and Br-Qsal ligands were prepared according to literature.[57] The ^{1}H-NMR and ^{13}C-NMR data are accurate with the data reported in literature (Appendix A.1-A.4).[20] The $[(Cl\text{-}Qsal)FeCl_2(CH_3OH)]$ and $[(Br\text{-}Qsal)FeCl_2(CH_3OH)]$ complexes were prepared in an analogous manner to that of the $[(Qsal)FeCl_2(CH_3OH)]$ complex.

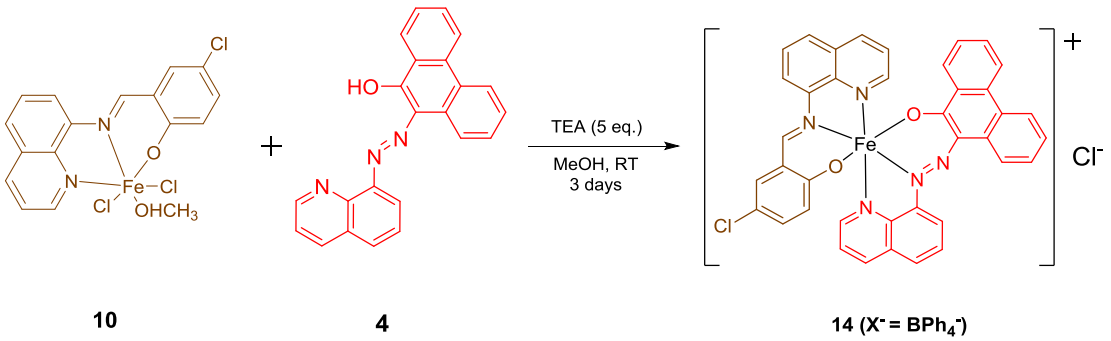

10 **4** **14 (X^- = BPh_4^-)**

Scheme 3.4: Synthesis of $[(Cl\text{-}Qsal)Fe(Qapl)]^+Cl^-$

Single crystals of **14** were grown through a slow diffusion of THF and pentane and have been diffracted at 150 K. The crystal structure $[(Cl\text{-}Qsal)Fe(Qapl)]^+BPh_4^-$ 1.5THF is reported below in Figure 3.16. The independent cationic molecules within the asymmetric unit each hold approximately 3 molecules of THF solvent and a counter ion.

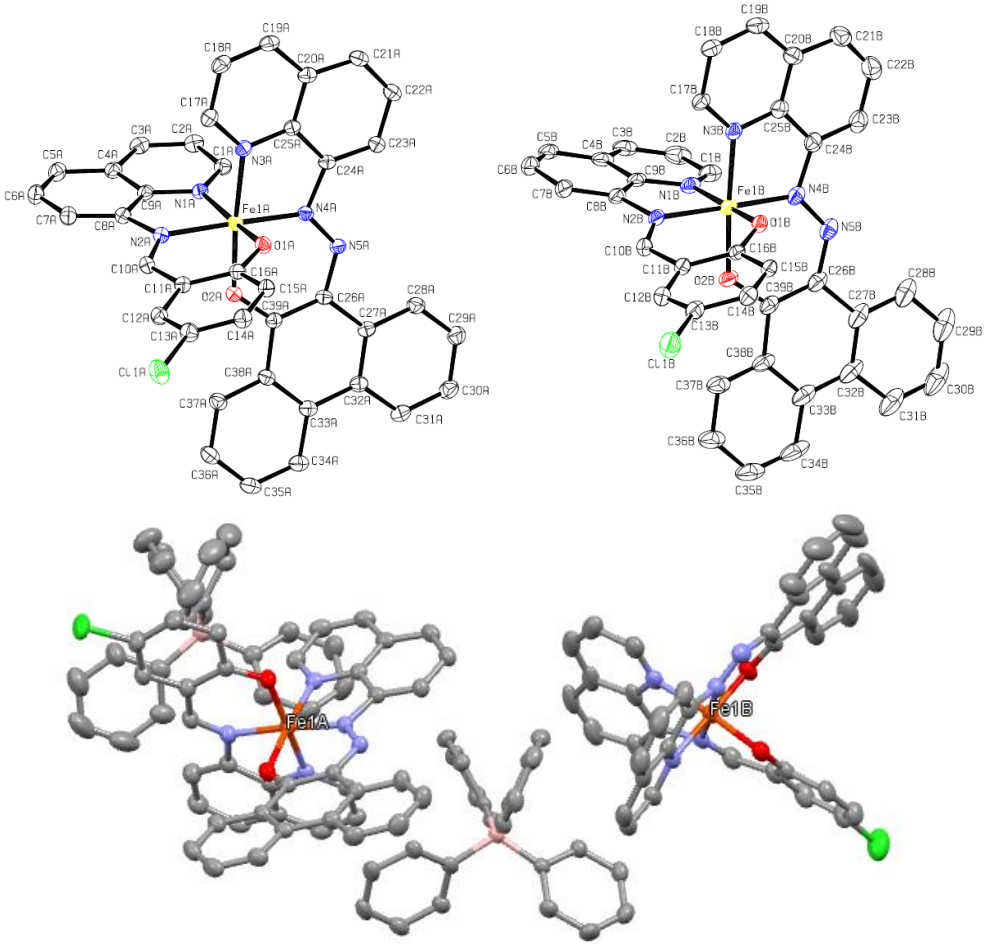

Figure 3.16: Crystal structure of $[(Cl\text{-}Qsal)Fe(Qapl)]^{+}BPh_4^{-}$ 1.5THF (top); Independent $[(Cl\text{-}Qsal)Fe1A(Qapl)]^{+}$ and $[(Cl\text{-}Qsal)Fe1B(Qapl)]^{+}$ cations within the asymmetric unit feature two BPh_4^{-} anions and 2.9 THF solvent molecules. Hydrogen atoms omitted for clarity. Structure solved by Dr. Alan J. Lough from the University of Toronto

Table 3.1: Coordinate bond lengths of $[(Cl\text{-}Qsal)Fe(Qapl)]^{+}BPh_4^{-}$

Bond (Complex A)	Length/ Å	Bond (Complex B)	Length/ Å
Fe(1A)-O(1A)	1.8820(15)	Fe(1B)-O(2B)	1.8666(15)
Fe(1A)-N(4A)	1.8873(17)	Fe(1B)-O(1B)	1.8675(16)
Fe(1A)-O(2A)	1.8969(15)	Fe(1B)-N(4B)	1.8920(2)
Fe(1A)-N(2A)	1.9608(17)	Fe(1B)-N(2B)	1.9550(2)
Fe(1A)-N(3A)	1.9796(18)	Fe(1B)-N(3B)	1.9652(18)
Fe(1A)-N(1A)	1.9893(18)	Fe(1B)-N(1B)	1.9850(2)
N(4A)=N(5A)	1.288(2)	N(4B)=N(5B)	1.297(3)

The coordinate bond distances reported here at low temperature (150 K) correspond to LS Fe^{3+} with distances measured between 1.8-1.9 Å for each molecule in the asymmetric unit, much like

the [(Qsal)Fe(Qapl)]$^{+}$BPh$_4^{-}$ complex. Furthermore, both independent complexes have a N=N$_{azo}$ bond on the Qapl ligand between 1.28-1.29 Å, characteristic of an azo N=N double bond. However, a higher degree of π-π contacts are observed in the molecular packing in contrast to complex **12**.

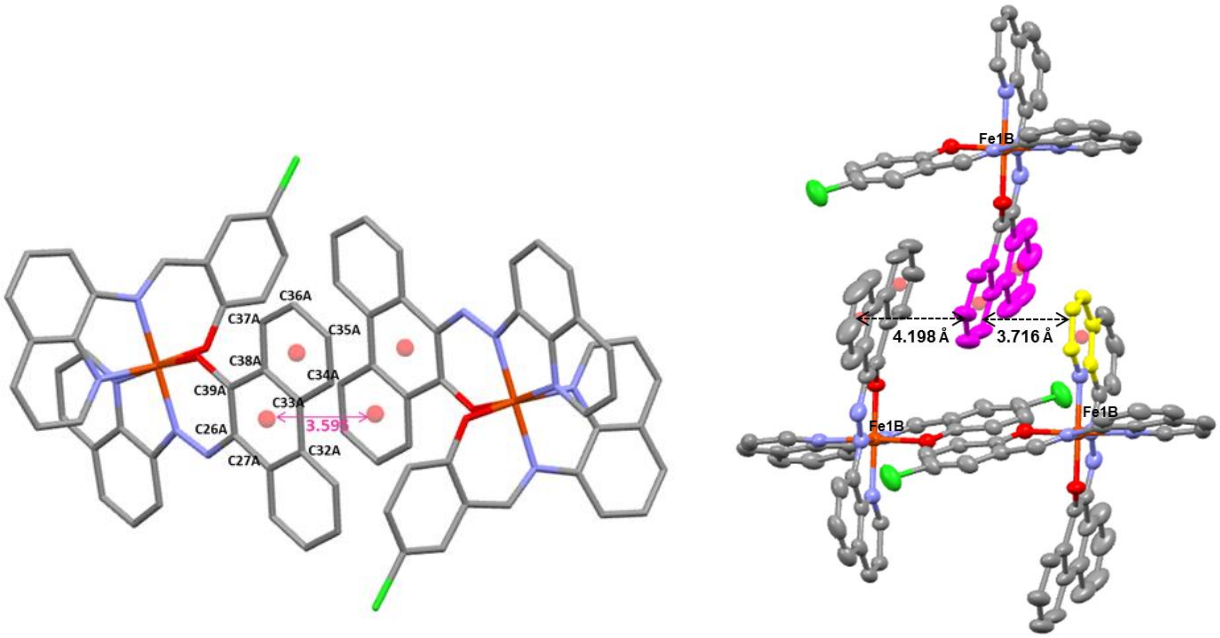

Figure 3.17: Intermolecular π-π contacts in [(Cl-Qsal)Fe1A(Qapl)]$^{+}$BPh$_4^{-}$ (left); Tri-fold intermolecular π-π contacts in [(Cl-Qsal)Fe1B(Qapl)]$^{+}$BPh$_4^{-}$ (right). Hydrogen atoms, solvent molecules, and counter ions omitted for clarity.

No halogen-based intermolecular interactions were observed in the packing based on the orientations of the molecules and the spatial arrangement of the BPh$_4^{-}$ ions as seen in Figure 3.16 and 3.17. However, in the [(Cl-Qsal)Fe1A(Qapl)]$^{+}$BPh$_4^{-}$ molecule, the central and one terminal phenanthrene ring of the Qapl ligand overlap with the terminal and central phenanthrene rings (C26A, C27A, C32A-C39A) of the neighbouring [(Cl-Qsal)Fe1A(Qapl)]$^{+}$BPh$_4^{-}$ complex. Each overlap closes a distance of 3.595 Å, slightly longer than the π-π intermolecular interactions observed in complex **12** by approximately 0.03 Å. An additional π-π contact is observed in the [(Cl-Qsal)Fe1B(Qapl)]$^{+}$BPh$_4^{-}$ molecule between a terminal phenanthrene ring of Qapl and the 8-

aminoquinoline ring of Qapl from adjacent [(Cl-Qsal)Fe1B(Qapl)]$^{+}$BPh$_4^{-}$ complexes highlighted in pink and yellow, respectively (Figure 3.17). Although the π-π overlap between the two phenanthrene rings is significantly larger at 4.198 Å than the overlap observed in [(Cl-Qsal)Fe1A(Qapl)]$^{+}$BPh$_4^{-}$, the distance of 3.716 Å from the additional π-π interaction between the phenanthrene ring and 8-aminoquinoline ring of Qapl in [(Cl-Qsal)Fe1B(Qapl)]$^{+}$BPh$_4^{-}$ is comparable to that observed in the [(Cl-Qsal)Fe1A(Qapl)]$^{+}$BPh$_4^{-}$ complex and complex **12**. These intermolecular interactions could prove promising for enhancing cooperativity among the network of complexes. The packing structure of the Fe1A and Fe1B complexes are shown below in Figure 3.18.

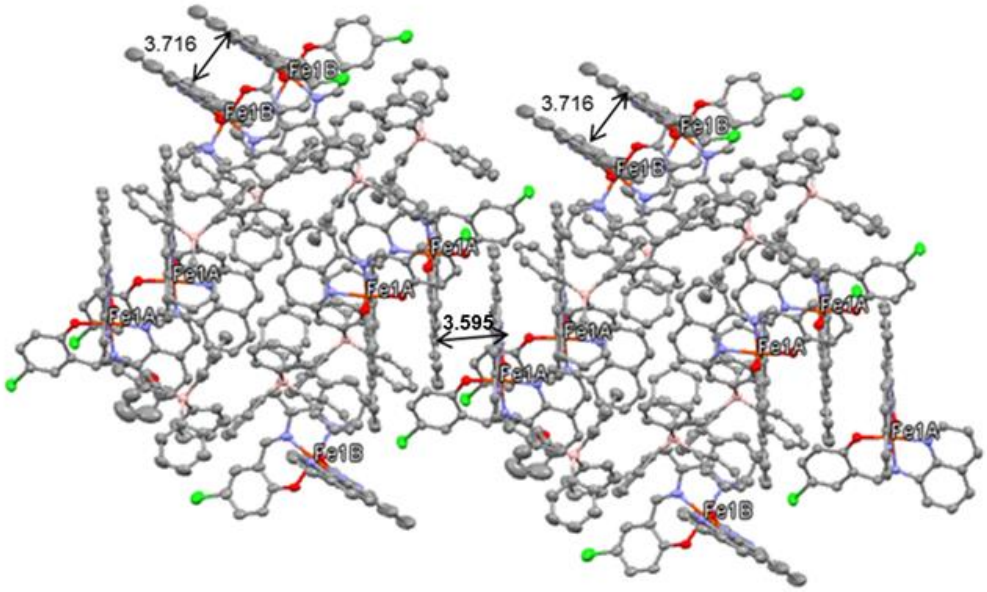

Figure 3.18: Packing structure of [(Cl-Qsal)Fe1A(Qapl)]$^{+}$BPh$_4^{-}$ and [(Cl-Qsal)Fe1B(Qapl)]$^{+}$BPh$_4^{-}$ with labeled intermolecular π-π contacts reported in Å. Hydrogen atoms omitted for clarity.

The chloride substituent on Qsal does not engage in any intermolecular bonding effects as anticipated. The network structure of complex **14** in Figure 3.18 shows a lack of communication between the Fe1A and Fe1B complexes. In fact the only linkages possible in the packing

structure are the π-π overlaps between the phenanthrene rings of Qapl at 3.595 Å among the [(Cl-Qsal)Fe1A(Qapl)]$^{+}$BPh$_4^{-}$ complexes and 3.716 Å among the [(Cl-Qsal)Fe1B(Qapl)]$^{+}$BPh$_4^{-}$ complexes. As already established it is not uncommon that C-X···H interactions exist with Cl-Qsal and Br-Qsal ligands in heteroleptic complexes. However, I-Qsal uniquely engages in C-I···π interactions.[58] Therefore, the preferential bonding intermolecular interactions seems to result in different supramolecular packings. Similarly, X-ray crystallographic studies at temperatures of 100 K and 123 K reported in literature for [(Cl-Qsal)Fe(Br-Qsal)]$^{+}$BPh$_4^{-}$ ·2 DCM revealed LS and mixed spin configurations, respectively.[59] As seen from the work of Harding and Murray presented in Figure 3.20, only two H···X contacts were found in both [Mn(Cl-Qsal)$_2$]OTf and [Mn(Br-Qsal)$_2$]OTf complexes ranging from 2.8-3.0 Å. Other intermolecular interactions which were more likely to contribute to the cooperativity between the Mn^{3+} centers that resulted in a gradual SCO are shown below in Figure 3.19.

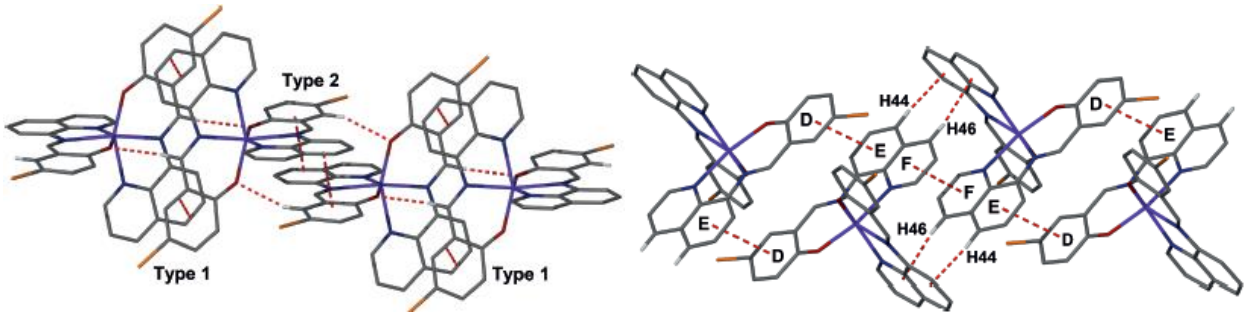

Figure 3.19: Type 1 and type 2 π-π interactions along the *b* axis in [Mn(Br-Qsal)$_2$]. Intermolecular aryl interactions that link the 1D π-π chains. Taken from *Eur. J. Inorg. Chem.*, **2015**, 2534-2542.

Although unable to compare H···X distances, the π-π interactions are similar in measurement. The type 1 π-π interactions (3.654 Å) and type 2 π-π interactions (3.645 Å) are slightly shorter than the π-π interactions observed in complex **14** and occur through the phenyl ring of the salicylaldimine and one of the aromatic rings of the quinoline moiety.[79] Furthermore, these π-π interactions are supported by C-H···O interactions between the coordinated phenoxide oxygen

atoms and the aromatic hydrogens of the ligands. Sets of π-π interactions between the ring systems labeled D, E and F ranging from 3.57 to 3.65 Å are also additional contacts that are not seen in complex **14**.[79] Supporting characterization data are reported below.

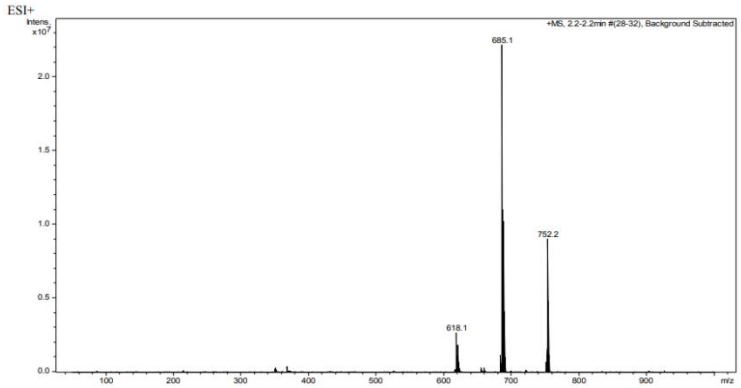

Figure 3.20: MS ESI+ of the $[(Cl\text{-}Qsal)Fe(Qapl)]^+$ complex. ESI- shows 319.1 *m/z* corresponding to BPh_4^-.

The 685.1 *m/z* peak corresponds to the mass of the heteroleptic $[(Cl\text{-}Qsal)Fe(Qapl)]^+$ species. Similarly to other MS data reported in this work, the homoleptic $[Fe(Cl\text{-}Qsal)_2]$ and $[Fe(Qapl)_2]$ complexes appear as 618.1 *m/z* and 752.2 *m/z*, respectively.

At the present time, less is known about the $[(Br\text{-}Qsal)Fe(Qapl)]^+BPh_4^-$ complex as it has been difficult to ascertain its formation with confidence. The MS ESI+ is presented for $[(Br\text{-}Qsal)Fe(Qapl)]^+BPh_4^-$ below in Figure 3.21.

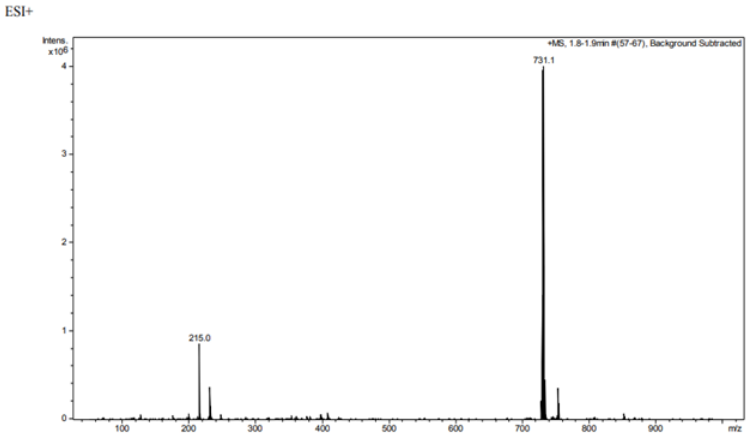

Figure 3.21: MS ESI+ of $[(Br\text{-}Qsal)Fe(Qapl)]^+BPh_4^-$ complex. ESI- shows 319 *m/z* corresponding to BPh_4^-.

The anticipated signal at 731.1 *m/z* which supports the formation of the [(Br-Qsal)Fe(Qapl)]$^{+}$BPh$_4^{-}$ complex, is accompanied by some undefined fragment with a mass/charge ratio of 215.0 *m/z*. The reproducibility of this complex remains uncertain. In fact, one reaction with the [(Br-Qsal)FeCl$_2$(CH$_3$OH)] complex with one equivalent of Qapl led to the formation of a charged homoleptic [Fe(Qapl)$_2$]$^{+}$ complex with a tetraphenylborate counter ion. At this time there is uncertainty with regards to controlling the coordination with the brominated version of Qsal.

3.4.2 Magnetic Properties

The magnetic susceptibility of complex **14** was measured with dried crystal samples by SQUID magnetometry for the possibility of Fe^{3+} SCO. The susceptibility profile is presented below in Figure 3.22.

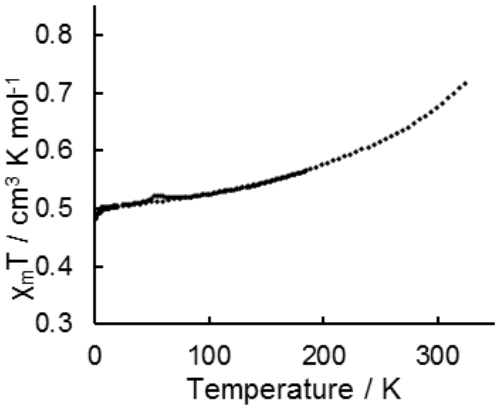

Figure 3.22: Magnetic susceptibility profile of [(Cl-Qsal)Fe(Qapl)]$^{+}$BPh$_4^{-}$ from a dried crystal sample.

The SQUID profile corresponds to a LS Fe^{3+} ion up to temperatures of 325 K. The $\chi_M T$ value reaches 0.71 cm^3 K mol^{-1} at 320 K. In comparison to the literature being followed from Harding and Murray, magnetic susceptibilities of both Cl- and Br- substituted X-Qsal Mn^{3+} complexes were studied using SQUID magnetometry (Figure 3.23).

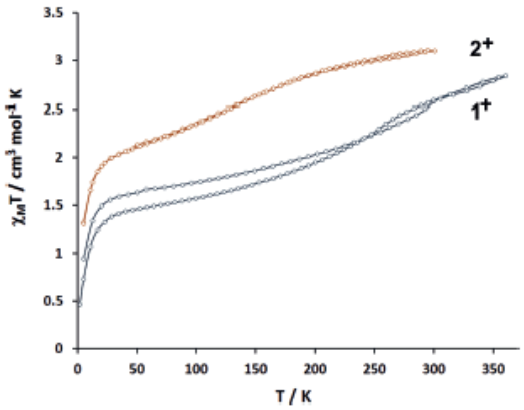

Figure 3.23: Thermal variation of $\chi_M T$ vs. T plots for $[Mn(Cl\text{-}Qsal)_2]^+OTf^-$ **1+** and $[Mn(Br\text{-}Qsal)_2]^+OTf^-$ **2+**. Taken from *Eur. J. Inorg. Chem.*, **2015**, 2534-2542.

Sirirak studied both Mn^{3+} halogenated Qsal complexes up to 300-350 K for the possibility of SCO. Their findings indicate that the $[Mn(Cl\text{-}Qsal)_2]^+OTf^-$ shows a gradual incomplete SCO with a $\chi_M T$ increasing from 1.40 cm^3 mol^{-1} K at 25 K to 2.80 cm^3 mol^{-1} K at 350 K.[79] The $[Mn(Br\text{-}Qsal)_2]OTf$ also shows a gradual SCO but rises more steadily from 2.00 to 3.05 cm^3 mol^{-1} K as the material is warmed to 300 K.[79] Another example, VT magnetic susceptibility measurements examined from polycrystalline material of [(X-Qsal)Fe(thsa)]·*n*MeCN (X= Cl, Br, I) show incomplete SCO with an approximate 50% spin transition occurring at 291 K.[58] The species [(I-Qsal)Fe(thsa)]·MeCN has been reported to remain fully LS up to 360 K.[58] The stability of a LS heteroleptic species featuring a X-Qsal ligand increases from F to I halogen substituents which suggests that the ligand field strength also increases from F to I substituted Qsal ligands.[58] Based on the magnetic susceptibility results for complex **14** and in comparison to literature findings, SCO behaviour may not always be as intuitive with halogenated Qsal ligands in either homoleptic or heteroleptic complexes. Tuning of the counter ions in catonic complexes is presumed to be more influential toward the packing of these complexes based on the crystallographic data.

Both the electronic spectroscopic data and the magnetic susceptibility in solution as a function of temperature are reported below by VT UV-vis and Evans method, respectively, in Figure 3.24.

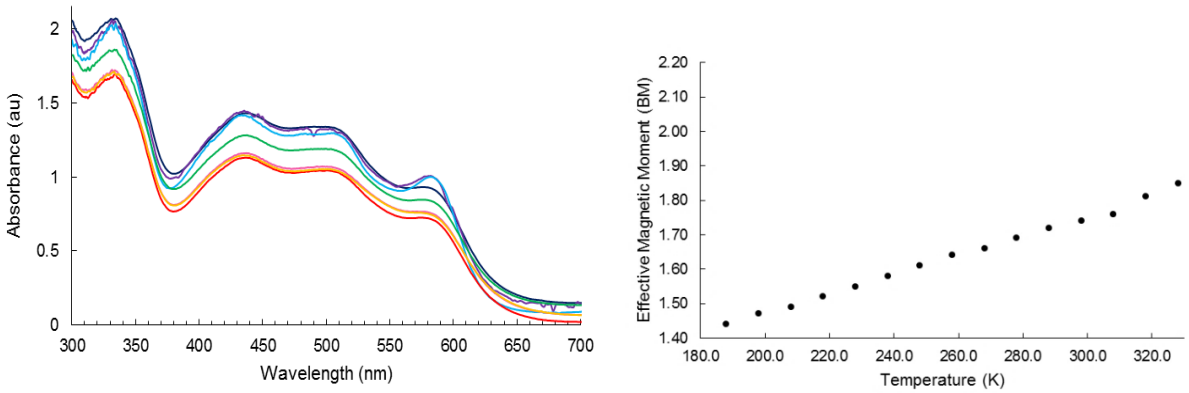

Figure 3.24: VT UV-vis of $[(Cl\text{-}Qsal)Fe(Qapl)]^{+}BPh_4^{-}$ in THF over a temperature range of 183 K to 303 K. VT Evans method in d_8-THF over the temperature range of 183 K to 323 K.

No real indication of switching as a function of temperature was noted from the VT UV-vis experiments. Other examples from literature have noted that X-Qsal dimers do not exhibit any bonding interactions with the halogen substituent between the ligands.[57] The magnetic susceptibility profile of complex **14** in Figure 3.24 also shows no transition between 188 K (1.44 BM) to 328 K (1.85 BM) indicating virtually no change. The consistency of the concentration of the sample in Evans method is crucial when measuring the susceptibility. Factors that can affect the concentration including the possibility of the sample crystallizing, as well as changes in the solvent density as temperatures fluctuate were considered in the calculations and experimentally by repeating the RT measurements of the sample at the beginning and end of the experiment.

3.4.3 Electrochemical Properties

The electrochemical profile of $[(Cl\text{-}Qsal)Fe(Qapl)]^{+}BPh_4^{-}$ in DCM is presented below in Figure 3.25.

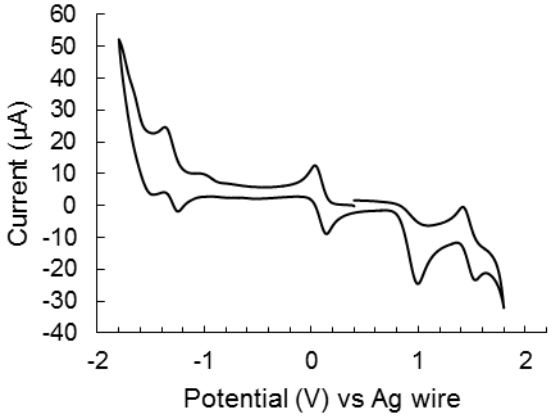

$E_{1/2}$ Anodic vs Ag wire	$E_{1/2}$ Cathodic vs Ag wire
0.7 V (irr), 1.2 V (irr)	-0.1 V (qr), -1.5 V (qr)

Figure 3.25: CV of $[(Cl\text{-}Qsal)Fe(Qapl)]^{+}BPh_4^{-}$ in DCM containing 0.5M $^{n}NBu_4PF_6$ supporting electrolyte.

The CV data resembles that of $[(Qsal)Fe(Qapl)]^{+}BPh_4^{-}$ showing the same reversibility in the cathodic trace corresponding to the azo feature.[17,22] The $E_{1/2}$ values are comparable with those of $[(Qsal)Fe(Qapl)]^{+}BPh_4^{-}$ with the quasi-reversible $E_{1/2}$ value at -0.1 V corresponding to the reduction of Fe^{3+}, and the quasi-reversible $E_{1/2}$ value at -1.5 V corresponding to the reduction of the Qapl ligand.

3.5.0 Homoleptic $[Fe(Qapl)_2]^{+}BPh_4^{-}$ Complex

The number of anionic SCO complexes is limited and sometimes seen with N_2O_4 donor atoms versus the commonly reported N_4O_2 donor set due to the ligand-field strength of oxygen being weaker than nitrogen.[49] However, one example reported in literature revealed magnetic susceptibility values $\chi_M T$ of 3.42 cm^3 K mol^{-1} at 350 K gradually decrease upon cooling to 230 K

with $\chi_M T$ of 0.50 cm^3 K mol^{-1} suggestive of a LS Fe^{3+} center for a $[Fe(azp)_2]$TBA homoleptic complex featuring two azo ligands.[49] Alternatively to the anionic charged complex, a charged cationic homoleptic complex which features two azo ligands has been realized.

3.5.1 Synthesis and Structural Characterization

The original synthesis of $[Fe(Qapl)_2]^+BPh_4^-$ was unusual as the complex was isolated from a reaction involving $[(Br\text{-}Qsal)FeCl_2(CH_3OH)]$ with Qapl in a 1:1 ratio with the intention of generating the heteroleptic species. Prior to this, no other coordination reaction involving Qsal, Cl-Qsal, and an arylazo ligand generated a charged homoleptic Qapl complex with Fe^{3+}. A more controlled reaction was developed to synthesize $[Fe(Qapl)_2]^+BPh_4^-$. Protonated Qapl was mixed with $FeCl_3$ in a 2:1 ratio in methanol at RT exposed to air. The reaction was left to stir overnight and the complex was filtered as a dark purple powder. A low temperature crystal structure was obtained and is presented below.

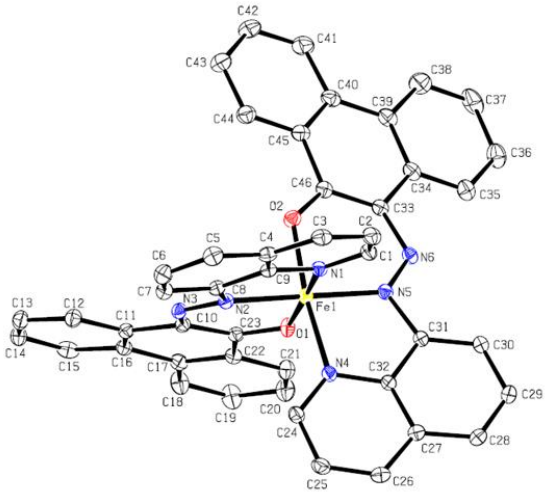

Figure 3.26: Molecular structure of $[Fe(Qapl)_2]^+BPh_4^-$. Counter ion and solvent molecules omitted. Structure solved by Dr. Alan J. Lough from the University of Toronto.

Table 3.2: Coordinate bond lengths and angles

Bond	Length/ Å	Atoms	Angle/ °
Fe(1)-O(1)	1.8631(14)	O(1)-Fe(1)-O(2)	93.50(6)
Fe(1)-O(2)	1.8669(14)	O(1)-Fe(1)-N(2)	91.72(6)
Fe(1)-N(2)	1.8973(16)	O(2)-Fe(1)-N(2)	89.24(6)
Fe(1)-N(5)	1.9049(16)	O(1)-Fe(1)-N(5)	87.29(6)
Fe(1)-N(4)	1.9599(16)	O(2)-Fe(1)-N(5)	90.86(6)
Fe(1)-N(1)	1.9708(16)	N(2)-Fe(1)-N(5)	179.01(7)
N(2)=N(3)	1.2960(2)	O(1)-Fe(1)-N(4)	91.24(6)
N(5)=N(6)	1.2880(2)	O(2)-Fe(1)-N(4)	172.73(7)
		N(2)-Fe(1)-N(4)	96.14(7)
		N(5)-Fe(1)-N(4)	83.85(7)
		O(1)-Fe(1)-N(1)	174.30(6)
		O(2)-Fe(1)-N(1)	89.96(6)
		N(2)-Fe(1)-N(1)	83.79(7)
		N(5)-Fe(1)-N(1)	97.20(7)
		N(4)-Fe(1)-N(1)	85.78(7)

The coordinate bond distances are similar to that reported for complex **12**, corresponding to a LS Fe^{3+} center.[5,7,25,83] The N=N bond length of Qapl correspond to azo nitrogen double bond.[33] The overlap between the terminal rings of the phenanthrene moiety resembles more closely the overlap observed between the phenanthrene rings of the Fe1A complex **14** rather than the overlap of complex **12**.

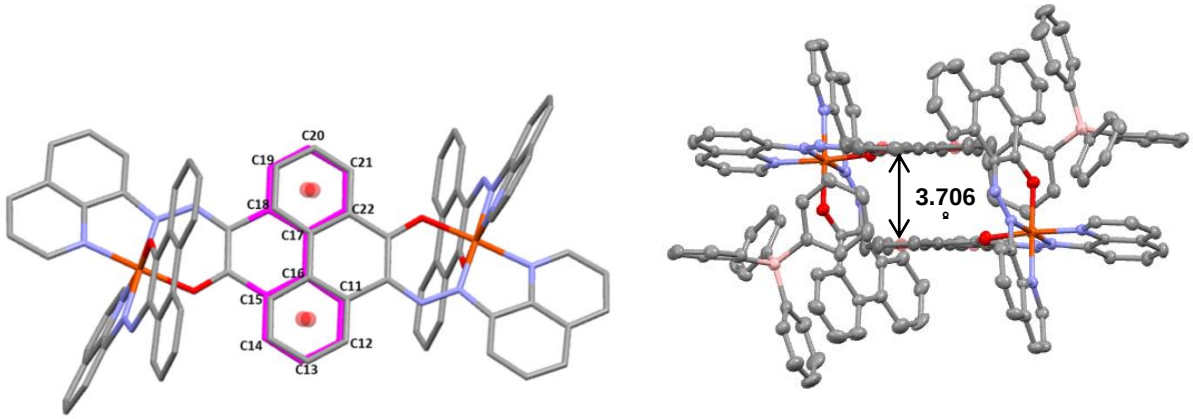

Figure 3.27: Intermolecular π-π overlap in $[Fe(Qapl)_2]^+BPh_4^-$ reported in Å. Hydrogen atoms and solvent molecules omitted.

The intermolecular π-π overlap shows a greater alignment between the phenanthrene rings of Qapl. The 3.706 Å gap of the π-π intermolecular interaction is similar to the 3.730 Å of Fe1A in complex **14**. The packing of $[Fe(Qapl)_2]^+BPh_4^-$ complexes is shown below in Figure 3.28.

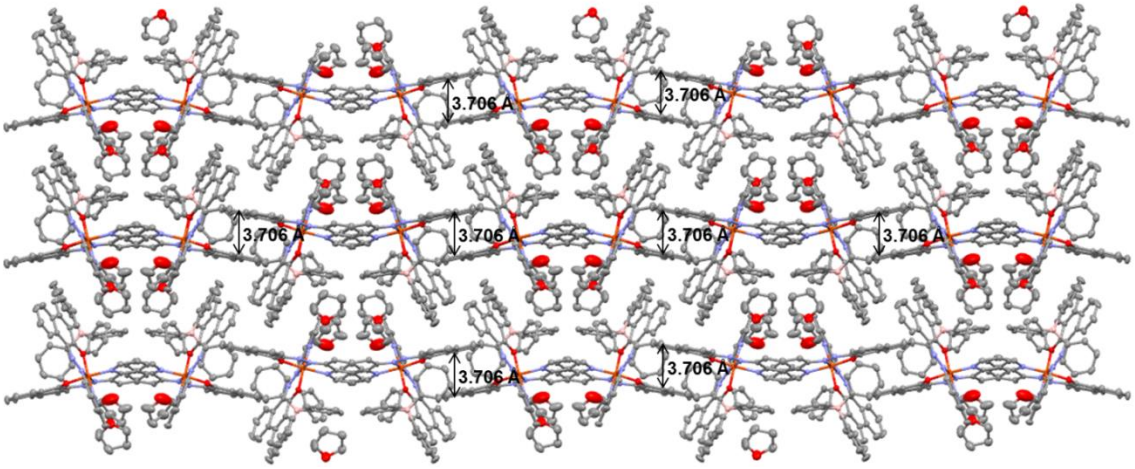

Figure 3.28: Packing structure of $[Fe(Qapl)_2]^+BPh_4^-$. Hydrogen atoms omitted for clarity.

The packing reveals this overlap to be the only π-π intermolecular interaction between the $[Fe(Qapl)_2]^+BPh_4^-$ complexes. The network forms individual lines that run parallel with each other with a slight kink that occurs where there is no π-π overlap between the complexes. Despite the presence of the bulky BPh_4^- counter ion, the kinks in the chains of the complexes appear to be a result of the π-π contacts between the neighbouring phenanthrene rings of Qapl pulling on the complexes to hold them together.

Because of the inconsistency of the synthetic route as well as the uncertainty of the reproduction of this complex, crystal or powder samples could not yet be analyzed for potential SCO behaviour in solid state or solution.

3.6.0 Heteroleptic $[(Qsal)Fe(Phpl)]^+Cl^-$ Complex

The 9-[2-(2-pyridyl)hydrazono]-1-phenalenol (Phpl) compound, shown below in Figure 3.29 is a tridentate hydrazine ligand. The ligand is prepared in three steps according to the

methodology described in Dale et al.[35] The synthesis of the preliminary 9-hydroxy-1-phenalenone and the subsequent 9-methoxy-1-phenalenone known.[61,62] The resulting species is a tautomer that is isolated as the enol hydrazine form as suggested by the ^{1}H-NMR (Appendix A.10, A.11) with the O-H resonance appearing beyond 13 ppm.[35] The maximum absorbance value at 460 nm of the red ligand is indicative of a transition between the delocalized π-frontier orbitals.[35] The initial interest in Phpl as it pertains to this research work lies in its potential redox activity as well as its high conjugation to provide stability.

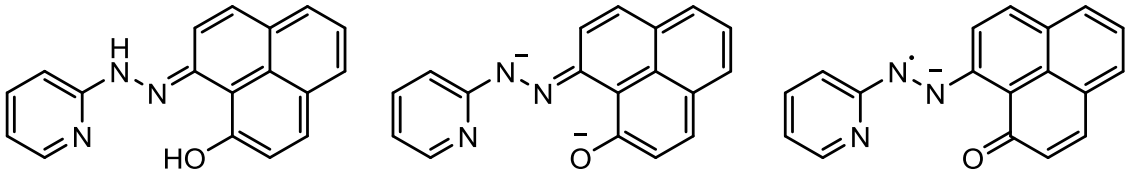

Figure 3.29: Structure of 9-[2-(2-pyridyl)hydrazono]-1-phenalenol (Phpl) ligand, fully protonated (left); dianion form (center); radical anion (right).

Double deprotonation of Phpl to produce the dianionic moiety could be oxidized to give rise to the radical anionic species where the spin density could be localized over the phenalenyl rings or on the low lying π*-orbitals of the azo group.[32] The two different oxidation states of Phpl are shown in Figure 3.29.Coordination of Phpl to $Fe(NO_3)_3 \bullet 9H_2O$ produces a homoleptic Phpl iron complex that shows semiconducting properties. Single crystals of this complex were found to be diamagnetic LS Fe^{3+} with S=1/2 that is antiferromagnetically coupled to a radical-anion of Phpl.[35]

3.6.1 Synthesis and Structural Characterization

The unique features of the Phpl ligand in conjunction with the observations from its coordination to an iron ion led to experimenting with coordination to the $[(Qsal)FeCl_2(CH_3OH)]$ complex to generate the heteroleptic complex.

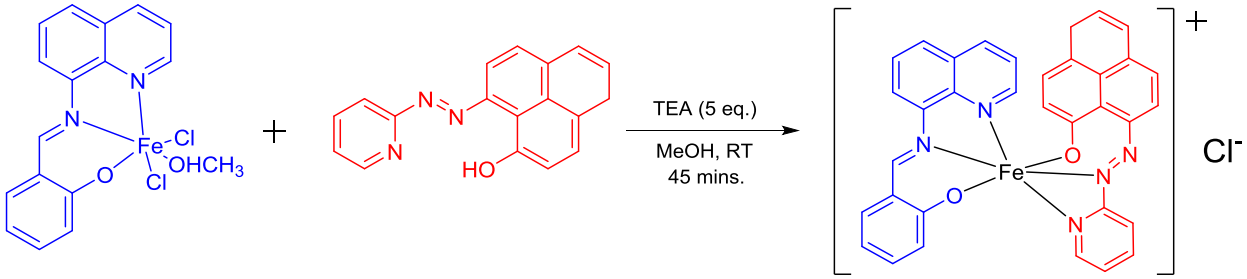

9 **7** **15**

Scheme 3.5: Synthesis of $[(Qsal)Fe(Phpl)]^{+}Cl^{-}$

Complex **15** crystallizes as a fine dark maroon microcrystalline. The elemental analysis determined a 95-99% match with the molecular formula $[(Qsal)Fe(Phpl)]^{+}Cl^{-} \cdot MeOH$. The spectrometric data for the heteroleptic complex is presented below in Figure 3.30.

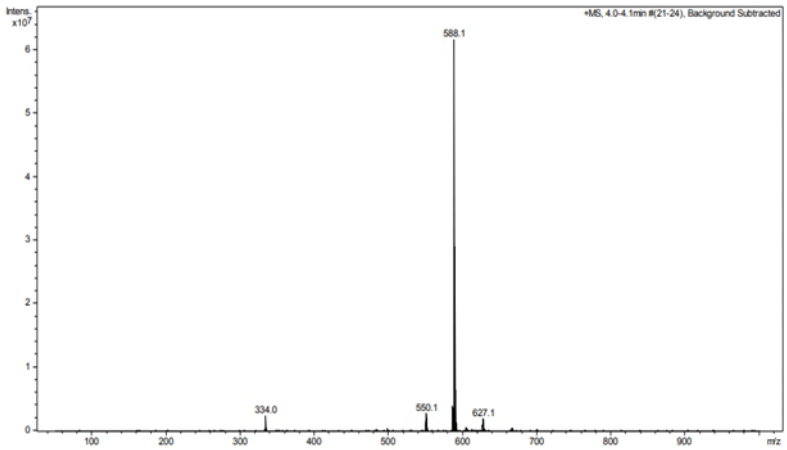

Figure 3.30: MS ESI+ of the $[(Qsal)Fe(Phpl)]^{+}$ complex.

The 588.1 *m/z* corresponds to the heteroleptic $[(Qsal)Fe(Phpl)]^{+}$ mass. Based on the mass to charge ratio the Phpl exists as a radical anion. This is further supported by the SQUID and Mössbauer data presented below in Figures 3.31 and 3.32, respectively. The $\chi_M T$ values between 2 K to 300 K reflect a LS Fe^{3+} center which correlates with the low isomer shift values observed from Mössbauer associated with Fe^{3+}. Based on these results, the Phpl ligand is rationalized to be a fully deprotonated and exist as a radical anion in complex **15**.

3.6.2 Magnetic Properties

The magnetic susceptibilty and Mössbauer data are presented below in Figure 3.31 and 3.33, respectively.

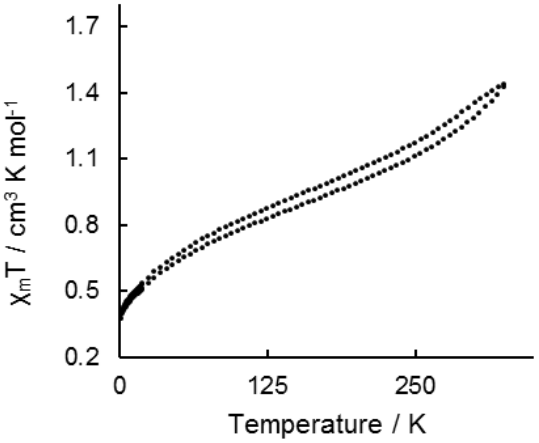

Figure 3.31: $\chi_M T$ vs T profile for $[(Qsal)Fe(Phpl)]^+Cl^-$ over a temperature range of 2 K to 325 K. Experiment was done using a dried powder sample.

At low temperature the $\chi_M T$ value reflects a single unpaired electron indicative of LS Fe^{3+}. The $\chi_M T$ values show little change starting at low temperatures where the $\chi_M T$ of 0.77 cm^3 K mol^{-1} at 90 K is noted to gently rise to approximately 1.20 cm^3 K mol^{-1} at 270 K. The $\chi_M T$ values correspond with the Mössbauer data at low temperature having predominantly LS Fe^{3+} seen from the low isomer shift values and asymmetric doublet at 6 K. More discernable changes are noted to take place at RT and beyond as indicated from both SQUID and Mössbauer data. The $\chi_M T$ value continues to rise beyond RT and at 325 K reaches 1.44 cm^3 K mol^{-1}. This is where the experiment reaches its temperature limit due to the solvent system and sample composition. The low temperature data is observed to be LS Fe^{3+} (S=1/2) antiferromagnetically coupled with the radical anion form of Phpl depicted in Figure 3.32. However, the Mössbauer data at low

temperature observes no S= 0 state and indicates some ratio of HS Fe^{3+} (S= 5/2) which propagates at RT as suggested by the higher isomer shifts.

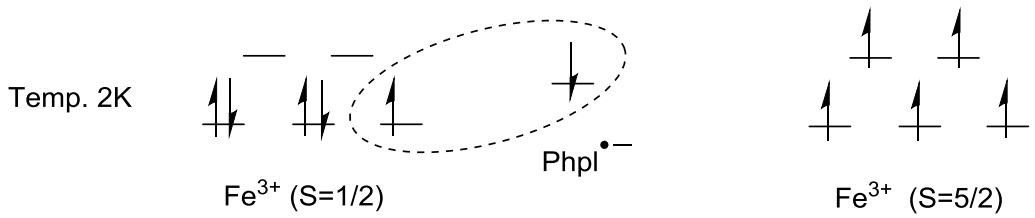

Figure 3.32: Fe^{3+} (S=1/2) with Phpl radical anion antiferromagnetically coupled at 2 K.

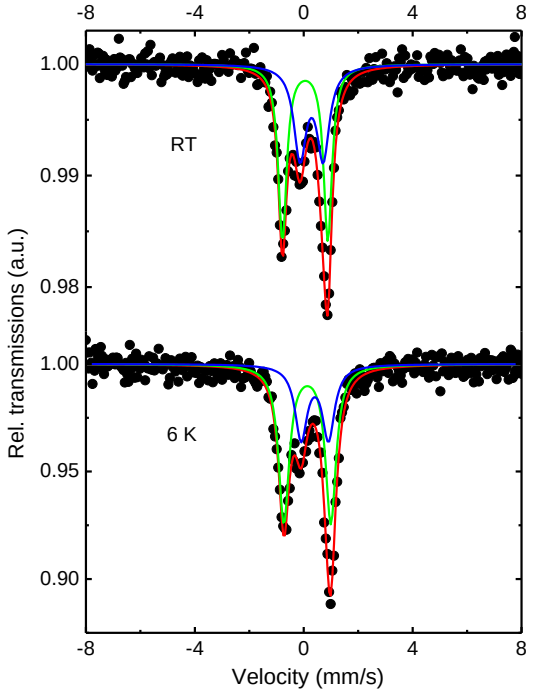

Figure 3.33: Mössbauer spectroscopy data for $[(Qsal)Fe(Phpl)]^{+}Cl^{-}$ at 298 K and 6K.

Table 3.3: Mössbauer Data

Temp. (K)	Γ (mm/s)	δ (mm/s)	ΔE_Q (mm/s)	Fe site occupancy (%)
6	0.47(2) 0.54(5)	0.23(1) 0.51(2)	1.72(2) 1.00(5)	65 35
RT	0.37(2) 0.55(3)	0.153(4) 0.390(8)	1.67(1) 0.85(2)	57 43

The lower isomer shift (δ) values of 0.153 mm/s and 0.390 mm/s correspond to the high oxidation state of Fe^{3+}. These results are attributed to Fe^{3+} having less *d*-electrons than Fe^{2+} and therefore experience less of a shielding effect from the *s*-electrons which results in a lower isomer shift value.[3,4,54] Comparable isomer shift values are seen with the $[Fe(Qsal\text{-}5\text{-}OMe)_2]^+Cl^-$ $\cdot MeCN\cdot H_2O$ complex introduced in Chapter 1.0, which gives rise to an asymmetric doublet upon cooling. This asymmetric doublet is highlighted in Figure 3.34 below.

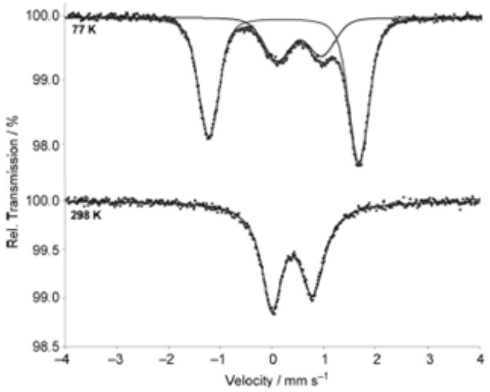

Figure 3.34: VT Mössbauer data of $[Fe(Qsal\text{-}5\text{-}OMe)_2]^+Cl^- \cdot MeCN\cdot H_2O$ complex at 298 K (bottom) and 77 K (top). Taken from *Chem. Eur. J.*, **2013**, 19, 1082-1090.

Upon cooling, the complex gives rise to an asymmetric doublet that begins to form with an δ value of 0.20 mm/s and a ΔE_Q value of 2.89 mm/s. These values for both parameters are indicative of LS Fe^{3+}.[54] The HS Fe^{3+} centers, having an δ value of 0.52 mm/s and a ΔE_Q value of 0.86 mm/s are noted to exist in a fraction of 28% compared to LS at 77 K.[54] For complex **15** the quadrupole splitting (ΔE_Q) was observed to be larger for LS with an occupancy of 57% and smaller for HS with an occupancy of 43%. The smaller quadrupole splitting for HS Fe^{3+} is likely due to the symmetrical configuration of the *d*-subshells. This Mössbauer data indicates incomplete spin-crossover since there is still some ratio of HS Fe^{3+} (S=5/2) present at 2 K.

3.7.0 Homoleptic [Fe(Qan)$_2$] Complex

The 1-(8-quinolylazo)-2-naphthol (Qan) ligand was synthesized for the intent to modify an oxidized charcoal sorbent that efficiently absorbs Cu^{2+} and Zn^{2+} ions to form surface electroneutral chelate complexes for sample preparation for atomic absorption or photometric analysis of water.[67] Its structure is shown below in Figure 3.35.

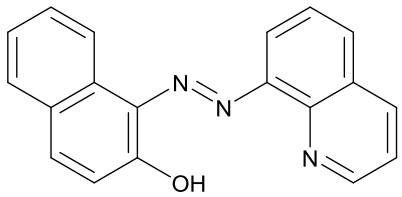

Figure 3.35: Molecular structure of Qan ligand.

Qan is prepared by first reacting a slight excess of $NaNO_2$ with 8-aminoquinoline in water and 18% HCl to produce the diazonium salt. The diazonium salt solution is added to 2-naphthol in a mixture of KOH and water. After reacting, the solution is neutralized with acetic acid and Qan is filtered off as a dark red powder.[67] The ligand offers the same N_2O coordination motif as both Qapl and Qsal. However, in contrast to Qapl, Qan is a smaller ligand with less conjugation, which could pose problematic for delocalization if a radical formed in the system.

3.7.1 Synthesis and Structural Characterization

The synthetic approach to generate the heteroleptic [(Qsal)Fe(Qan)] complex remained conventional to the approach taken for other complexes reported in this work. However, from the recrystallization the homoleptic [Fe(Qan)$_2$] species was isolated. Later, the synthesis was modified as illustrated in Scheme 3.6 to reproduce only the homoleptic [Fe(Qan)$_2$] complex to further study its properties.

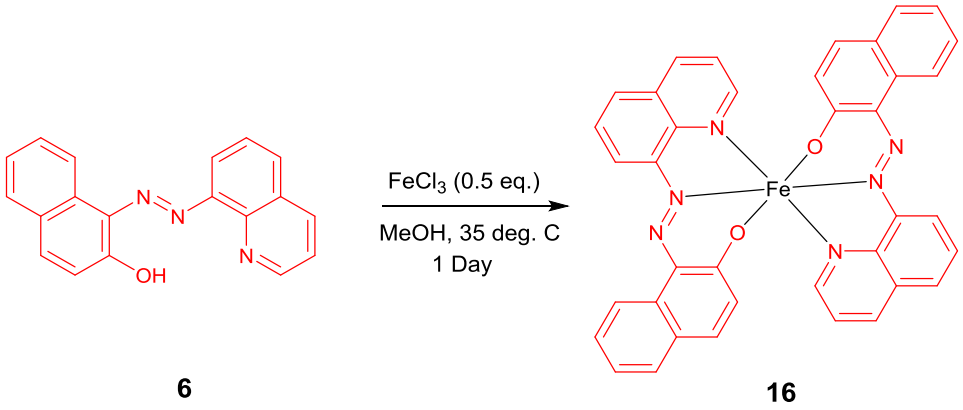

6 **16**

Scheme 3.6: Synthesis of $[Fe(Qan)_2]$

Single black needle-shaped crystals of the $[Fe(Qan)_2]$ complex were grown by slow diffusion with DCM and ether and a crystal was diffracted at low temperature reported below in Figure 3.36.

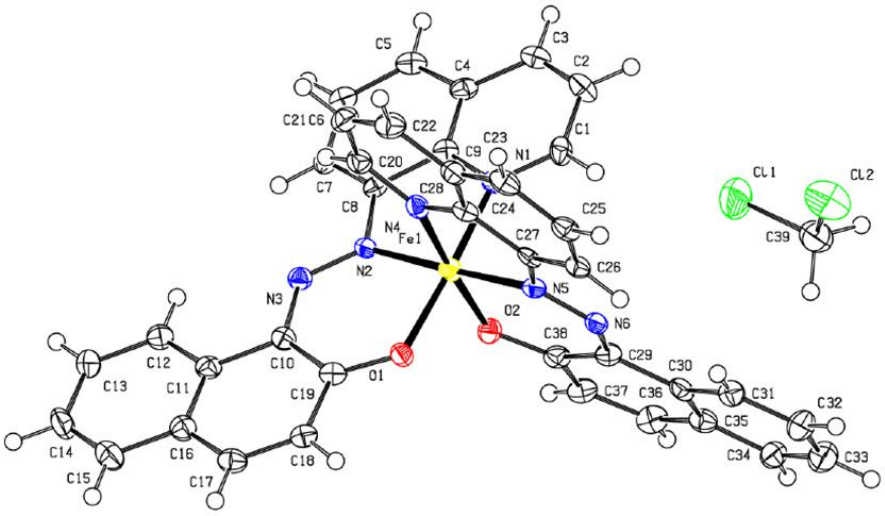

Figure 3.36: Molecular structure of $[Fe(Qan)_2]$ at 100 K. Hydrogens excluded for clarity. Structure solved by Dr. Brian O. Patrick from University of British Columbia.

Table 3.4: Coordinate bond lengths of the [Fe(Qan)$_2$] complex

Bond	Length/Å	Atoms	Angle/°
Fe1-O1	1.928(2)	O1-Fe1-N1	175.76(12)
Fe1-O2	1.922(3)	O1-Fe1-N4	90.18(11)
Fe1-N1	1.971(3)	O2-Fe1-O1	90.93(11)
Fe1-N2	1.895(3)	O2-Fe1-N1	88.41(11)
Fe1-N4	1.965(3)	O2-Fe1-N4	175.72(12)
Fe1-N5	1.895(3)	N2-Fe1-O1	91.90(12)
N2=N3	1.299(4)	N2-Fe1-O2	89.78(12)
N5=N6	1.298(4)	N2-Fe1-N1	83.91(13)
		N2-Fe1-N4	94.31(13)
		N4-Fe1-N1	90.79(12)
		N5-Fe1-O1	88.82(12)
		N5-Fe1-O2	92.23(12)
		N5-Fe1-N1	95.40(13)
		N5-Fe1-N2	177.86(13)
		N5-Fe1-N4	83.66(13)

The coordinate bond lengths determined are comparable to the other heteroleptic [(Qsal)Fe(RAL)]$^+$X$^-$ complexes reported in this work. These short coordinate lengths ranging from 1.895-1.971 Å for iron centers reflect a LS iron as described earlier. However, the iron center presented here has been determined to exist as a LS Fe^{2+} center, given the coordination to two monoanionic ligands with bond lengths not pertaining to any sort of radical formation and with no counter ion present with the complex. The packing structure of complex **16** is shown in Figure 3.37. Each individual complex is associated with a single molecule of DCM.

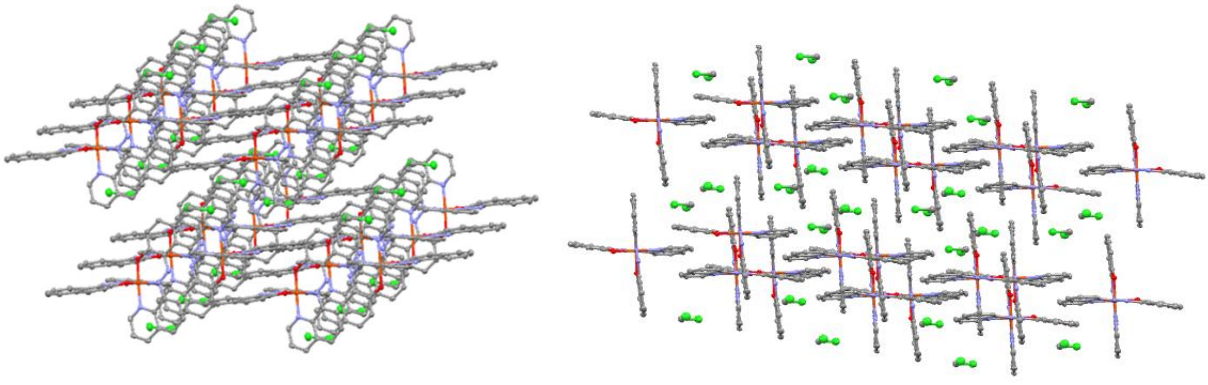

Figure 3.37: Packing structure of [Fe(Qan)$_2$]. Hydrogen atoms omitted for clarity.

Further characterization by mass spectrometry supports the formation of the synthetic target.

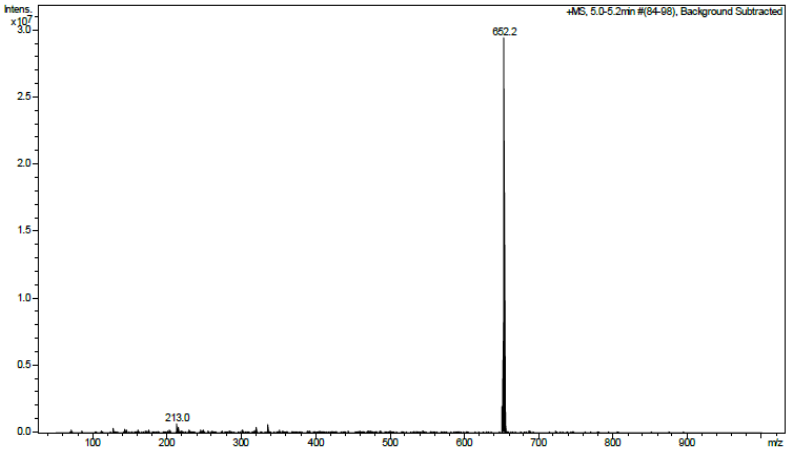

Figure 3.38: MS ESI+ for $[Fe(Qan)_2]$ complex.

The 652.2 *m/z* corresponds to the mass of the homoleptic iron-Qan complex. Unlike the $[(Qsal)Fe(Qapl)]^+$ species, there was no evidence of a cationic heteroleptic version of iron-(Qan)(Qsal) present in the filtrate of the reaction, nor could any species be precipitated out with a large counter ion like BPh_4^-. No counter ion was found present in the ESI– mode which further supports that the homoleptic $[Fe(Qan)_2]$ complex is neutral.

There is no discernable signal produced at RT NMR which suggests that the complex may be paramagnetic in some solvents. This homoleptic Fe^{2+} complex does not exhibit any of the desired characteristics or properties that pertain to the objectives outlined in this work. The χ_M was calculated as 0.01 cm^3/mol from the experimentally determined χ_g value using a Gouy balance. This value coincides with a diamagnetic LS Fe^{2+} species at RT.[1,3,7]

3.8.0 Heteroleptic $[(Qsal)Co(Qapl)]^+BPh_4^-$ Complex

In addition to iron, cobalt was another metal explored falling in the d^4-d^7 range of metal ions for possible SCO candidates. Two heteroleptic cobalt complexes using Qsal with Qapl and Papl, generated in a similar manner to that of the iron complexes, are presented in the following

Sections. Some of the synthetic methods and characterization were carried out by Zackery Watts in partial fulfillment of his undergraduate thesis in the Lemaire group.[90]

3.8.1 Synthesis and Structural Characterization

A cobalt-Qsal complex containing a non-redox-active ancillary ligand was synthesized. Initial attempts to generate the cobalt-Qsal complex involved the use of $CoCl_2 \cdot 6\ H_2O$. Reactions with $CoCl_2 \cdot 6\ H_2O$ resulted in only the formation of homoleptic $[Co(Qsal)_2]$ species with little to no control over the reaction. To resolve this issue another source of cobalt, $Co(OAc)_2 \cdot 4\ H_2O$, was used under the rationale that the acetate groups would provide more stability and control over the formation of the monosubstituted product. The stability between Co^{2+} oxidizing to Co^{3+} was taken into consideration and therefore the reactions were carried out under a nitrogen atmosphere.

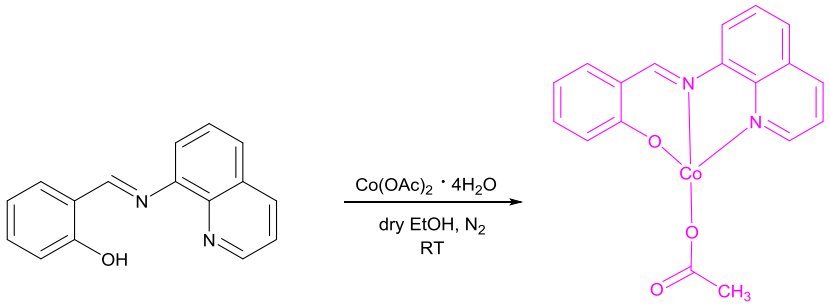

1 **17**

Scheme 3.7: Synthesis of $[(Qsal)Co(OAc)] \cdot 1.15\ CH_3CH_2OH \cdot 2\ H_2O$

Complex **17** was formed in this manner and isolated as a light orange powder. Although the complete structure remains uncertain, spectrometric data is reported in Appendix D.1 and elemental analysis supports a complex in the form of $[(Qsal)Co(OAc)] \cdot 1.15\ CH_3CH_2OH \cdot 2\ H_2O$. Further characterization of complex **17** by FT-IR is included in Appendix C.9. NMR was not a suitable method for analysis regarding structure elucidation or probing diamagnetic character due to the poor solubility of the complex in deuterated solvents. To accommodate for

this a Gouy balance was used to experimentally determine that the complex possessed a HS Co^{2+} center at a μ_{eff} of 3.98 BM.[90] The electronic absorption profile of complex **17** is overlaid and compared with the profiles of the Qsal ligand and homoleptic $[Co(Qsal)_2]$ at RT in Appendix B.7. In each experiment the powder sample was used at a relatively consistent concentration in methanol. Complex **17** was discerned to be some cobalt acetate species containing one Qsal ligand and able to generate heteroleptic complexes. Following the methodologies used for the heteroleptic iron systems, the first heteroleptic cobalt complex synthesized was $[(Qsal)Co(Qapl)]^{+}BPh_4^{-}$.

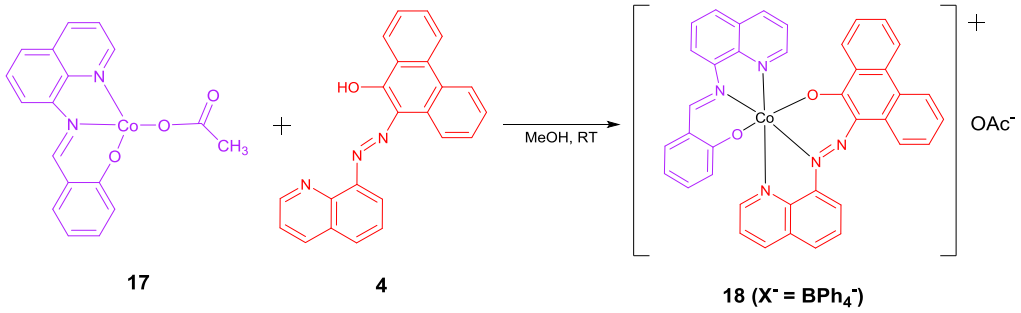

17 **4** **18 (X^{-} = BPh_4^{-})**

Scheme 3.8: Synthesis of $[(Qsal)Co(Qapl)]^{+}OAc^{-}$

Crystallization of complex **18** was analogous to that of $[(Qsal)Fe(Qapl)]^{+}BPh_4^{-}$ which is not unexpected due to their shared solubility in THF as a result of the ligands and large tetraphenylborate counter ion. A black rod-shaped single crystal was diffracted and the structure of the heteroleptic complex is reported below in Figure 3.39.

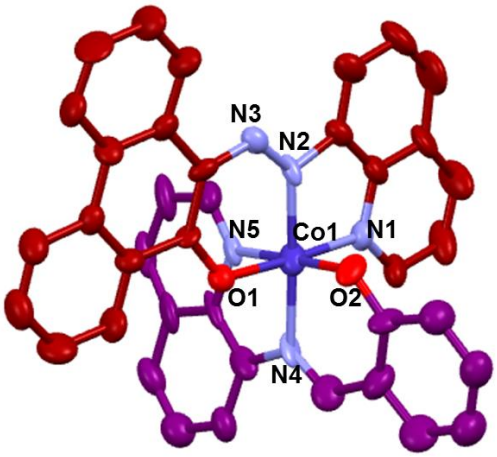

Figure 3.39: Molecular structure of the $[(Qsal)Co(Qapl)]^{+}BPh_4^{-}$ complex. Hydrogens excluded for clarity. Structure solved by the Pilkington group from Brock University.

Table 3.5: Coordinate bond lengths of the $[(Qsal)Co(Qapl)]^{+}BPh_4^{-}$ complex

Bond	Bond length/Å
Co1-N1	1.910(9)
Co2-N2	1.896(6)
Co1-N4	1.936(6)
Co1-N5	1.934(9)
Co1-O1	1.886(6)
Co1-O2	1.883(8)
N2=N3	1.253(6)

Much like the octahedral heteroleptic iron systems, the ligands of the heteroleptic cobalt complex are near perpendicular to each other with coordinate bond distances all under 2.0 Å, which is typically observed with Co^{3+}.[29] The Co-O bonds are the shortest coordinate bonds observed, in particular the Co-O2 bond distance of 1.883 Å from the Qsal ligand. The $N_{quinoline}$ and N_{imine} are slightly longer with bond lengths of 1.934 Å and 1.936 Å, respectively. The N=N bond length of 1.253 Å is typical for an azo bond. The Co1-$N1_{quinoline}$ coordinate bond of 1.910 Å and the Co2-$N2_{azo}$ coordinate bond of 1.896 Å are typical bond distances for a LS Co^{3+} configuration.[29] The intermolecular interactions and packing structure are shown in Figure 3.40.

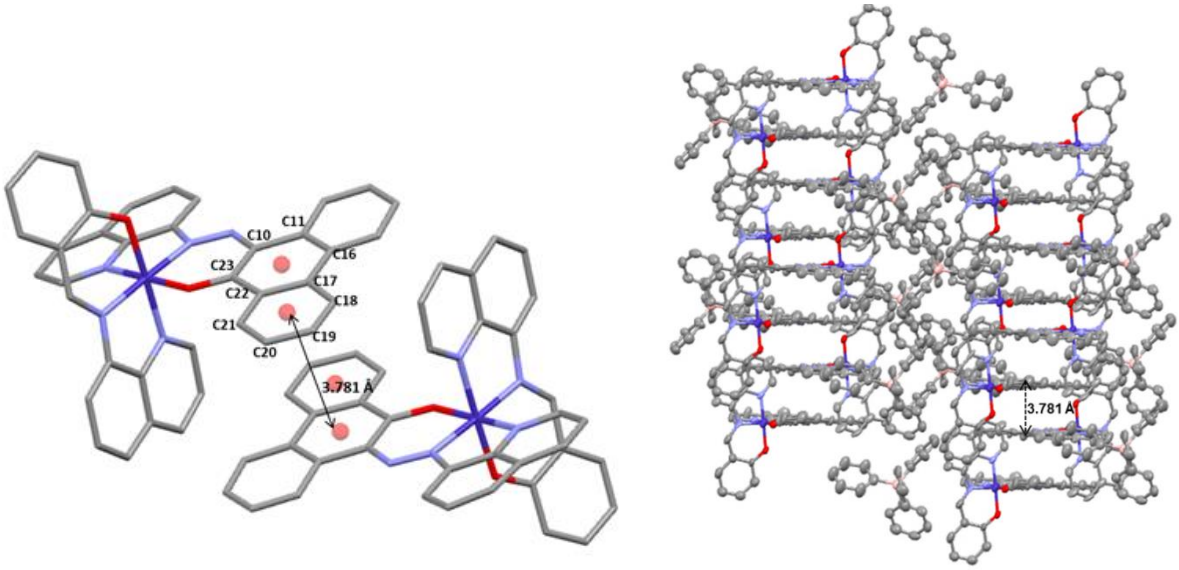

Figure 3.40: Intermolecular π-π interactions and packing of $[(Qsal)Co(Qapl)]^{+}BPh_4^{-}$. Hydrogen atoms omitted for clarity.

Complex **18** shares the same intermolecular π-π interaction as complex **12** between the central and one terminal ring from the phenanthrene moiety of Qapl. The distance that closes this π-π contact is about 0.218 Å longer than in complex **12**. Despite their structural similarities between the ligands and counter ion as well as the shared intermolecular interaction, the packing of complex **18** is unlike complex **12**. Complex **18** packs into a linear chain and forms a ladder structure. The BPh_4^{-} ions situated between each complex running down the ladder is an apparent interference between each ladder structure. The spectrometric analysis by MS ESI+/- is presented below.

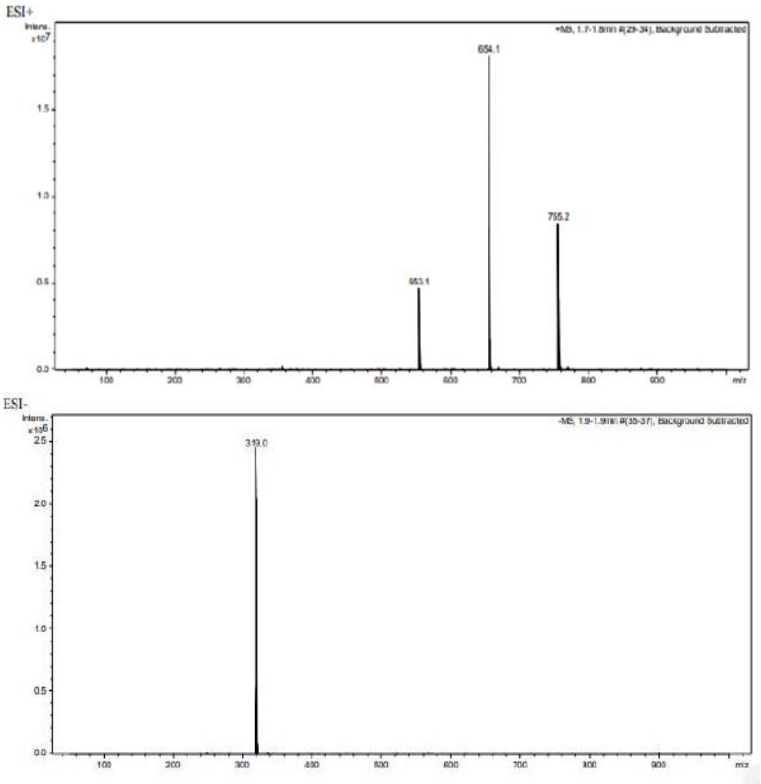

Figure 3.41: MS ESI+ of the $[(Qsal)Co(Qapl)]^+$ complex (top); ESI- of BPh_4^- (bottom).

The base peak of 654.1 *m/z* representing the heteroleptic $[(Qsal)Co(Qapl)]^+$ complex is accompanied by two other peaks representing the rearrangement to the homoleptic complexes $[Co(Qsal)_2]$ found at 553.1 *m/z* and $[Co(Qapl)_2]$ found at 755.2 *m/z* as anticipated. The presence of the BPh_4^- counter ion is noted at 319.0 *m/z*. Figure 3.42 below features the FT-IR spectrum of the complex **18**.

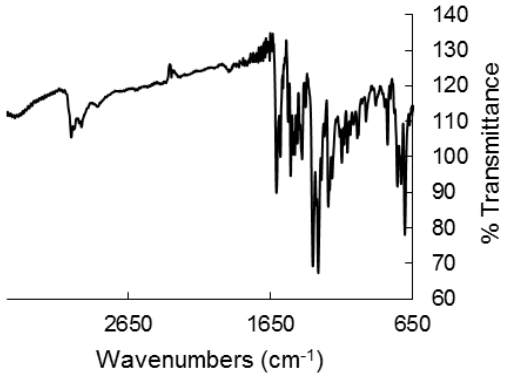

Figure 3.42: FT-IR spectroscopy in KBr of heteroleptic $[(Qsal)Co(Qapl)]^+BPh_4^-$ complex.

Aromatic C-H stretching is evident beyond 2650 cm^{-1}. The bending C-H resonances between 1604 cm^{-1} to 1430 cm^{-1} are attributed to both the conjugated ligands of the complex as well as the tetraphenylborate counter ion. C=N stretching from the ligands is visible between 1242 cm^{-1} and 1315 cm^{-1}.[20] No appearance of O-H or N-H resonances supports that the complex contains monoanionic Co-O coordinate bonds and N=N bonding. The experimental results obtained from combustion analysis of complex **18** are nearly identical (99%) with the calculated theoretical composition and match the values as $CoC_{63}H_{45}N_5O_2 \cdot 0.95Na^+CH_3COO^- \cdot 0.3CH_3OH$. These supporting data ensure that further investigations of magnetic and electrochemical properties were carried out with a pure form of the synthetic target.

3.8.2 Electrochemistry

The electronic spectroscopic data of complex **18** is overlaid with electronic absorption profiles of the Qsal and Qapl ligands in Figure 3.43. Crystals of complex **18** were analyzed while powder samples of the ligands were used. All experiments were conducted at RT. However, due to the solubility of each species, the solvent remains inconsistent as well as the relative concentrations.

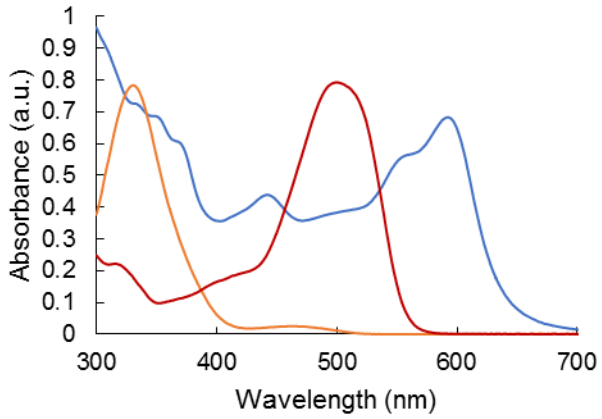

Figure 3.43: Electronic absorption profiles of $[(Qsal)Co(Qapl)]^+BPh_4^-$ in THF (blue trace), Qapl in DCM (red trace), Qsal (orange trace) in MeOH.

It is not unexpected to observe the intense absorbance of the Qapl ligand at 506 nm, lower in energy than Qsal, since the arylazo based ligand is much more conjugated. Complex **18** has a broad spectrum leading up to a lower energy absorption at around 600 nm. The low energy bands in the UV-vis presented here can be some LMCT of Co^{3+}.[33,34] The absorbance signals between 340-370 nm are speculated as some π-π* electronic transitions.

The electrochemical properties of $[(Qsal)Co(Qapl)]^{+}BPh_4^{-}$ presented below in Figure 3.44 show quite a different profile to that of the Fe^{3+} Qsal-RAL complexes.

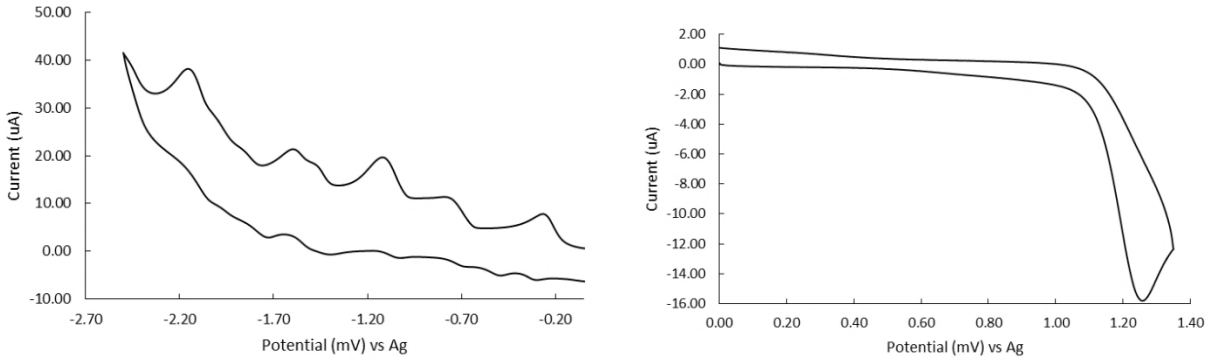

Figure 3.44: Cathodic trace (left) and anodic trace (right) of $[(Qsal)Co(Qapl)]^{+}BPh_4^{-}$ in DMF containing 0.5M $^{n}NBu_4PF_6$ supporting electrolyte.

$E_{1/2}$ Anodic vs Ag wire	$E_{1/2}$ Cathodic vs Ag wire
0.8 V (irr), 1.2 V (irr)	-0.3 V (qr), -1.0 V (irr), -1.5 V (irr), -2.1 V (irr)

A quasi-reversible process centered at -0.3 V is assigned to the $Co^{3+/2+}$ couple. A series of irreversible process are noted in the voltammogram of $[Co(Qapl)_2]^{+}Cl^{-}$ which can be assigned as ligand-centered oxidations involving the coordinated phenanthrol group.[19] The $E_{1/2}$ potentials of -1.5 V and -0.3 V in the cathodic trace here are consistent with the reported values pertaining to the azo bond of the coordinated Qapl ligand in the $[(Qsal)Fe(Qapl)]^{+}BPh_4^{-}$ and [(Cl-Qsal)Fe(Qapl)]$^{+}BPh_4^{-}$ complexes. The irreversible $E_{1/2}$ potentials of 0.8 V and 1.2 V in the

anodic trace of $[(Qsal)Co(Qapl)]^{+}BPh_4^{-}$ are comparable to 0.7 V and 1.2 V in $[(Cl\text{-}Qsal)Fe(Qapl)]^{+}BPh_4^{-}$ and 0.8 V and 1.3 V in $[(Qsal)Fe(Qapl)]^{+}BPh_4^{-}$ which is expected from the coordinated Qsal ligand.

3.9.0 Heteroleptic $[(Qsal)Co(Papl)]^{+}BPh_4^{-}$ Complex

In addition to Qapl, the ligand 1-(2-pyridylazo)-2-phenanthrol (Papl) was used to generate the heteroleptic $[(Qsal)Co(Papl)]^{+}BPh_4^{-}$ complex. Papl is synthesized by adding a solution of 2-hydrazinopyridine in glacial acetic acid, dropwise, to a hot solution of 9,10-phenanthrenequinone in glacial acetic acid. This mixture is then taken to reflux, neutralized with K_2CO_3, and the product is filtered off as an orange precipitate.[70,71] Its molecular structure is depicted below in Figure 3.45.

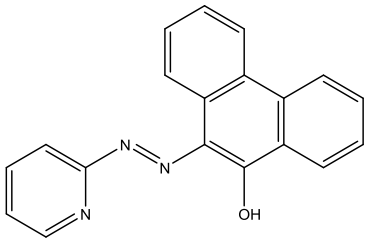

Figure 3.45: Molecular structure of the 1-(2-pyridylazo)-2-phenanthrol (Papl) ligand.

3.9.1 Synthesis and Structural Characterization

The Papl ligand was coordinated with [(Qsal)Co(OAc)] in an open atmosphere. The synthetic approach was identical to the one proven for the heteroleptic $[(Qsal)Co(Qapl)]^{+}BPh_4^{-}$ complex. Both the synthesis of complex **18** and **19** are among the shortest reaction times in contrast to the iron coordinations for forming the heteroleptic complexes.

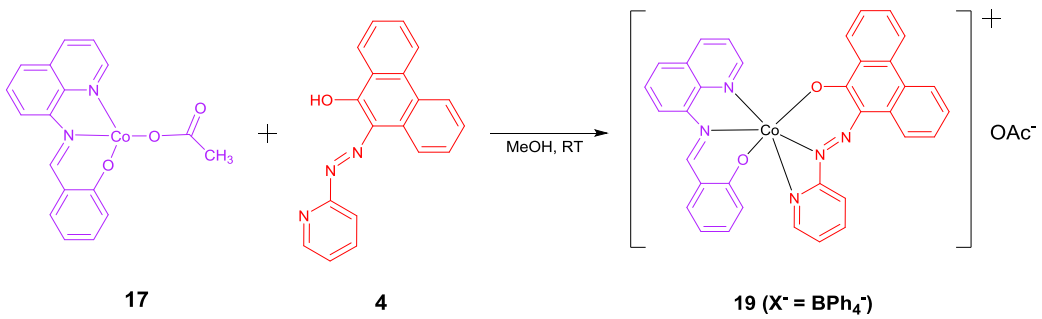

17 4 19 ($X^- = BPh_4^-$)

Scheme 3.9: Synthesis of $[(Qsal)Co(Papl)]^+OAc^-$

Recrystallization of complex **19** was accomplished through a DCM and pentane diffusion as inferred from literature by the crystallization of several homoleptic $[M(Papl)_2]^+$ complexes.[34] The structure of $[(Qsal)Co(Papl)]^+BPh_4^-$ is presented below in Figure 3.46.

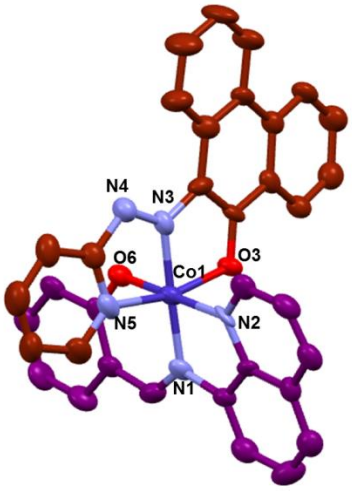

Figure 3.46: Molecular structure of the $[(Qsal)Co(Papl)]^+BPh_4^-$ complex. Hydrogen atoms and BPh_4^- counter ion omitted for clarity. Structure solved by the Pilkington group from brock University.

Table 3.6: Coordinate bond lengths of the $[(Qsal)Co(Papl)]^+BPh_4^-$ complex

Bond	Bond Length/Å
Co1-N1	1.914(9)
Co1-N2	1.937(5)
Co1-N3	1.856(8)
Co1-N5	1.933(9)
Co1-O1	1.919(9)
Co1-O2	1.871(5)
N3=N4	1.290(6)

The coordinate bond lengths of $[(Qsal)Co(Papl)]^{+}BPh_4^{-}$ infer a LS Co^{3+} center with all coordinate bonds being relatively short (< 2.0 Å). The N_2O donor atoms of Qsal correspond to the Co1-$N1_{imine}$ at 1.914 Å, the Co1-$N2_{quinoline}$ at 1.937 Å, and the deprotonated hydroxyl Co1-O2 at 1.871 Å. The coordinate bond lengths are typical of a Qsal anion and are consistent with other cobalt and iron heteroleptic Qsal complexes reported in this work. The Papl ligand shares the same set of donor atoms as Qapl with the exception that the azo coordinate bond comes from the N atom adjacent to the phenanthrol. The coordinate bonds of the $N_{pyridine}$ at 1.933 Å, the azo N at 1.856 Å, and the deprotonated hydroxyl at 1.919 Å are typical bond distances for a reported Papl anion.[34] The N=N bond distance of the azo moiety of 1.290 Å falls within the range of double bond character for a transition metal coordination complex.[33,34,65] The intermolecular interactions and how the complexes pack are shown in Figure 3.47 below.

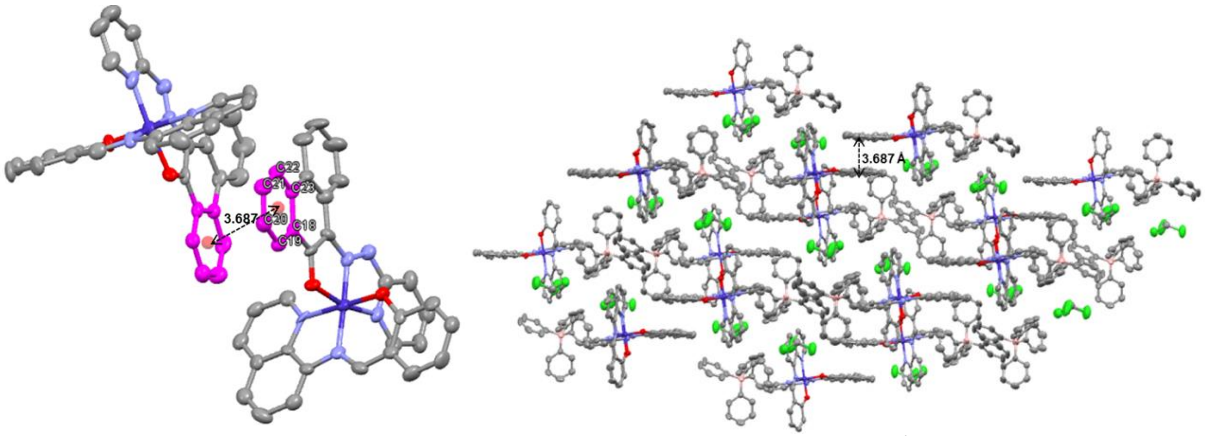

Figure 3.47: Intermolecular π-π overlap and packing of $[(Qsal)Co(Papl)]^{+}BPh_4^{-}$. Hydrogen atoms omitted for clarity

The only intermolecular π-π interaction noted occurs between the terminal ring of the phenanthrene moiety (C18-C23) on the Papl ligands. This π-π overlap closes a distance of 3.687 Å, comparable to complex **12** and **14** involving the Qapl ligand. The packing structure reveals an offset chain-like pattern held by the C18-C23 phenanthrene π-π overlap between adjacent complexes. The BPh_4^{-} ion appears to disrupt the propagation of further intermolecular contacts

along the chain as it rests in between the π-systems of the neighbouring Qsal and Papl ligands perpendicular to one another. This seems to be the case among all of the charged heteroleptic complexes that incorporate the bulkier counter ion which poses as a hindrance toward the complexes communicating with one another.

The corresponding homoleptic species appears with a mass charge ratio of 553.1 *m/z* for $[Co(Qsal)_2]^+$ and 655.1 *m/z* for $[Co(Papl)_2]^+$ in Mass Spectrometry (Appendix D.2).[90] The elemental analysis revealed a 5% discrepancy between the theoretically calculated and experimentally determined composition of complex **19** which was corrected by $0.6CHCl_3$ and $1.95H_2O$ molecules, likely from repeated washing and filtration of the target complex. Further characterization of the heteroleptic $[(Qsal)Co(Papl)]^+BPh_4^-$ complex by FT-IR spectroscopy is included in Appendix C.10.

3.9.2 Physicochemical and Electrochemical Properties

The electronic spectroscopic data comparing complex **19** with homoleptic $[Co(Qsal)_2]^+Cl^-$ at RT is presented below in Figure 3.48. A crystal sample of complex **19** was used in chloroform while a clean powder of $[Co(Qsal)_2]^+Cl^-$ was dissolved in THF due to their variance in solubility.

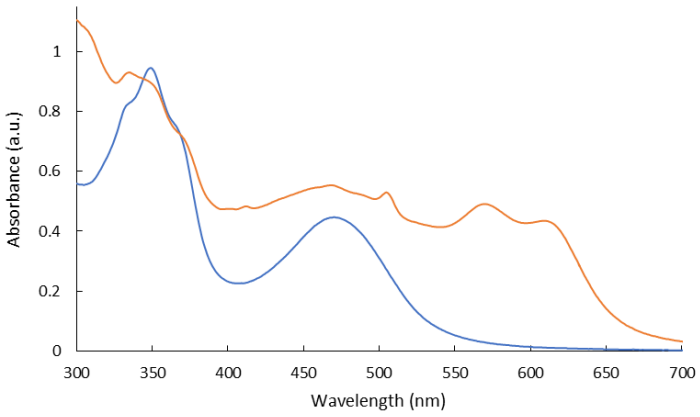

Figure 3.48: UV-vis spectra at RT for: $[(Qsal)Co(Papl)]^+BPH_4^-$ in $CHCl_3$ (orange trace); $[Co(Qsal)_2]^+Cl^-$ in THF (blue trace).

Uncoordinated Papl ligand exhibits a broad band with a high energy shoulder designated as the azo n-π* transitions (Appendix B.3). The broad feature of the $[(Qsal)Co(Papl)]^{+}BPh_4^{-}$ profile is distinct from the $[Co(Qsal)_2]^{+}Cl^{-}$ and complexes containing the Qapl ligand. Lower energy absorbance points at approximately 570 and 615 nm could indicate some LMCT character. Comparatively, a $[Ni(Papl)_2]$ complex reported in literature features two similarly broad bands accompanied by a higher energy shoulder at longer wavelengths which have been rationalized as ligand centered transitions of Papl in the presence of the metal cation, based on TD-DFT calculations.[34] Furthermore, several of these homoleptic $[M(Papl)_2]$ (M= Mn, Ni, Zn) complexes are capable of undergoing the multistep reduction process of the azo bond to generate the anionic radical on each ligand.[64] The short double bond distance reported for the $[(Qsal)Co(Papl)]^{+}BPh_4^{-}$ complex shows no elongation and therefore does not exist as a anionic radical. Reduction of both Qapl and Papl heteroleptic complexes were done in the glove box using sodium as the reducing agent. However, this reducing agent was excessive which resulted in degradation of the ligands. A strong one electron reducing agent such as cobaltocene would have to be investigated for the reduction of both Qapl and Papl to the anionic radical species.[74]

As stated earlier the [(Qsal)Co(OAc)] complex was determined as HS Co^{2+} which could potentially act as a strong one electron reducing agent. Activating the reduction process over the azo feature of the aryl-azo ligand could generate a neutral paramagnetic complex with a dianionic radical ligand. In comparison to Qapl, the Papl ligand alone exhibits an irreversible cathodic pathway suggestive of a less stable radical anionic form than Qapl.[34] However, electrochemical properties of the heteroleptic $[(Qsal)Co(Papl)]^{+}BPh_4^{-}$ complex could not be adequately measured with CV experiments due to the complex's poor solubility and its affinity for precipitating out of solution. Previous coordination attempts performed with exposure to air

produced charged Co^{3+} complexes. A neutral Co^{2+} complex would be expected to be paramagnetic for both HS and LS with *S*=3/2 and *S*=1/2, respectively. There is potential under inert atmosphere to produce Co^{2+} and possibly a phenoxyl radical species with redox-active valence tautomers.[36,83] This has been reported with cobalt-dioxolene complexes by a single electron transfer upon heating from a diamagnetic catecholate ligand coordinated to a LS Co^{3+} ion, producing a HS Co^{2+} ion, with a paramagnetic semiquinonate ligand.[83]

3.10.0 Alternative Ligand Systems

Given the synthetic nature of this research, other ligands were explored for heteroleptic coordinations. The ligand 4-(8-Quinolylazo)resorcinol (Qar) ligand was prepared analogous to Qan from a diazotization of 8-aminoquinoline with resorcinol as described in literature.[67] The structure of the Qar ligand is depicted below in Figure 3.49.

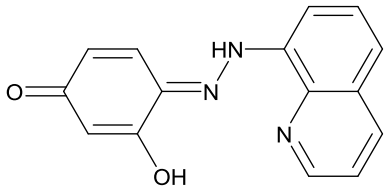

Figure 3.49: Structure of 4-(8-Quinolylazo)resorcinol (Qar) ligand.

In addition to the N_2O coordination site common among the ligands in this research, Qar also offered a quinone-like feature that was thought to give rise to interesting electronic properties and redox-activity. Coordination of Qar with iron or cobalt carried out in a similar manner discussed in Sections 3.2, 3.6, 3.8, and 3.9 were observed to be inconsistent with both heteroleptic and homoleptic formation and rationalized based on the possible reduction of the quinone in the Qar ligand.

Chapter 4.0 Conclusions and Perspectives

Working through the synthetic strategies for generating heteroleptic mononuclear redox-active complexes with the potential for SCO and conductivity, united within a single component, has provided greater insight regarding their coordination chemistry and factors that appear to significantly impact their cooperativity. Most of these coordination reactions presented complications regarding the formation of homoleptic complexes and the solubility and purity of the heteroleptic complexes. Working primarily with iron and cobalt we have established a means of coordinating the metal ion with Qsal in the form of $[(Qsal)FeCl_2(CH_3OH)]$ and $[(Qsal)Co(OAc)]^+OAc^-$ to various arylazo redox-active ligands, leading to complexes in the form of $[(Qsal)Fe(RAL)]^+X^-$ and $[(Qsal)Co(RAL)]^+X^-$, respectively. Complexes that could not be crystallized for X-ray diffraction relied heavily on other supporting data like UV-vis, FT-IR, and combustion analysis to provide evidence of their formation and purity. A major impact over the intermolecular forces and cooperativity among the complexes appears to be the bulk of the counter ion as noted from the packing structures of complex **12**, **14**, **18**, and **19**. In particular, complex **12** and **13**, despite remaining LS Fe^{3+}, show some early onset of spin transition at RT. Solution based analyses by VT UV-vis do indicate multiple components in solution at specific wavelengths. However, this behaviour was not observed with halogenated Qsal complexes. Despite offering greater π-π overlaps in the Fe1B molecule of complex **14**, the magnetic susceptibility in both the solid state and solution did not reflect this compared to complex **12**.

Based on the effects of the BPh_4^- ion over the identified intermolecular interactions and packing structures of complexes **12**, **14**, **18**, **19** and $[Fe(Qapl)_2]^+BPh_4^-$ it would be ideal to purify and investigate these complexes with smaller counter ions or counter ions that do not contain arene groups. Deviating from counter ions like BPh_4^- may also help the complex to act less like

an insulator.[42] The electrochemical profiles of the complexes containing the Qapl ligand show a quasi-reversible low reduction potential. This characteristic could render these complexes as candidates for a one-electron reduction process. Chemical reduction of either the azo bond of the arylazo ligands or the Fe^{3+}/Co^{3+} centers using milder reductant like sodium naphthalide or cobaltocene would be rational to examine. Reducing the metal centers from M^{3+} to M^{2+} could introduce thermally reversible intramolecular electron transfers that could reduce the redox-active ligands.[32,83] Exploration with other types of ligands helps to constantly expand the field of coordination chemistry. One prospective ligand that was briefly examined known as 2,4-di-tert-butyl-6-(pyridin-2-ylazo)phenol (HL) and its coordination pathway is proposed below in Scheme 4.0.

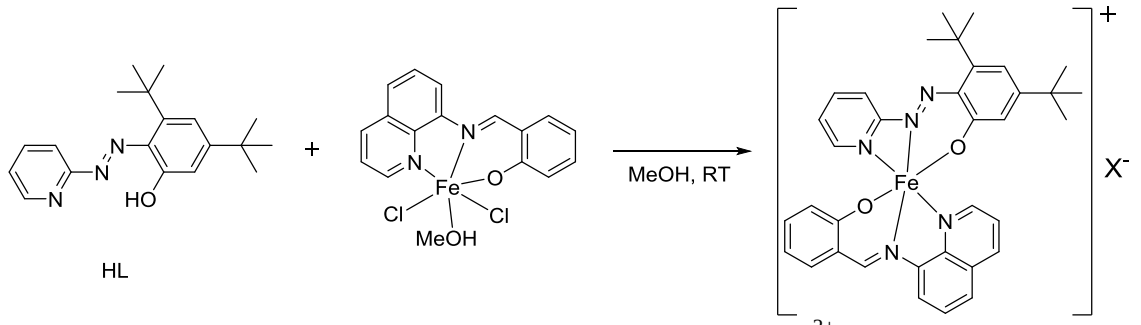

Scheme 4.0: Proposed synthetic target based on heteroleptic Fe^{3+} coordination reactions.

The feature of the *t*-butyl groups or other alkyl substituents were not explored but could be of interest for altering different properties of the complex like solubility or radical stabilization. The $[(Qsal)FeCl_2(CH_3OH)]$ complex was also investigated for its use as a capping agent in attempts to engineer bimetallic complexes with the intent of producing a system that would exhibit multi-state switching capabilities. This idea was investigated with a previously synthesized ligand known as bis(4,6-di-tert-butylphenol)-bis(4,6-diazenyl)pyrimidine, illustrated below in Figure 4.0, including the proposed bimetallic complex.

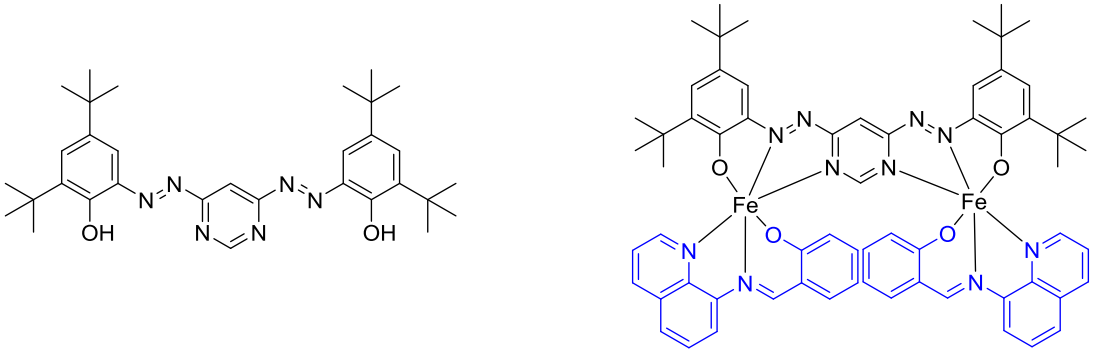

Figure 4.0: Proposed bimetallic Fe(Qsal) system with bis(4,6-di-tert-butylphenol)-bis(4,6-diazenyl)pyrimidine.

The coordination reaction in a 2:1 ratio with [(Qsal)$FeCl_2(CH_3OH)$] inadvertently gave rise to some [2x2] grid system. Although the sample was collected with numerous by-products, there is some indication of a di-protic [2x2] iron grid system identified at 2394.2 *m/z* in the MS ESI+ spectrum. Subsequent coordination reactions with $FeCl_3$ resulted in a tetra-radical grid species. Crystallization and purification of the iron grids through diffusion or slow evaporation has so far been unsuccessful. These initial findings temporarily suspended the investigation of bimetallic and [2x2] grid systems.

The aspirations of this research are to provide a stepping-stone concerning the synthetic strategies toward heteroleptic redox-active complexes and to provide insight for improving potential SCO and conductivity properties of these types of heteroleptic complexes for the significance of multifunctional materials.

APPENDICES

Appendix A: $^{1}H/^{13}C$-NMR Spectra

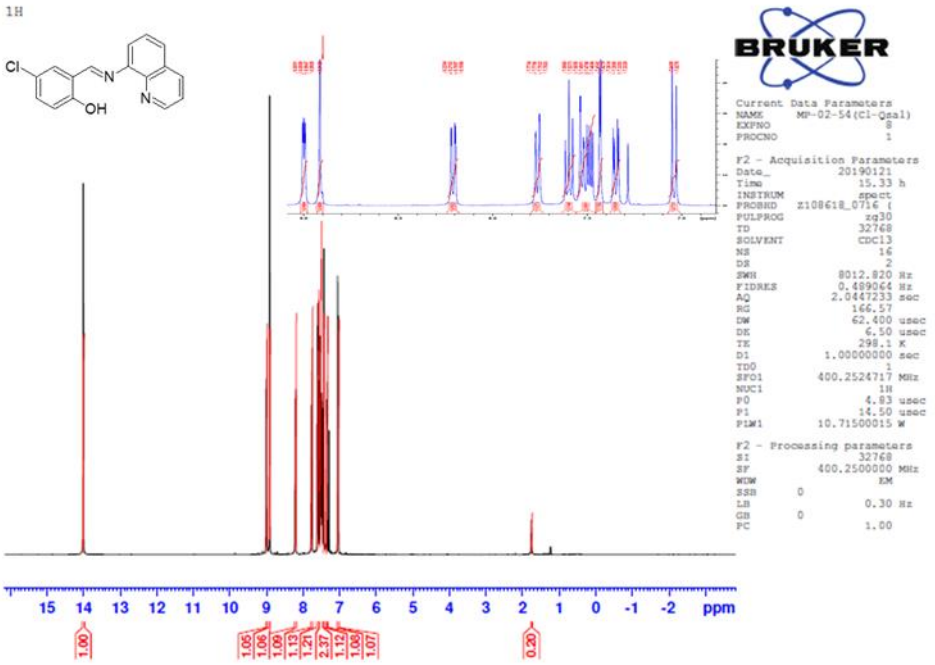

Figure A.1: ^{1}H-NMR Cl-Qsal in $CDCl_3$

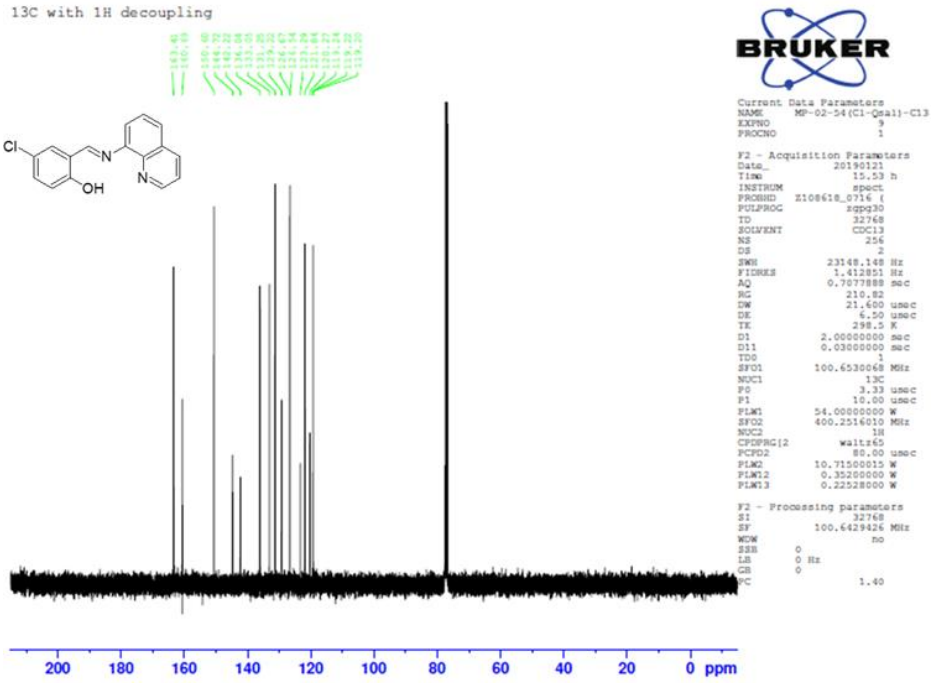

Figure A.2: ^{13}C-NMR Cl-Qsal in $CDCl_3$

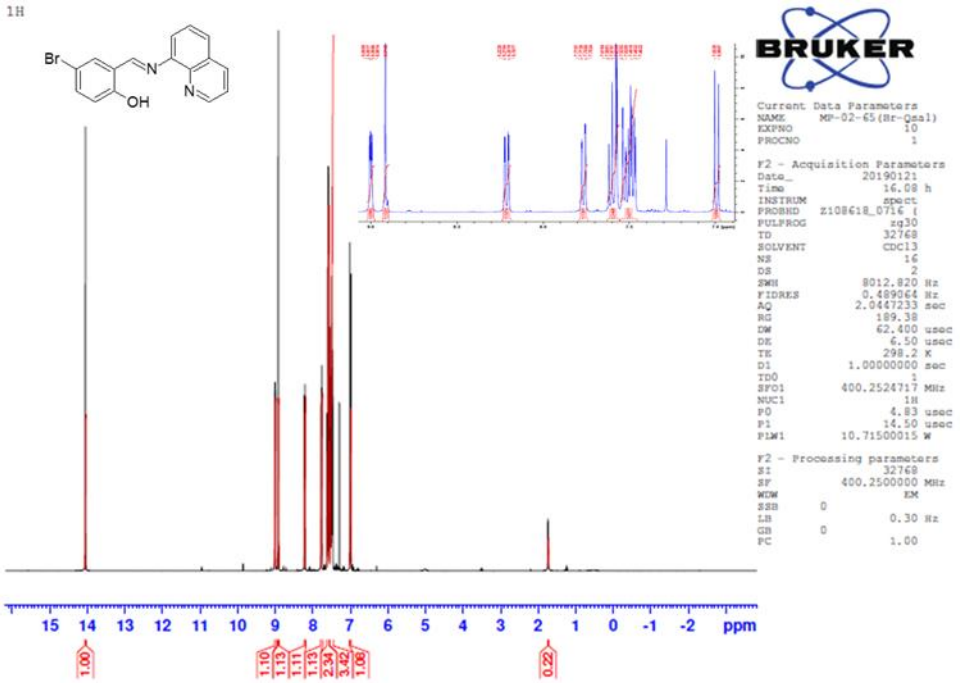

Figure A.3: ^{1}H-NMR Br-Qsal in $CDCl_3$

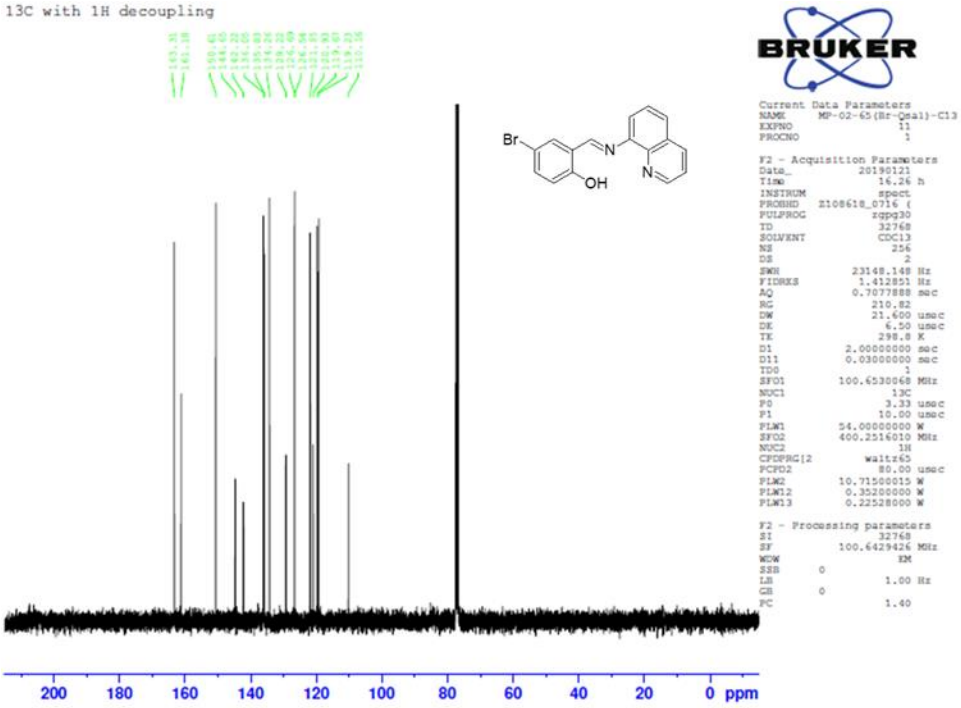

Figure A.4: ^{13}C-NMR Br-Qsal in $CDCl_3$

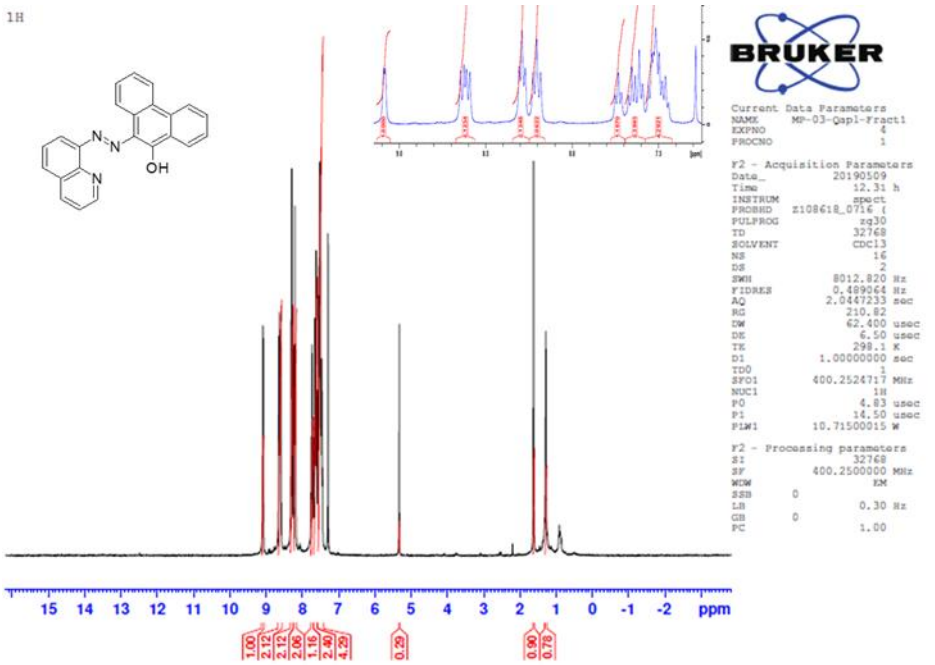

Figure A.5: ^{1}H-NMR Qapl in $CDCl_3$

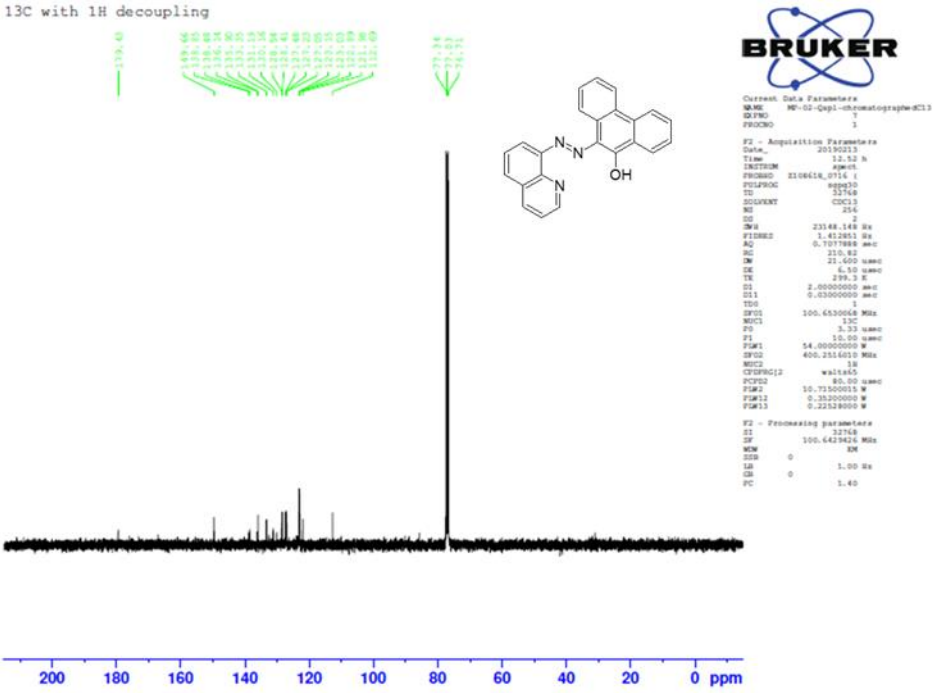

Figure A.6: ^{13}C-NMR Qapl in $CDCl_3$

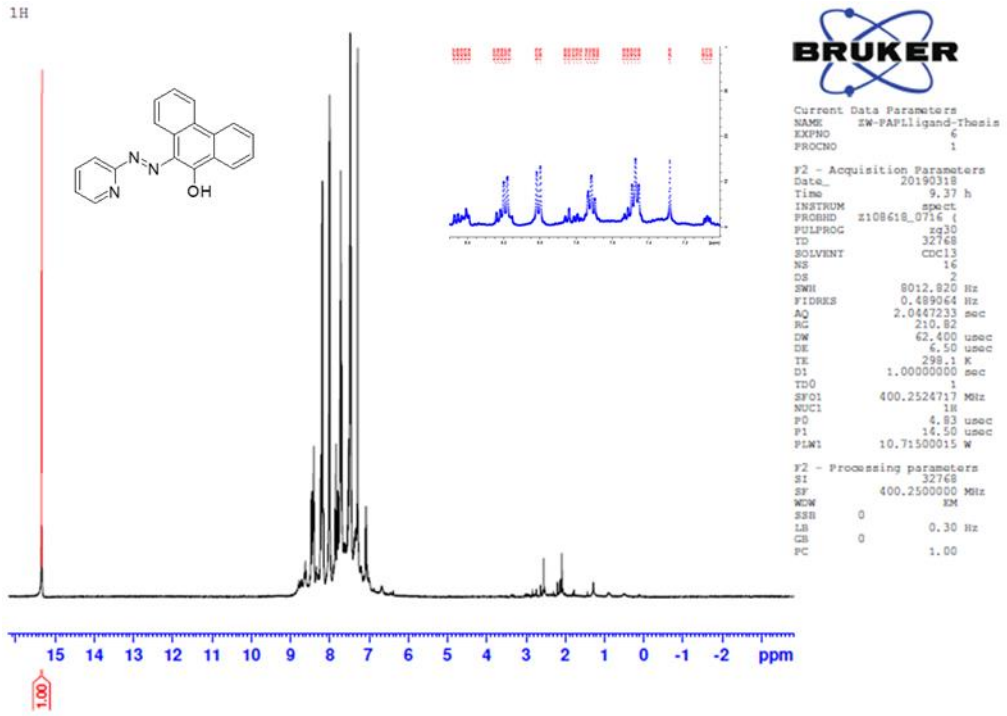

Figure A.7: ^{1}H-NMR Papl in $CDCl_3$

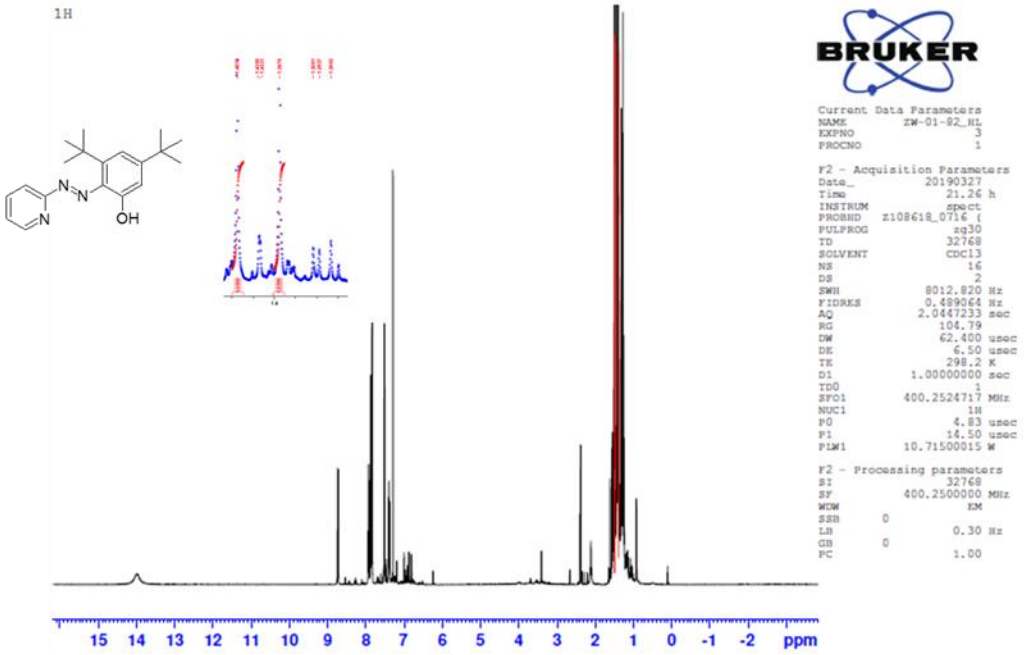

Figure A.8: ^{1}H-NMR HL in $CDCl_3$

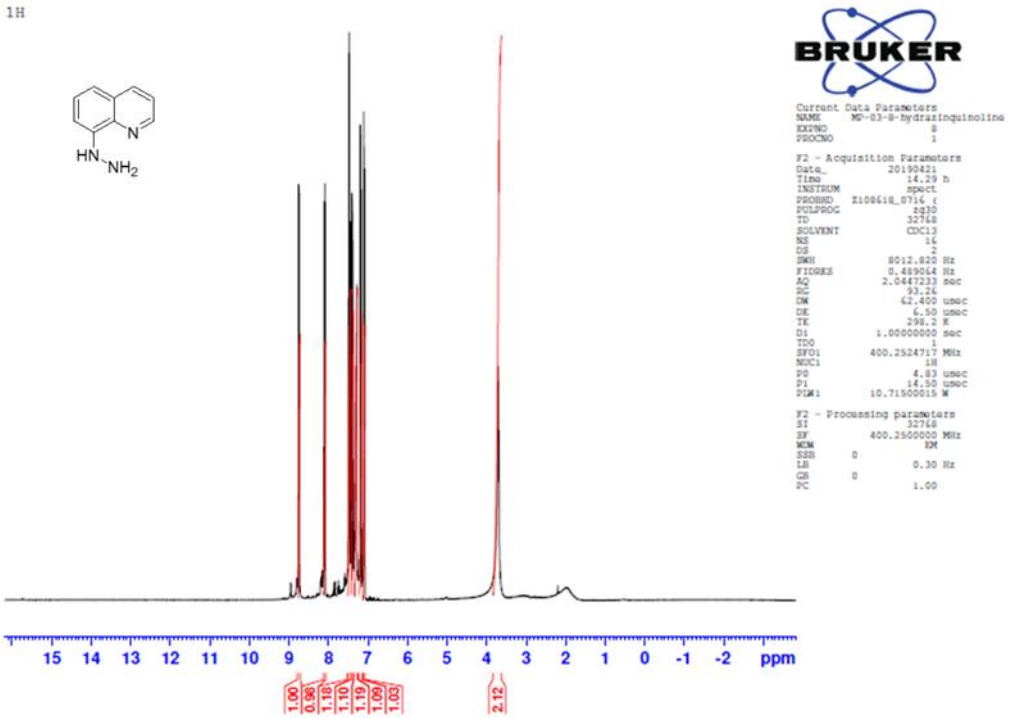

Figure A.9: ^{1}H-NMR 8-hydrazinoquinoline in $CDCl_3$

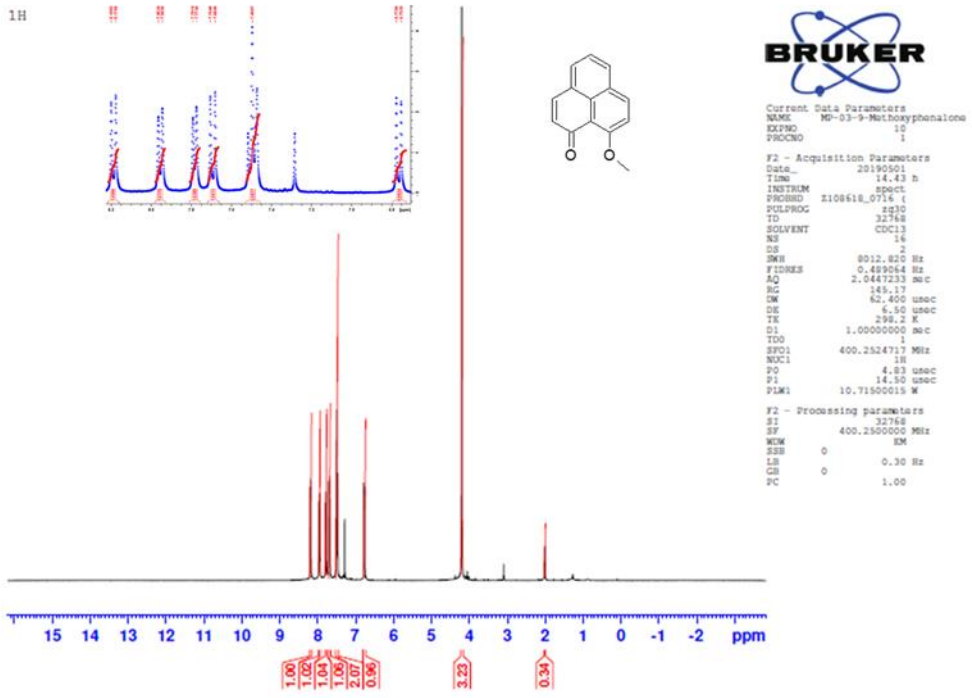

Figure A.10: ^{1}H-NMR 9-methoxyphenalenone in $CDCl_3$

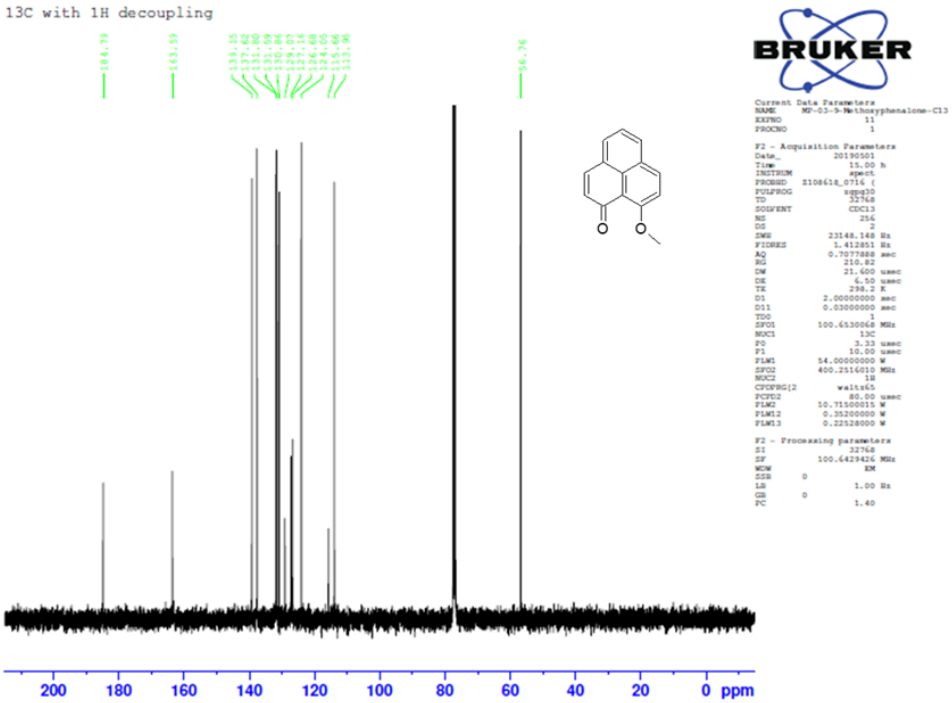

Figure A.11: ^{13}C-NMR 9-methoxyphenalenone in $CDCl_3$

Appendix B: UV-visible Spectra

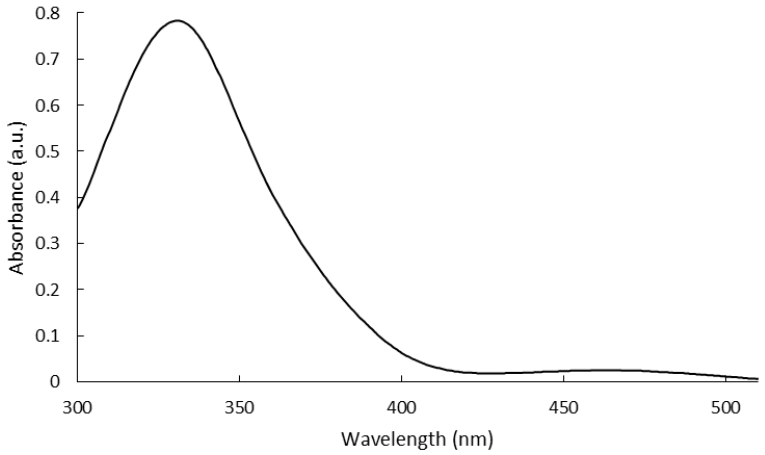

Figure B.1: UV-vis data for Qsal ligand in DCM at RT: λ_{max}: 331 nm

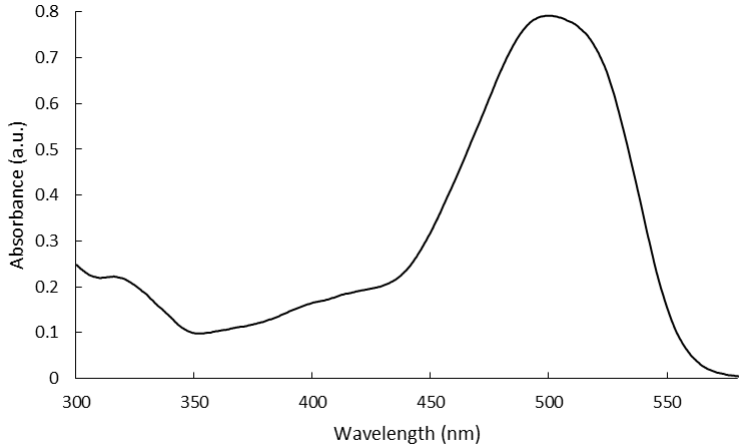

Figure B.2: UV-vis data for Qapl ligand in DCM at RT: λ_{max}: 493 nm

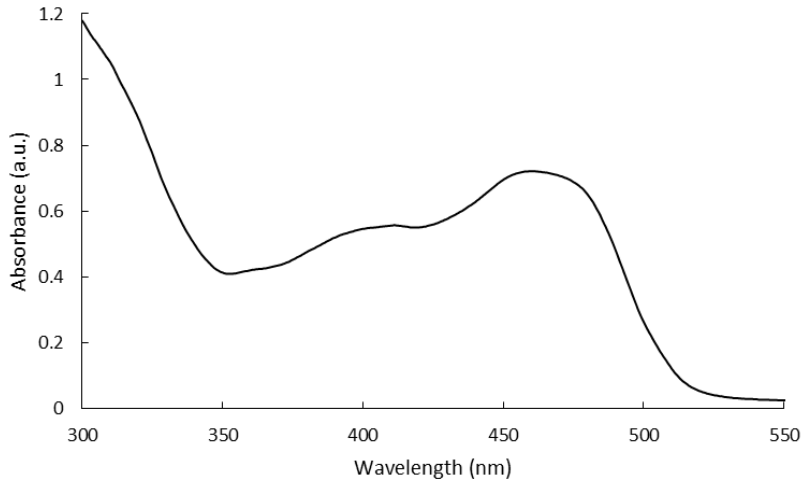

Figure B.3: UV-vis data for Papl ligand in DCM at RT: λ_{max}: 460 nm

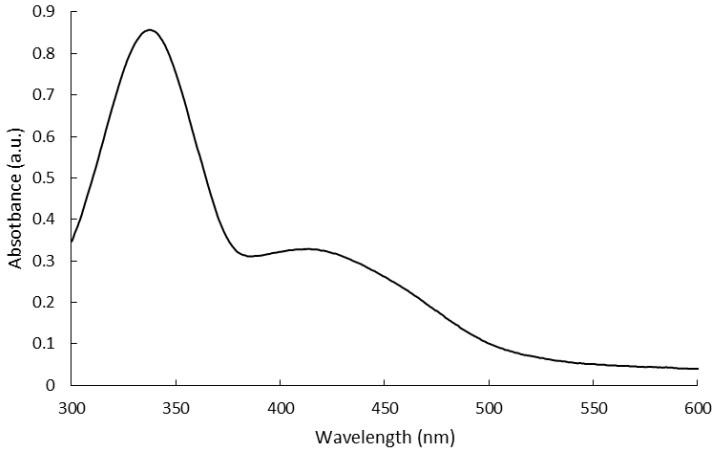

Figure B.4: UV-vis data for HL ligand in THF at RT: λ_{max}: 340 nm

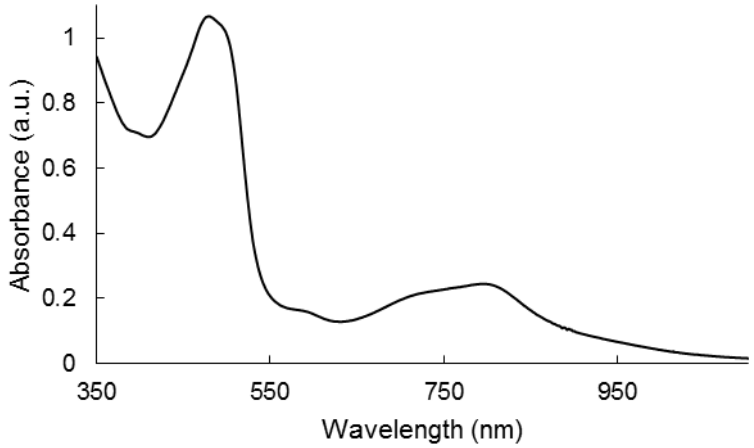

Figure B.5: UV-vis data for Qan ligand in DCM at RT; λ_{max}: 470 nm

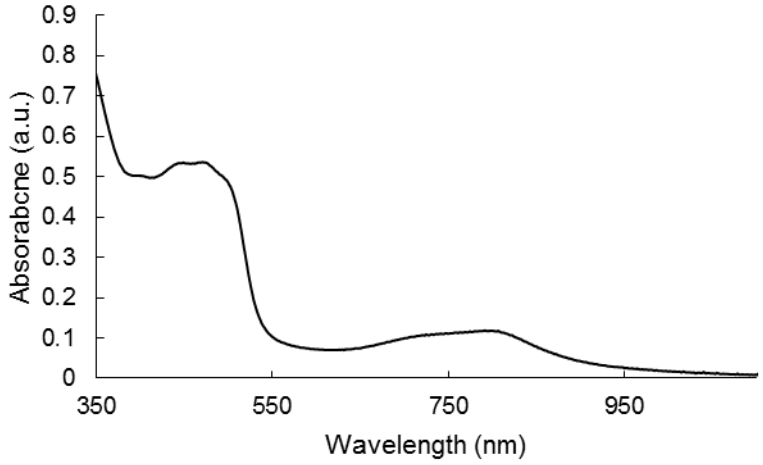

Figure B.6: UV-vis data for $[Fe(Qan)_2]$ at RT in THF; λ_{max}: 459 nm

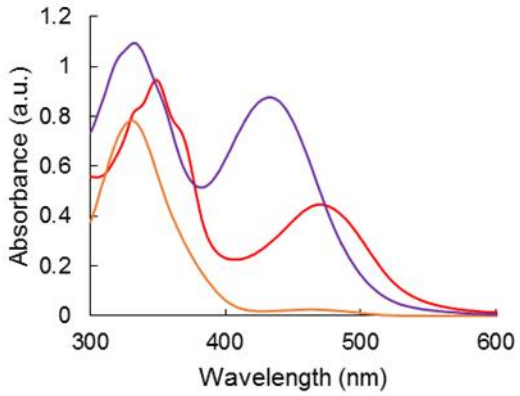

Figure B.7: UV-vis spectra at RT for: [(Qsal)Co(OAc)] (purple trace); [Co(Qsal)$_2$] (red trace); Qsal (orange trace) in methanol. The blue shift from 348 nm to 334 nm between the cobalt complexes points to two separate species. The absorbance at 436 nm of the [(Qsal)Co(OAc)] complex may suggest some MLCT from the metal's *d*-orbital to a ligand centered orbital.

Appendix C: FT-IR Spectra

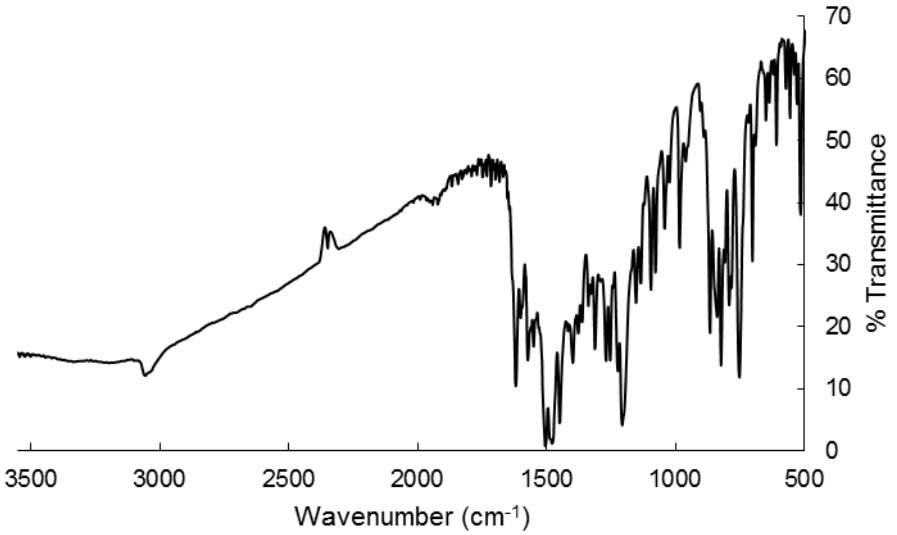

Figure C.1: FT-IR (KBr, cm^{-1}) Qan ligand

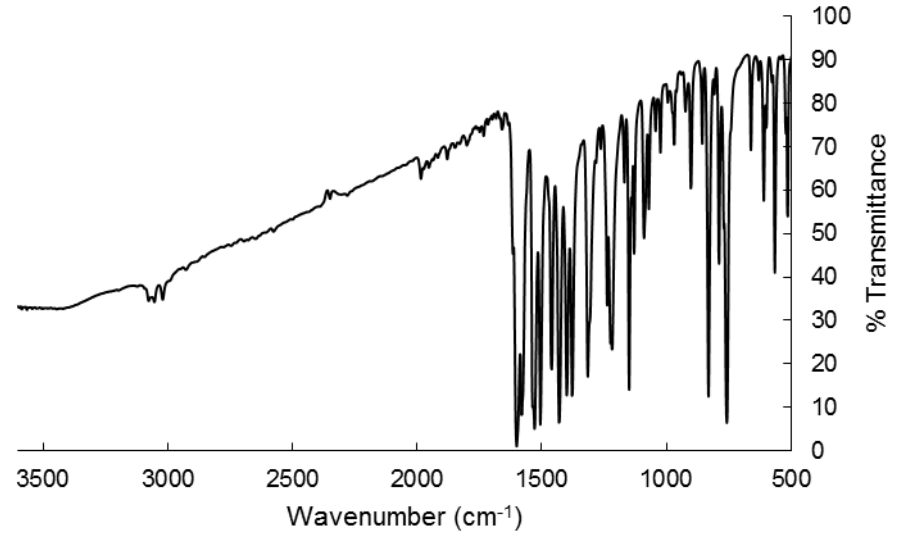

Figure C.2: FT-IR (KBr, cm^{-1}) [(Qsal)$FeCl_2(CH_3OH)$] complex

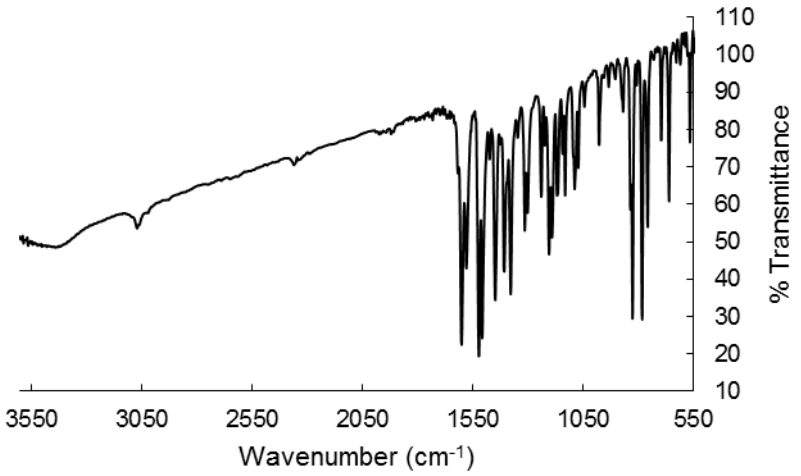

Figure C.3: FT-IR (KBr, cm^{-1}) [(Cl-Qsal)$FeCl_2(CH_3OH)$] complex

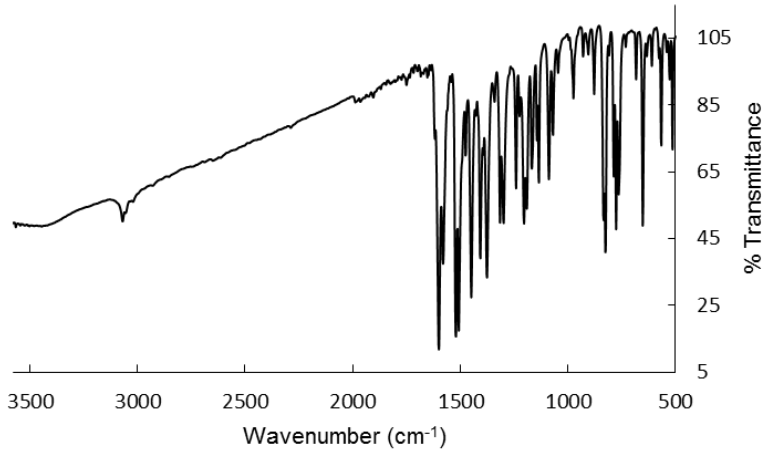

Figure C.4: FT-IR (KBr, cm^{-1}) [(Br-Qsal)$FeCl_2(CH_3OH)$] complex

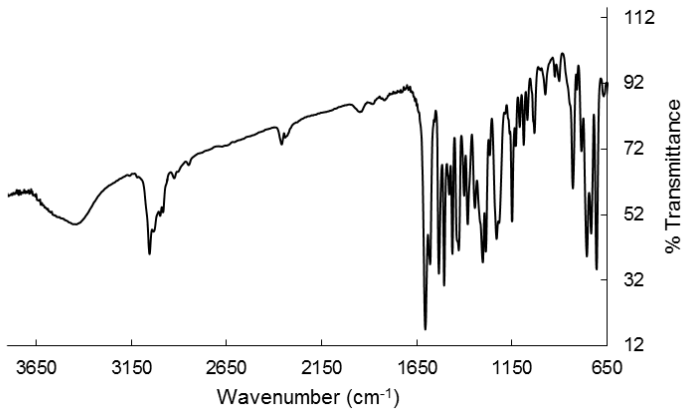

Figure C.5: FT-IR (KBr, cm^{-1}) Heteroleptic $[(Qsal)Fe(Qapl)]^{+}BPh_4^{-}$ complex

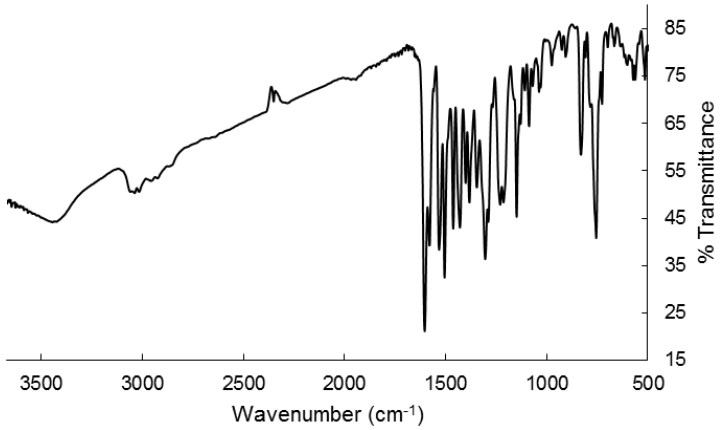

Figure C.6: FT-IR (KBr, cm^{-1}) Heteroleptic $[(Qsal)Fe(Qapl)]^{+}I^{-}$ complex

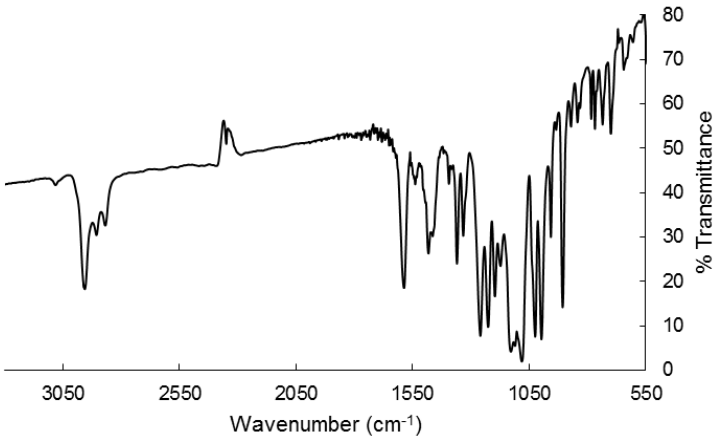

Figure C.7: FT-IR (KBr, cm^{-1}) Di-protic Fe[2x2] grid system

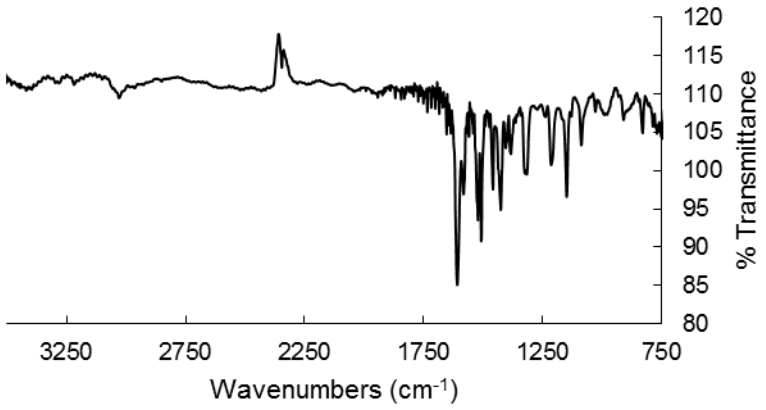

Figure C.8: FT-IR (KBr, cm^{-1}) Homoleptic $[Co(Qsal)_2]^+Cl^-$ complex

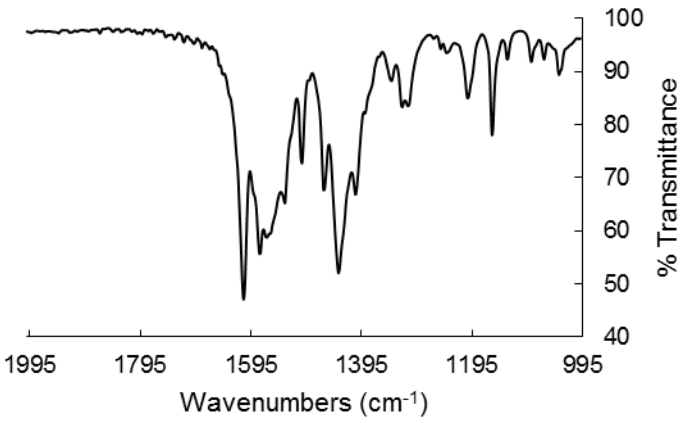

Figure C.9: FT-IR in KBr of $[(Qsal)Co(OAc)]^{+}OAc^{-}$ complex. The C=O stretching observed at 1608 cm^{-1} is characteristic of an acetate species. The stretching seen at 1558 cm^{-1} is likely to be C=N stretching. The lack of an O-H signal indicates that the oxygen donor atom of Qsal is fully associated with the cobalt.

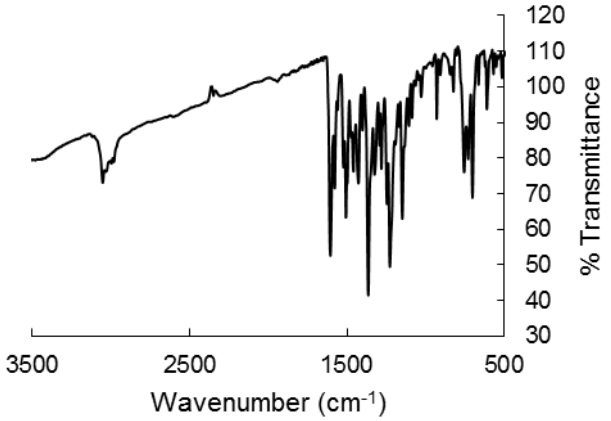

Figure C.10: FT-IR in KBr of heteroleptic $[(Qsal)Co(Papl)]^{+}BPh_4^{-}$ complex. Stretching at 1606 cm^{-1} is characteristic of C=N bonding in Qsal similar to that of the [(Qsal)Co(OAc)]. Weaker stretching appearing at 1149 cm^{-1} likely corresponds to the coordinated azo N=N feature of Papl.[34] Most aromatic C=C stretching covers the range between 1506-1402 cm^{-1}. The 1365 cm^{-1} and 1228 cm^{-1} stretches, in addition to no O-H signal present, are suggestive of aromatic C-O stretching of the deprotonated hydroxyls on each ligand.

Appendix D: Mass Spectrometry

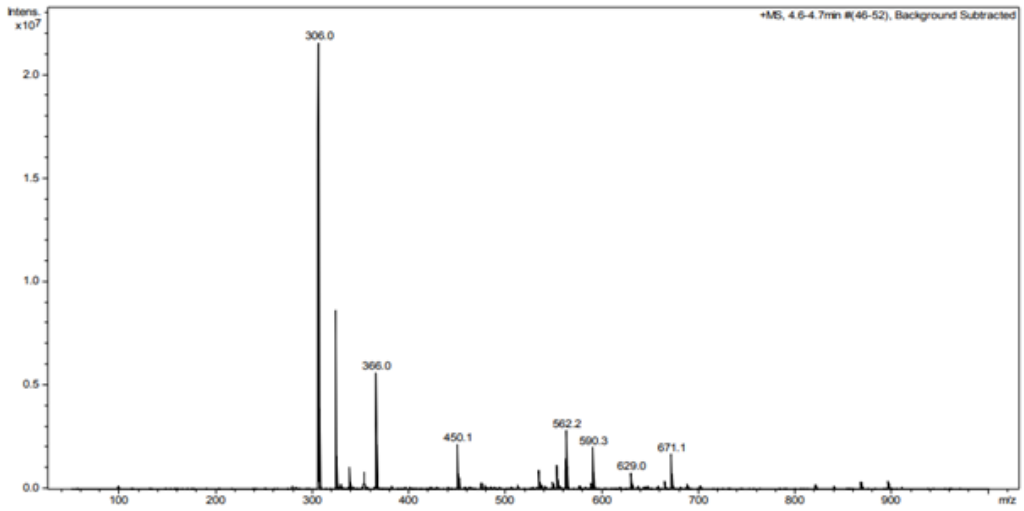

Figure D.1: MS ESI+ of $[(Qsal)Co(OAc)]^{+}OAc^{-}$

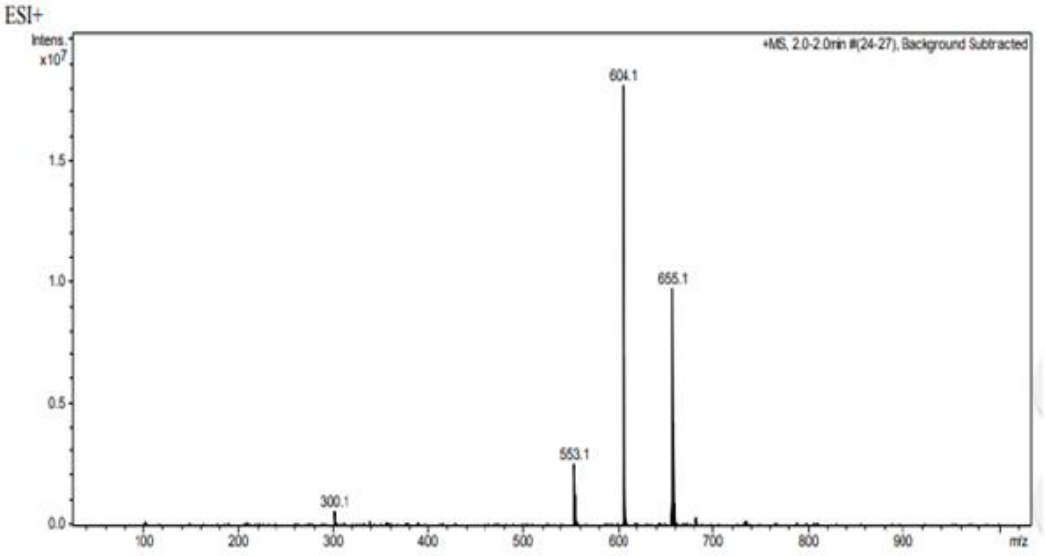

Figure D.2: MS ESI+ of the $[(Qsal)Co(Papl)]^{+}$ complex. Base peak at 604.1 *m/z* is in accordance with the mass of the heteroleptic Co complex.

Appendix E: Crystallographic Parameters

Table E.1: Crystal data and structure refinement for $[(Qsal)Fe(Qapl)]^{+}BPh_4^{-}$ THF

Crystal Data. $C_{67}H_{53}BFeN_5O_3$, M_r = 1042.80, monoclinic, $P2_1/c$ (No. 14), a = 10.3394(4) Å, b = 19.9119(7) Å, c = 25.3920(8) Å, α = 95.2350(10)°, $\beta = \gamma$ = 90°, V = 5205.8(3) Å^3, T = 90(2) K, Z = 4, Z' = 1, μ(MoK$_\alpha$) = 0.345 mm^{-1}, 69707 reflections measured, 15933 unique (R_{int} = 0.0560) which were used in all calculations. The final wR_2 was 0.1150 (all data) and R_1 was 0.0468 (I > 2(I)).

Formula	$C_{67}H_{53}BFeN_5O_3$
Formula Weight	1042.80
Colour	black
Shape	tablet
Size/mm^3	0.27×0.17×0.07
T/K	90(2)
Crystal System	monoclinic
Space Group	$P2_1/c$
a/Å	10.3394(4)
b/Å	19.9119(7)
c/Å	25.3920(8)
α/°	90
β/°	95.2350(10)
γ/°	90
V/Å^3	5205.8(3)
Z	4
Z'	1
Measured Refl.	69707
Independent Refl.	15933
Reflections Used	11409
R_{int}	0.0560
Parameters	694
Restraints	0
Largest Peak	0.855
Deepest Hole	-0.623
GooF	1.014
wR_2 (all data)	0.1150
wR_2	0.1019
R_1 (all data)	0.0781
R_1	0.0468

Table E.2: Crystal data and structure refinement for $[(Cl\text{-}Qsal)Fe(Qapl)]^{+}BPh_4^{-}1.5THF$

Empirical formula	C68.80 H55.60 B Cl Fe N5 O3.45	
Formula weight	1109.72	
Temperature	150(2) K	
Crystal system	Triclinic	
Space group	P-1	
Unit cell dimensions	a = 10.0971(4) Å	
	b = 21.3818(8) Å	
	c = 26.8130(10) Å	a= 102.499(2)°.
Volume	5485.1(4) Å3	b= 90.372(2)°.
Z	4	g = 103.517(2)°.
Density (calculated)	1.344 Mg/m3	
Absorption coefficient	3.093 mm-1	
F(000)	2316	
Crystal size	0.340 x 0.340 x 0.060 mm3	
Theta range for data collection	1.691 to 67.792°.	
Index ranges	-12<=h<=12, -25<=k<=25, -31<=l<=32	
Reflections collected	125268	
Independent reflections	19636 [R(int) = 0.0524]	
Completeness to theta = 67.679°	98.90%	
Absorption correction	Semi-empirical from equivalents	
Max. and min. transmission	0.7530 and 0.6060	
Refinement method	Full-matrix least-squares on F2	
Data / restraints / parameters	19636 / 12 / 1451	
Goodness-of-fit on F2	1.017	
Final R indices [I>2sigma(I)]	R1 = 0.0461, wR2 = 0.1214	
R indices (all data)	R1 = 0.0545, wR2 = 0.1284	
Extinction coefficient	n/a	
Largest diff. peak and hole	0.788 and -0.435 e.Å-3	

Table E.3: Crystal data and structure refinement for $[Fe(Qapl)_2]^+BPh_4^-$

Empirical formula	C78 H64 B Fe N6 O4	
Formula weight	1216.01	
Temperature	150(2) K	
Wavelength	1.54178 Å	
Crystal system	Monoclinic	
Space group	$P2_1/n$	
Unit cell dimensions	a = 11.7529(4) Å	
	b = 34.0695(12) Å	a= 90°.
	c = 15.9736(6) Å	b= 108.783(2)°.
Volume	6055.5(4) Å3	g = 90°.
Z	4	
Density (calculated)	1.334 Mg/m3	
Absorption coefficient	2.467 mm-1	
F(000)	2548	
Crystal size	0.130 x 0.120 x 0.120 mm3	
Theta range for data collection	2.594 to 67.658°.	
Index ranges	-14<=h<=14, -40<=k<=40, -19<=l<=19	
Reflections collected	134857	
Independent reflections	10907 [R(int) = 0.0576]	
Completeness to theta = 67.658°	99.70%	
Absorption correction	Semi-empirical from equivalents	
Max. and min. transmission	0.7530 and 0.6584	
Refinement method	Full-matrix least-squares on F2	
Data / restraints / parameters	10907 / 10 / 811	
Goodness-of-fit on F2	1.068	
Final R indices [I>2sigma(I)]	R1 = 0.0431, wR2 = 0.1130	
R indices (all data)	R1 = 0.0473, wR2 = 0.1161	
Extinction coefficient	n/a	
Largest diff. peak and hole	0.741 and -0.891 e.Å-3	

Table E.4: Crystal data and structure refinement for $[Fe(Qan)_2]$

Crystal Data. $C_{39}H_{26}Cl_2FeN_6O_2$, M_r = 737.41, triclinic, P-1 (No. 2), a = 11.363(3) Å, b = 12.370(3) Å, c = 13.056(4) Å, α = 112.882(7)°, β = 110.728(6)°, γ = 92.939(7)°, V = 1542.7(7) Å^3, T = 100(2) K, Z = 2, Z' = 1, $\mu(MoK_\alpha)$ = 0.712 mm^{-1}, 19782 reflections measured, 5669 unique (R_{int} = 0.0933) which were used in all calculations. The final wR_2 was 0.1461 (all data) and R_1 was 0.0555 (I > 2(I)).

Formula	$C_{39}H_{26}Cl_2FeN_6O_2$
$D_{calc.}$/ g cm^{-3}	1.587
μ/mm^{-1}	0.712
Formula Weight	737.41
Colour	black
Shape	needle
Size/mm^3	0.22×0.03×0.02
T/K	100(2)
Crystal System	triclinic
Space Group	P-1
a/Å	11.363(3)
b/Å	12.370(3)
c/Å	13.056(4)
α/°	112.882(7)
β/°	110.728(6)
γ/°	92.939(7)
V/Å^3	1542.7(7)
Z	2
Z'	1
Measured Refl.	19782
Independent Refl.	5669
Reflections Used	3701
R_{int}	0.0933
Parameters	451
Restraints	1
Largest Peak	0.921
Deepest Hole	-0.579
GooF	1.023
wR_2 (all data)	0.1461
wR_2	0.1245
R_1 (all data)	0.0991
R_1	0.0555

REFERENCES

1. Housecroft, C.E.; Sharpe, A.G. (2012). *Inorganic Chemistry, 4th Ed*. Harlow, England: Pearson Education Ltd.

2. Benelli, C.; Gatteschi, D. (2015). *Introduction to Molecular Magnetism From Transition Metals to Lanthanides.* Weinheim, Germany: Wiley-VCH Verlag GmbH & Co.

3. Miller, J.S.; Drillon, M. (2002). *Magnetism: Molecules to Materials IV*. Electronic: Wiley-VCH Verlag GmbH & Co.

4. Kahn, O. (1993). *Molecular Magnetism*. New York N.Y., United States: VCH Publishers Inc.

5. Halcrow, M.A. (2013). *Spin-crossover Materials, Properties and Applications*. Chichester, United Kingdom: John Wiley & Sons Ltd.

6. Nemec, I.; Herchel, R.; Trávníček, Z. *Dalton Trans*., **2015**, 44, 4474-4484.

7. Harding, D.J.; Harding, P.; Phonsri, W. *Coord. Chem. Rev.*, **2016**, 313, 38-61.

8. Real, J.A.; Gaspar, A.B.; Muñoz, C.M. *Dalton Trans*., **2005**, 2062-2079.

9. Parkin, G. *J. Chem. Edu*., **2006**, 83(5), 791-799.

10. Dickinson, R.C.; Baker, W.A. *J. Inorg. Nucl. Chem.*, **1976**, 1531-1533.

11. Dahl, B.M.; Dahl, O. *Acta Chem. Scand*., **1969**, 23, 1503.

12. Kauffman, G.B. *Spectrum*, **1987**, 25(4), 5-14.

13. Li, G.; Sato, O. *Acta Cryst.* **2017**, E73, 993-995.

14. Barrios, L.A.; Bartual-Murgui, C.; Peyrecave-Lleixà, E.; Guennic, B.; Teat, S.J.; Roubeau, O.; Aromí, G. *Inorg. Chem*., **2016**, 55, 4110-4116.

15. Yergeshbayeva, S.; Hrudka, J.J.; Lengyel, J.; Erkasov, R.; Stoian, S.A.; Dragulescu-Andrasi, A.; Shatruk, M. *Inorg. Chem*., **2017**, 56, 11096-11103.

16. Kawamura, Y.; Tsukahara, Y.; Nasu, S.; Morimoto, S.; Fuyuhiro, A.; Kaizaki, S. *Inorg. Chim. Acta.*, **2004**, 357, 2437-2440.

17. Lord, R.L.; Schultz, F.A.; Baik, M. *J. Am. Chem. Soc*., **2009**, 131, 6189-6197.

18. Evangelio, E.; Ruiz-Molina, D. *C. R. Chimie*, **2008**, 11, 1137-1154.

19. Himmel, H. *Inorg. Chim. Acta*, **2018**, 481, 56-68.

20. Silverstein, R.M.; Webster, F.X.; Kiemle, D.J. (2005). *Spectrometric Identification of Organic Compounds, 7th Ed.*, New York, United States: John Wiley & Sons Inc.

21. Johnson, A.R. (2016). *The Evans Method*. California, United States: VIPEr.

22. Phan, H.; Herng, T.S.; Wang, D.; Li, X.; Zeng, W.; Ding, J.; Loh, K.P.; Wee, A.; Wu, J. *Chem*., **2019**, 5, 1-12.

23. Phonsri, W.; Macedo, D.S.; Davies, C.G.; Jameson, G.N.L.; Moubaraki, B.; Murray, K.S. *Dalton Trans.*, **2017**, 46, 7020-7029.

24. Drahoš, B.; Šalitroš, I.; Herchel, R. *Inorg. Chim. Acta*, **2019**, 495, 118921-118927.

25. Kumar, K.S.; Ruben, M. *Coord. Chem. Rev.*, **2017**, 346, 176-205.

26. Clemente-León, M.; Coronado, E.; López-Jordà, M.; Waerenborgh, J. *Inorg. Chem.*, **2011**, 50, 9122-9130.

27. Ru, J.; Yu, F.; Shi, P.; Jiao, C.; Li, C.; Xiong, R.; Liu, T.; Kurmoo, M.; Zuo, J. *Eur. J. Inorg. Chem.*, **2017**, 3144-3149.

28. Dankhoff, K.; Weber, B. *Dalton Trans.*, **2019**, 48, 15376-15380.

29. Dankhoff, K.; Schneider, S.; Nowak, R.; Weber, B. *Z. Anorg. Allg. Chem.*, **2018**, 1839-1848.

30. Hayes, J.R.; Grosvenor, A.P. *J. Solid State Chem.*, **2013**, 197, 532-542.

31. Her, J.; Matsuda, Y.H.; Nakano, M.; Niwa, Y.; Inada, Y. *J. Appl. Phys.*, **2012**, 111, 053921-1 – 053921-4.

32. Samanta, S.; Ghosh, P.; Goswami, S. *Dalton Trans*., **2012**, 41, 2213-2226.

33. Taylor, R.A.; Bonnano, N.M.; Mirza, D.; Lough, A.J.; Lemaire, M.T. *Polyhedron*, **2017**, 131, 34-39.

34. Taylor, R.A.; Lough, A.J.; Seda, T.; Poddutoori, P.K.; Lemaire, M.T. *Polyhedron*, **2017**, 123, 462-469.

35. Dale, S.; Bonanno, N.M.; Pelaccia, M.; Lough, A.J.; Miyawaki, A.; Takahashi, K.; Lemaire, M.T. *Dalton Trans*., **2019**, 48, 8053-8056.

36. Bonnano, N.M.; Lough, A.J.; Prosser, K.E.; Walsby, C.J.; Poddutoon, P.K.; Lemaire, M.T. *Dalton Trans*., **2016**, 45, 5460-5463.

37. Cook, L.J.K.; Kulmaczewski, R.; Mohammed, R.; Dudley, S.,Barrett, S.A.; Little, M.A.; Deeth, R.J.; Halcrow, M. *Angew. Chem. Int. Ed*., **2016**, 55, 4327-4331.

38. Ivanova, T.A.; Ovchinnikov, I.V.; Garipov, R.R.; Ivanova, G.I. *Appl. Magn. Reson.*, **2011**, 40, 1-10.

39. Nihei, M.; Shiga, T.; Maeda, Y.; Oshio, H. *Coord. Chem. Rev.*, **2007**, 251, 2606-2621.

40. Zenbutu, S.; Nakata, R.; Sumita, M. *Jpn. J. Appl. Phys.*, **1971**, 10, 1497-1502.

41. Muralidhara, R.S.; Kesavulu, C.R.; Rao, J.L.; Anavekar, R.V.; Chakradhar, R.P.S. *J. Phys. And Chem. Solids*, **2010**, 71, 1651-1655.

42. Purcell, E.M. (1985). *Electricity and Magnetism: Vol 2*. N.P.: McGraw-Hill.

43. Teachspin, Inc. (2015). *The Relaxation Times: Vol 4(9).* Foundation Magnetic Susceptibility.

44. Miller, J.S.; Drillon, M. (2001). *Magnetism: Molecules to Materials II*. Weinheim, Germany: Wiley-VCH Verlag GmbH & Co.

45. Phonsri, W.; Davies, C.G.; Jameson, G.N.L.; Moubaraki, B.; Murray, K.S. *Chem. Eur. J.*, **2016**, 22, 1322-1333.

46. Matsumoto, T.; Newton, G.N.; Shiga, T.; Hayami, S.; Matsiu, Y.; Okamoto, H.; Kumai, R.; Murakami, Y.; Oshio, H. *Nature Comm.* **2014**, 5, 3865-3872.

47. Murata, S.; Takahashi, K.; Mochida, T.; Sakurai, T.; Ohta, H.; Yamamoto, T.; Einaga, Y. *Dalton Trans*., **2017**, 46, 5786-5789.

48. Zhang, X.; Wang, Z.; Xie, H.; Li, M.; Woods, T.J.; Dunbar, K.R. *Chem. Sci*., **2006**, 7, 1569-1574.

49. Sekimoto, Y.; Karim, M.R.; Saigo, N.; Ohtani, R.; Nakamura, M.; Hayami, S. *Eur. J. Inorg. Chem*. **2017**, 1049-1053.

50. Nihei, M.; Takahashi, N.; Nishikawa, H.; Oshio, H. *Dalton Trans*., **2011**, 40, 2154-2156.

51. Takahashi, K.; Kawamukai, K.; Okai, M.; Mochida, T.; Sakurai, T.; Ohta, H.; Yamamoto, T.; Einaga, Y.; Shiota, Y.; Yoshizawa, K. *Chem. Eur. J.*, **2016**, 22, 1253 – 1257.

52. Hayami, S.; Gu, Z.; Yoshiki, H.; Fujishima, A.; Sato, O. *J. Am. Chem. Soc.*, **2001**, 123, 11644-11650.

53. Cook, L.J.K.; Shepherd, H.J.; Comyn, T.P.; Baldé. C.; Cespedes, O.; Chastanet, G.; Halcrow, M. *Chem. Eur. J.*, **2015**, 21, 4805-4816.

54. Harding, D.J.; Sertphon, D.; Harding, P.; Murray, K.S.; Moubaraki, B.; Cashion, J.D.; Adams, H. *Chem. Eur. J.*, **2013**, 19, 1082-1090.

55. Djukic, B.; Dube, P.A.; Razavi, F.; Seda, T.; Jenkins, H.A.; Britten, J.F.; Lemaire, M.T. *Inorg. Chem.*, **2009**, 48: 699-707.

56. Elgrishi, N.; Rountree, K.J.; McCarthy, B.D.; Rountree, E.S.; Eisenhart. T.T.; Dempsey, J.L. *J. Chem. Educ*., **2018**, 95, 197-206.

57. Sirirak, J.; Phonsri, W.; Harding, D.J.; Harding, P.; Phommon, P.; Chaoprasa, W.; Hendry, R.M.; Roseveare, T.M.; Adams, H. *J. Mol. Str.*, **2013**, 1036, 439-446.

58. Phonsri, W.; Macedo, D.S.; Davies, C.G.; Jameson, G.N.L.; Moubaraki, B.; Murray, K.S. *Dalton Trans.*, **2017**, 46, 7020 – 7029.

59. Phonsri, W.; Harding, P.; Murray, K.S.; Moubaraki, B.; Harding, D.J. *New J. Chem.*, **2017**, 41, 13747 – 13753.

60. D'Alessandro, D.M. *Chem. Comm.*, **2016**, 52, 8957–8971.

61. Caes, B.; Jensen, D. *J. Chem. Educ.*, **2008**, 85, 413–415.

62. Franz, K.D.; Martin, R.L. *Tetrahedron*, **1978**, 34, 2147–2151.

63. Elgrishi, N.; Rountree, K.J.; McCarthy, B.D.; Rountree, E.S.; Eisenhart. T.T.; Dempsey, J.L. *J. Chem. Educ*. **2018**, 95, 197-206.

64. Damme, N. V.; Lough, A. J.; Gorelsky, S. I.; Lemaire, M. T. *Inorg. Chem.*, **2013**, 52(22), 13021–13028.

65. Chatterjee, I.; Chowdhury, N. S.; Ghosh, P.; Goswami, S. *Inorg. Chem.*, **2015**, 54, 5257–5265.

66. Damme, N. V.; Zaliskyy, V.; Lough, A. J.; Lemaire, M. T. *Polyhedron*, **2015**, 89, 155–159.

67. Vershinina, I.A.; Gornukhina, O.V.; Lubimova, T.V.; Golubchikov, O.A.; Semeikin, A.S. *Russian J. Gen. Chem.*, **2016**, 86, 9, 2232-2235.

68. Sciancelepore, C.; Bondioli, F.; Messori, M. *J. Sol-Gel Sci. Tech.*, **2017**, 81, 69-83.

69. Florini, N.; Berra G.; Tiberto, P.; Allia, P.; Bondioli, F. *J. Am. Ceram. Soc*., **2013**, 96, 3169-3175.

70. Chiswell, B.; Lions, F.; Tomlinson, M.L. *Inorg. Chem*., **1964**, 3, 492-499.

71. Pandeya, K.B.; Singh, R.P.; Bhoon, Y.K. *J. Coord. Chem*., **1976**, 6, 71-74.

72. Edler, E.; Stein, M. *Eur. J. Inorg. Chem*., **2014**, 3587-3599.

73. Wang, L.; Zlatar, M.; Vlahović, F.; Demeshko, S.; Philouze, C.; Molton, F.; Gennari, M.; Meyer, F.; Duboc, C.; Gruden, M. *Chem. Eur. J.*, **2018**, 24, 5091-5094.

74. Melikyan, G.G.; Davis, R.; Anker, B.; Meron, D.; Duncan, K. *Organometallics*. **2016**, 35(24), 4060-4070.

75. Kostka, K.L.; Fox, B.G.; Hendrich, M.P.; Collins, T.J.; Rickard, C.E.F.; Wright, L.J.; Münck, E. *J. Am. Chem. Soc.*, **1993**, 115, 6746-6757.

76. Ling, Y.; Zhang, Y. *J. Am. Chem. Soc. Com.*, **2009**, 131, 6386-6388.

77. Reed, C.A.; Guiset, F. *J. Am. Chem. Soc. Com.*, **1996**, 118, 3281-3282.

78. Sertphon, D.; Harding, D.J.; Harding, P.; Murray, K.S.; Moubaraki, B.; Cashion, J.D.; Adams, H. *Eur. J. Inorg. Chem.*, **2013**, 788-795.

79. Sirirak, J.; Harding, D.J.; Harding, P.; Murray, K.S.; Moubaraki, B.; Liu, L.; Telfer, S.G. *Eur. J. Inorg. Chem.*, **2015**, 2534-2542.

80. Shongwe, M.S.; Al-Rahbi, S.H.; Al-Azani, M.A.; Al-Muharbi, A.A.; Al-Mjeni, F.; Matoga, D.; Gismelseed, A.; Al-Omari, I.A.; Yousif, A.; Adams, H.; Morris, M.J.; Mikuriya, M. *Dalton Trans*., **2012**, 41, 2500-2514.

81. Haddon, R.C.; Rayford, R.; Hirani, A.M. *J. Org. Chem*., **1981**, 46, 4587-4588.

82. Takahashi, K.; Kawamukai, K.; Okai, M.; Mochida, T.; Sakurai, T.; Ohta, H., Yamamoto, T.; Einaga, Y.; Shiota, Y.; Yoshizawa, K. *Chem. Eur. J.*, **2016**, 22, 1253-1257.

83. Tezgerevska, T.; Alley, K.G.; Boskovic, C. *Coord. Chem. Rev*., **2014**, 268, 23-40.

84. Phonsri, W.; Martinez, V.; Davies, C.G.; Jameson, G.N.L.; Moubaraki, B.; Murray, K.S. *Chem. Comm*., **2016**, 52, 1443-1446.

85. O.V. Dolomanov, O.V.; Bourhis, L.J.; Gildea, R.J.; Howard, J.A.K.; Puschmann, H. *J. Appl. Cryst*., **2009**, 42, 339-341.

86. Sheldrick, G.M. *Acta Cryst.*, **2015**, A71, 3-8.

87. Sheldrick, G.M. *Acta Cryst*., **2015**, C71, 3-8.

88. Parsons, S.; Flack, H.D.; Wagner, T. *Acta Cryst*., **2013**, B69, 249-259.

90. Watts, Z. *An Investigation into Heteroleptic [Co(Qsal)(RAL)]$^{+}$ Complexes*, **2019**, Department of Chemistry; Brock University.